First Principles Study of Role of Nuclear Quantum Effects on Properties of HIV/Cancer Inhibitor Ellipticine in protic solvents and Descriptors for Predicting Efficient Dye-sensitized Semiconductor Photocatalysts for Hydrogen Evolution Reaction

A thesis

submitted in partial fulfillment of the requirements

of the degree of

Doctor of Philosophy

by

Subrahmanyam Sappati

Roll No. 20123187

Department of Chemistry

Indian Institute of Science Education and Research, Pune

Pune 411008, Maharashtra, India

May 2019

Certificate

Certified that the work incorporated in the thesis entitled "**First Principles Study of Role of Nuclear Quantum Effects on Properties of HIV/Cancer Inhibitor Ellipticine in protic solvents and Descriptors for Predicting Efficient Dye-sensitized Semiconductor Photocatalysts for Hydrogen Evolution Reaction**" submitted by **Subrahmanyam Sappati** was carried out by the candidate, under my supervision. The work presented here or any part of it has not been included in any other thesis submitted previously for the award of any degree or diploma from any other University or institution.

Date:

(Dr. Prasenjit Ghosh)
Thesis supervisor

Declaration

I, Subrahmanyam Sappati, declare that this thesis titled, "**First Principles Study of Role of Nuclear Quantum Effects on Properties of HIV/Cancer Inhibitor Ellipticine in protic solvents and Descriptors for Predicting Efficient Dye-sensitized Semiconductor Photocatalysts for Hydrogen Evolution Reaction**", written submission represents my ideas in my own words and where others' ideas have been included, I have adequately cited and referenced the original sources. I also declare that I have adhered to all principles of academic honesty and integrity and have not misrepresented or fabricated or falsified any idea/data/fact/source in my submission. I understand that violation of the above will be cause for disciplinary action by the Institute and can also evoke penal action from the sources which have thus not been properly cited or from whom proper permission has not been taken when needed.

Subrahmanyam Sappati
Roll No. 20123187
Date: May 2019

Synopsis

The thesis is divided into two parts. In the first part of the thesis (Chapter 3), we have studied the effect of the quantum nature of the nuclei on the structural, dynamical and electronic properties of ellipticine, a plausible anti-HIV/cancer drug solvated in water. In Chapter 4 we have extended the study to two more protic solvents, namely methanol and ethylene glycol and investigated the role of nuclear quantum effects (NQEs) on the solvent-solute hydrogen bond (H-bond) and how these affect the H-bonding network of the solvent. Further, we have also discussed how the structural fluctuations induced by NQEs strongly affect the optical properties of such H-bonded systems. To achieve this we have used the state-of-the-art path integral molecular dynamics simulations coupled with a recently proposed coloured noise thermostat based on the generalized Langevin equations. In the second part (Chapter 5), using density functional theory based calculations, we have proposed novel descriptors that can be used to screen materials for the design of more efficient dye-sensitized semiconductor photocatalyst for photocatalytic hydrogen evolution reaction.

The thesis is divided into six chapters.

In **Chapter 1**, we have discussed the importance of nuclear quantum effects and explained how path integral molecular dynamics (PIMD) simulations could incorporate nuclear quantum effects. We have also summarized the challenges of performing a straight forward PIMD simulation and discussed the recent developments of the computational techniques that can overcome some of these challenges. Moreover, we have also motivated the importance of photocatalytic water splitting in the context of the present day energy challenges. Further, the remaining chapters of the thesis have also been summarized.

The computational techniques, which are used in the thesis, are discussed in **Chapter 2**. We briefly discuss the basic principles of both classical and Born-Oppenheimer Molecular dynamics formalism (BOMD). The BOMD surfaces on which the ions move were derived using density functional theory (DFT). Hence in this chapter, we have provided a short overview of the theory and practical aspects of DFT. Further to incorporate the NQEs we have used the PIMD simulations with the coloured noise thermostat. Hence we have also described both of these. Additionally, the excited states to study optical properties are computed using time-dependent-DFT (TDDFT). This is also described in a nutshell in this chapter.

In **Chapter 3**, we present the results of the study of NQEs influence the structural and electronic properties of ellipticine, a plausible anti-cancer/HIV inhibiting drug in

a common biological solvent water. From the calculations, it has been shown that quantum effects collectively enhance the fluctuations of both light and heavy nuclei of the covalent and hydrogen bonds in ellipticine. In particular, for the ellipticine water system, where the proton donor and acceptor have different proton affinities, we find that nuclear quantum effects (NQEs) strengthen both the strong and the weak H bonds. This is in contrast to what is observed for the cases where the proton affinity of the donors and acceptors is same. These structural fluctuations cause a significant red shift in the absorption spectra and an increase in the broadening, bringing it into closer agreement with the experiments. This chapter shows that nuclear quantum effects alter both qualitatively and quantitatively the optical properties of this biologically relevant system and highlights the importance of the inclusion of these effects in the microscopic understanding of their optical properties.

Chapter 4: In this chapter, we extend the study of the importance NQEs for the H-bonding of ellipticine to two more protic solvents (methanol and ethylene glycol) and investigate the generality of conclusions in the previous chapter. Additionally, we have also investigated the influence of the ellipticine-solvent H-bonding on the H-bonding network amongst the solvent molecules. We find that as we move from water to methanol to ethylene glycol, the strong H bond between pyridine N of ellipticine and solvent molecule weakens. In contrast with water, the simulations show that NQE weakens this H bond for methanol while for ethylene glycol NQEs do not significantly change the H bond strength. For the weak H bond between pyrrole N and solvent molecules, NQE strengthens the H-bond for methanol (similar to what was observed for water) and weakens for ethylene glycol. Additionally, we show that if solute-solvent H bond is strong, the H-bond between solvent molecules that are close to the solute is further strengthened. Finally, we also show that for H-bonded systems, it is crucial to incorporate the NQEs even for qualitative agreements between computed and experimentally measured absorption spectra.

Chapter 5: In this chapter, we have proposed descriptors that can be used for screening dyes-semiconductor composites, which can be used to design novel photocatalysts for hydrogen evolution reaction (HER). Specifically, we have shown that for ZnO nanoparticles sensitized with azo and thiophene based dyes, the electron-hole separation and charge injection capacity together correlates well with the turnover number for hydrogen production from photocatalytic water splitting. Further based on a recipe proposed by Bahers *et al.* [1] and Luca *et al.* [2]. We show that reasonably good estimates of these two properties can be obtained from simple ground state calculations.

Finally, we summarize the results presented in this thesis in **Chapter 6**, provide a broad outlook of the same and discuss the future directions in which further work can

be pursued.

To my parents

Acknowledgements

First and foremost, I would like to express my earnest thanks to my thesis supervisor, Dr. Prasenjit Ghosh for his constant encouragement, support, and guidance throughout my research. His conscientious effort and training was the reason behind every success achieved by me and undoubtedly is the asset for my future research. This thesis would not have been possible without his valuable support. I would like to extend heartfelt thanks to Dr. Ralph Gebauer, Dr. Ali Hassanali, and Mr. Ivan Girotto who are the mentors for my first part of my thesis and improved in many aspects such as understanding physics topics, guidance to molecular dynamics with nuclear quantum effects and parallelization techniques for using resources efficiently and effectively. Further generous invitations for multiple short-term visits at ICTP and the international conferences held at Abdu Salam International Center for Theoretical and Physics (ICTP), Trieste, Italy. I would like to thank and dedicated my research work to my parents Sappati Ramarao and Sappati Sreelaxmi, and my sisters S Bharati, and S Pavani.

I am grateful to the Research Advisory Committee (RAC) members Dr. Anirban Hazra, and Dr. Nandini Devi for their valuable suggestions and comments during RAC meetings. The critical examination of my research work and valuable comments from all of the RAC members were always very useful. Because of their guidance and suggestions, I gained experience to work in diverse fields of research which was indeed very helpful. I am grateful to our collaborators, Dr. Nirmalya Ballav, Dr. Partha Hazra and Dr. Nandini Devi for giving me the opportunity to work with them on different collaborative research projects, especially with their students Dr. Barun Dara, Dr. Ranguwar Rajendra, Dr. Plawan Kumar Jha, Dr. RajKumar Konniti, Dr. Krishna G, Dr. Leena George. I learned several techniques in computational studies by helping my seniors and colleagues at post graduation and doctoral studies (viz, Dr. M. Ganesh from Dr. H. N. Gopi's lab, Dr. E. Sateesh from Prof. K. N. Ganesh's lab, Dr. Kiran Kumar Reddy from Dr. V. G. Anand, Dr. Hari Krishna, Dr. Shiva Koti from Dr. Ragavendra K's lab, Mr. Udaya, Mr. Ashok and Dr. Ashok from Dr. Boomishankar's Lab, Dr. Rajesh from Dr. R. G. Bhat's lab).

Further, I want to extend my sincere thanks to my teachers who supported me to the point (viz, Mr. B. Eswara Rao (Ushodaya), Mr. J. Ramesh (Uralm, my school teacher), Mr. Raghu (Ushodaya), Mr. Govind (Ushodaya), Mr. M. Rambabu (JNV), Mr. Bhaskar (Gayatri college), Mr. Prakash (Gayatri college), Mr. Rambabu (Chemica), Prof. Susanta Mahapatra, Prof. M. Durga prasad, Prof. T. P. Radhakrishnan, Prof. Anunaya Samntha, Prof. K. D. Sen, other UoH faculty and Prof. Srinivas Hotha)

Similarly, special thanks to Dr. Phani Murali Krishna, Dr. Anmol, Dr. Surya Brahmam, Dr. Ramakrishna, Dr. Chaitanya, Dr. Y. G. Reddy, Dr. Mahesh Gudem, Dr. Sandeep Kumar P, Dr. Reman K. Singh, Dr. Praveen, Dr. Avdhoot Datar, to support when I was in difficulty.

I would like to acknowledge Prof. Prasenjit Sen, Harish Chandra Research Institute, India, CDAC Pune, India and the Abdus Salam ICTP, Trieste, Italy for providing computing resources. I would like to thank Dr. Partha Hazra and Dr. Raj kumar Koninti, IISER Pune, India for providing the experimental absorption spectra of ellipticine in solvents. Mr. Uday for NMR spectra of carbazole in protic and aprotic solvents. I acknowledge Indian Institute of Science Education and Research (IISER), Pune for providing excellent research facilities and an outstanding research environment. I would like to acknowledge DST-Nanomission Project No SR/NM/NS-1285/2014 for funding. I also would like to thank Infosys for financial support to attend a conference and a short term visit at the Abdus Salam International Center for Theoretical Physics, Trieste, Italy.

I also express my sincere thanks to my co-mates/seniors Dr. Niharika Joshi, Dr. N. Kumar V., Dr. Indu Kaul, Dr. Rahul Hardikar, Dr. Krishna Kanth, and Dr. Saikat C. and extended my special thanks to my juniors Mr. Unmesh Mondal, Ms. Ashwathi, Mr. Vineet, Ms. Aarti, Mr. Hossian, Ms Kanika, Mr. Aseem, Mr. Amit Sahu, Mr. Gautam, Dr. Bhamu, and all other lab-mates for their suggestions toward the betterment of my performance in every aspect.

Further, I would like to thank my childhood friends, JNV-Srikakulam (1999-2006) friends, under graduation friends (2007-2009), post-graduation friends (2009-2011) and doctoral studies friends [Jagan, Naveen, Veeresh, Gayatri, Pavan]. I can not think of my research life without friends. Further, I would like to thank my relatives especially my brother in law's (Mr. K. Kondala Rao and Mr. P. Mukhalingam), my niece (K. Surya Supraja) and my nephew (P. Harshith) and other near and dear relatives, Dr. Anusha, Sowmya, Navya, Kavya and Anupam. Finally thanks to everyone who helped me to complete my doctoral studies.

List of Figures

List of Tables

Contents

Abbreviations

H-bond	**H**ydrogen **B**onding
GLE	**G**eneralized **L**angevin **E**quation
PIMD	**P**ath **I**ntegral **M**olecular **D**ynamics
PIGLET	**P**ath **I**ntegral **G**eneralized **L**angevin **E**quation **T**hermostat
NQEs	**N**uclear **Q**uantum **E**ffects
DFT	**D**ensity **F**unctional **T**heory
TDDFT	**T**ime-**D**ependent **D**ensity **F**unctional **T**heory
BOMD	**B**orn **O**ppenheimer **M**olecular **D**ynamics
CMD	**C**lassical **M**olecular **D**ynamics
AMBER	**A**ssisted **M**odel **B**uilding with **E**nergy **R**efinement
GAFF	**G**eneral **A**MBER **F**orce **F**ield
OPLS	**O**ptimized **P**otential for **L**iquid **S**imulation for All Atom
PCWS	**P**hoto-**C**atalytic **W**ater **S**plitting
PTC	**P**roton **T**ransfer **C**oordinate
HOMO	**H**ighest **O**ccupied **M**olecular **O**rbital
LUMO	**L**owest **U**noccupied **M**olecular **O**rbital
OP	**O**xidation **P**otential
RP	**R**eduction **P**otential
WS	**W**ater **S**plitting
VBM	**V**alence **B**and **M**axima
CBM	**C**onduction **B**and **M**inima
NHE	**N**ormal **H**ydrogen **E**lectrode
EWG	**E**lectron-**W**ithdrawing **G**roup
EDG	**E**lectron **D**onating **G**roup
ΔE	**D**ifference between HOMO and LUMO **E**nergies

$\mathbf{E}_g$	**B**and **G**ap
HER	**H**ydrogen **E**volution **R**eaction
OER	**O**xygen **E**volution **R**eaction
EP	**E**llipticine
GGA	**G**eneralized **G**radient **A**pproximation

Chapter 1

Introduction

In this thesis, using first principles simulations, I have studied two important physical processes. In the first part, I have investigated the importance of nuclear quantum effects (NQE) on the structural and electronic properties of ellipticine, a plausible anti-cancer, anti-HIV drug. In the second part of my thesis, I have proposed some descriptors that can be used to design dye-sensitized semiconductor based photocatalyst for hydrogen evolution reaction (HER). These descriptors can also be used for the rational design of dye-sensitized photovoltaics. Below I briefly introduce the significance of nuclear quantum effects, the principle of photocatalytic water splitting and provide a brief outline of the remaining chapters of the thesis.

1.1 Nuclear quantum effects

The Born-Oppenheimer approximation that enables us to separate the nuclear and electronic degrees of freedom forms the basis of any quantum chemistry calculations. In addition to this, it is also routinely approximated that nuclear motion can be treated classically. However, within this second approximation, the simulations lose the ability to capture several important phenomena related to the quantum nature of the nuclear motion viz. the zero-point energy, tunneling, etc. For example, the zero point energy of a typical chemical bond exceeds the thermal energy scale by order of magnitude, which might result in changes in reaction rates of reactions involving light nuclei even at room temperature. NQEs can make large changes to the structure and dynamics in processes

ranging from proton delocalization and tunneling in enzymes [3, 8–11] to the phase diagram of high pressure melt [12] to changes in the stability of crystal polymorphs [13]. Further, the importance of nuclear quantum effects (NQE) are not only restricted to light nuclei like protons but are also observed for heavy nuclei. For example, it has been shown that the unusually high reaction rate (4×10^{-6} s^{-1}) in the rearrangement of carbene to cyclopentene observed experimentally at ultra-low temperatures is due to tunneling [14].

Path integral approach to quantum mechanics provides an elegant way to treat NQEs for equilibrium and dynamical properties. Within the Lagrangian formulation of classical mechanics, a particle follows the path that minimizes its action. In contrast, the path integral formulation considers what happens if deviations from the classical path are allowed. In his seminal work Feynman showed that by summing the amplitudes associated with all possible paths, quantum mechanics emerges in a physically insightful way. In the limit when all the paths that deviate from minimum action one cancel each other due to their positive and negative amplitudes, classical mechanics emerges. These oscillatory amplitudes imply that a naive implementation of the path integral formulation is computationally intractable. However, while computing static properties, the oscillatory amplitudes of the paths no longer appear because of the fact that evaluating these properties requires one to weight the states of the system by a Boltzmann factor ($e^{-\beta \hat{H}}$). This is typically referred to as the imaginary time propagator because it is related to the real time propagator ($e^{-i\hat{H}t/\hbar}$) by replacing $t = i\beta\hbar$. This allows the calculation of static properties to be exactly mapped onto a classical problem composed of P replicas of the classical system, where these replicas are connected through harmonic springs as shown schematically in Figure 1.1. The main computational cost lies in the fact that the number of replicas needs to be sufficiently large to reach the quantum limit. The value of P needed to converge path integral molecular dynamics (PIMD) is related to the ratio of the harmonic quantum energy level spacing to the thermal energy $\left(\frac{\hbar\omega_{max}}{k_B T}\right)$. P grows rapidly as the maximum vibrational frequency (ω_{max}) in the system increases or the temperature (T) decreases. For a typical O-H covalent bond system at room temperature at least 32 replicas are necessary to obtain converged structural properties. Additionally, the frequencies associated with the ring polymer (ω_P) is usually many times higher than the maximum physical frequencies. This necessities the use of a

reduced integration time-step and aggressive thermostatting. To circumvent these difficulties there are a lot of efforts to develop efficient integrators and thermostats. One such method is the "Ring polymer contraction" where the P-replica description is mapped to a P'-replica problem [15]. Further, there are also efforts to use higher order terms in the Trotter decomposition of the Boltzmann factor [16]. Among the different thermostats, Ceriotti *et al* have developed some elegant methods that combine PIMD with a generalized Langevin equation based coloured-noise thermostat (PIGLET) [17, 18]. Using this thermostat, they have shown that the same level of accuracy of a full PIMD simulation can be achieved with fractional computational cost [15–19].

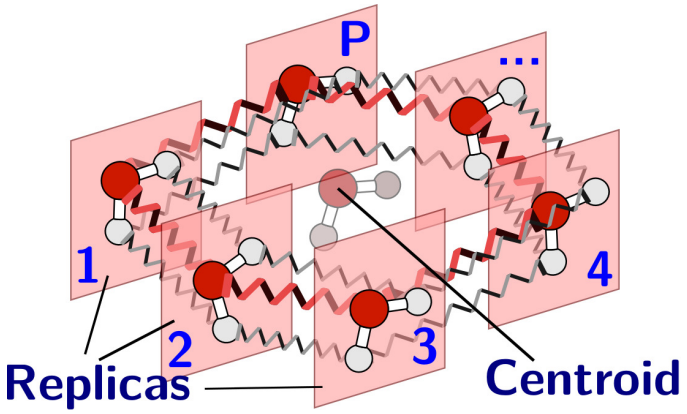

FIGURE 1.1: Schematic representation of a ring-polymer (imaginary time path integral) simulation of a water molecule. Each replica (bead) comprises physical interaction between one oxygen and two hydrogen atoms, and corresponding atoms in adjacent replicas are joined by a harmonic spring. Reprinted with permission from Reference [3] Copyright© 2018, Nature review.

Recently, PIGLET had been used to explore the role of NQEs on the structural and electronic fluctuations of both neutral and protonated solvents [18, 19]. In this thesis, performing PIMD simulations with the above mentioned coloured noise thermostat we have studied NQEs on the structural and electronic properties of ellipticine (EP), a plausible anti-cancer/HIV drug in three protic solvents, namely water, methanol, and ethylene glycol.

1.2 Photocatalytic water splitting (PCWS)

Till date, fossil fuels serve as the primary source of energy. However, with the ever increasing demand for energy, dwindling energy resources and environmental deterioration due to combustion of fossil fuels, there is an increased focus on utilizing solar

power as an alternative to fossil fuels. Depending on geographical location, seasons and time there are variations in the degree of sunlight reaching different places on the planet. Hence, for efficient utilization of solar resources, the solar energy needs to be converted and stored in a cost-effective and environmentally friendly way. H_2 is a potential high-energy-density and carbon-free energy carrier. The energy stored in hydrogen can be released either through direct combustion or a hydrogen fuel cell where water is the only product. Additionally, H_2 is also an important industrial feedstock for several industrially important reactions including ammonia synthesis. Hence the production of hydrogen using solar powered water splitting is one of the most important approaches for harnessing solar energy.

Splitting of water into H_2 and O_2 is a thermodynamically unfavorable reaction that requires an energy input of 2.46 eV as shown in Eqn. 1.1:

$$H_2O \rightarrow H_2 + \frac{1}{2}O_2, \qquad \Delta G^0 = 2.46 \text{ eV} \tag{1.1}$$

In order to drive this reaction, a semiconductor is excited by shining light containing energy equal to or greater than the band gap. When sufficient photochemical energy is applied, electrons are excited to the conduction band leaving behind holes valence band of the semiconductor. These electron-hole pairs play a crucial role in the redox reactions of water splitting. The electrons reduce the proton to produce hydrogen while the holes oxidize oxygen anions. The two half reactions are given below:

$$H_2O + 2h^+ \rightarrow 2H^+ + \frac{1}{2}O_2 \qquad E^0_{\text{oxidation}} = \text{-1.23 V} \tag{1.2}$$

$$2H^+ + 2e^- \rightarrow H_2 \qquad E^0_{\text{reduction}} = 0.00 \text{ V} \tag{1.3}$$

For the reaction to proceed, it is evident that the conduction band minima of the semiconductor should be more negative than the hydrogen evolution potential (E_{H_2/H_2O}, 0 V vs. Normal Hydrogen Electrode, NHE) and the valence band maximum should be more positive than the water oxidation level (E_{O_2/H_2O}, 1.23 V vs. NHE). Moreover, the minimum band gap of a semiconductor to be suitable for a PCWS photocatalyst should be 1.23 eV. These are schematically shown in Figure 1.2 (a). In addition to the

above two criteria, the photocatalyst should also be resistant to photocorrosion. Typically metal oxides, sulphides, nitrides, and phosphates with d^0 or d^{10} transition metal elements are used as a photocatalyst [20]. Group I and Group II metals along with some lanthanides form perovskite materials that can also be used as a photocatalyst. Apart from the conventional ones, there are also efforts to develop graphene-based materials to be used for the same purpose. For PCWS high crystallinity and small particle size are desired to prevent electron-hole recombination. A summary of different common semiconductors and their band alignment with respect to the oxidation and reduction potentials are shown in Figure 1.2 (b).

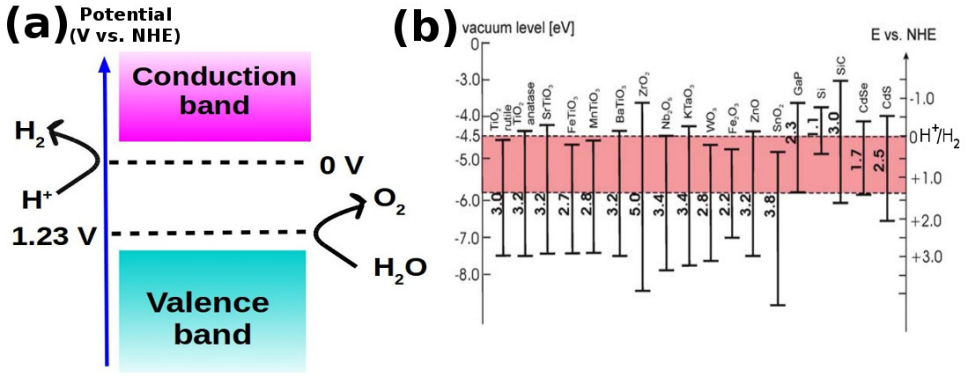

FIGURE 1.2: (a) Schematic representation of the band alignment diagram of semiconductor for photocatalytic water splitting. (b) Some semiconductor photocatalysts and their corresponding band positions with respect to the water redox potential Reprinted with permission from ref. [4] Copyright© 2011 RSC.

To the best of our knowledge, to date, there are very few photocatalysts available that are capable of water splitting through visible light driven processes [4, 21]. Further, the efficiency of this process is still far from reaching industrial standards [22]. Hence there are several efforts to improve the overall efficiency of the process. For example, electron donors (eg. methanol) or acceptors (eg. Ag^+) are added to the reaction solution to drive either of the reactions. Further novel interfaces are engineered or surfaces of photoanodes are modified to improve the performance. Additionally there are also reports of adding co-catalysts like noble metals (Pt, Co, etc.), transition metal dichalcogenides, transition metal phosphides, carbides and nitrides [23–27] for hydrogen evolution and electrolytes such as trimethylamine, methanol and KOH for oxygen evolution to speed up the reactions [28, 29].

Another potential route for designing efficient catalysts for photocatalytic water splitting using visible light is to use dye-sensitized semiconductors. This was first proposed in Gratzel's group in the early 1980s where they used Pt and RuO_2 co-deposited on Nb-doped TiO_2 particles along with Ru based dyes for water splitting [30]. Later several other transition metal based dyes and porphyrins are used for the same purpose [31–33]. A nice review of the same can be found in Reference [6]. However, most of these photocatalysts are prepared on a trial and error basis. In this part of the thesis, we propose some descriptors, based on properties of the semiconductor-dye composite, that can be used for rational design of dye-sensitized semiconductor photocatalyst.

1.3 Outline of the thesis

The rest of the thesis is organized as follows:

Chapter 2: The computational techniques, which are used in the thesis, are discussed in this chapter. I briefly discuss the basic principles of both classical and Born-Oppenheimer Molecular dynamics formalism. The BOMD surfaces on which the ions move was derived using density functional theory (DFT). Hence in this chapter, I have provided a short overview of the theory and practical aspects of DFT. Further to incorporate the NQEs I have used the PIMD simulations with the coloured noise thermostat. Hence I have also described both of these. Additionally, the excited states to study optical properties are computed using time-dependent-DFT (TDDFT). This is also described in a nutshell in this chapter.

Chapter 3: In this chapter, using PIMD and TDDFT based calculation, I have studied how NQEs influence the structural and electronic properties of ellipticine, a plausible anti-cancer/HIV inhibiting drug in common biological solvent water. From the calculations, it has been shown that quantum effects collectively enhance the fluctuations of both light and heavy nuclei of the covalent and hydrogen bonds in ellipticine. In particular, for the ellipticine water system, where the proton donor and acceptor have different proton affinities, we find that nuclear quantum effects (NQEs) strengthen both the strong and the weak H bonds. This is in contrast to what is observed for the cases where the proton affinity of the donors and acceptors is same. These structural fluctuations cause a significant red shift in the absorption spectra and an increase in the

broadening, bringing it into closer agreement with the experiments. This chapter shows that nuclear quantum effects alter both qualitatively and quantitatively the optical properties of this biologically relevant system and highlights the importance of the inclusion of these effects in the microscopic understanding of their optical properties.

Chapter 4: In this chapter, we extend the study of the importance NQEs for the H-bonding of ellipticine in two more protic solvents (methanol and ethylene glycol) and investigate the generality of conclusions in the previous chapter. Additionally, we have also investigated the influence of the ellipticine-solvent H-bonding on the H-bonding network amongst the solvent molecules. We find that as we move from water to methanol to ethylene glycol the strong H bond between pyridine N of ellipticine and solvent molecule weakens. In contrast with water, our simulations show that NQE weakens this H bond for methanol while for ethylene glycol NQEs do not significantly change the H bond strength. For the weak H bond between pyrrole N and solvent molecules, NQE strengthens the H-bond for methanol (similar to what was observed for water) and weakens for ethylene glycol. Additionally, we show that if solute-solvent H bond is strong, the H-bond between solvent molecules that are close to the solute are further strengthened. Finally, we also show that for H-bonded systems, it is crucial to incorporate the NQEs even for qualitative agreements between computed and experimentally measured absorption spectra.

Chapter 5: In this chapter, I have proposed descriptors that can be used for screening dyes-semiconductor composites, which can be used to design novel photocatalysts for hydrogen evolution reaction (HER). Specifically, I have shown that for ZnO nanoparticles sensitized with azo and thiophene based dyes, the electron-hole separation and charge injection capacity together correlates well with the turnover number for hydrogen production from photocatalytic water splitting. Further based on a recipe proposed by Bahers *et al.* [1] and Luca *et al.* [2]. I show that reasonably good estimates of these two properties can be obtained simple ground state calculations.

Chapter 6: In this chapter, I summarize my thesis, provide a broad outlook of the results presented in this thesis and discuss the future directions in which further work can be pursued.

Chapter 2

Computational Methodologies

In this chapter, we have discussed the computational methodologies employed in this thesis. Firstly we have shown the theoretical derivation of the Schrödinger equation and Born-Oppenheimer approximation. Then we have discussed classical molecular dynamics, Born-Oppenheimer molecular dynamics, Kohn-Sham density functional theory. Further, we have discussed path integral molecular dynamics (PIMD) and the accelerated method for PI, such as PIGLET. Finally, we have concluded with a spectroscopic methodology such as time-dependent density functional (TDDFT) theory.

2.1 Quantum many-body problem and electronic structure

Be it the field of chemistry, biology or material science, the behavior of electrons is accurately described by the many-body Hamiltonian of the Schrödinger equation.

2.1.1 The Schrödinger equation

The Schrödinger equation is perhaps the most important equation in the entire field of quantum mechanics. The time-dependent Schrödinger equation given below, using the notation of Marx and Hutter, form the backbone of molecular dynamics method theory.

$$i\hbar\frac{\partial}{\partial t}\Phi(\{r_i\};\{R_i\};t) = \hat{\mathcal{H}}\Phi(\{r_i\};\{R_i\};t) \tag{2.1}$$

The microscopic properties of electrons in atoms, molecules, and solids are accurately explained by using many-body Hamiltonian ($\hat{\mathcal{H}}$) in the Schrödinger equation. The many-body standard Hamiltonian for a system with N_{nuc} atoms and N electrons is

$$\hat{\mathcal{H}} = -\sum_{I=1}^{N_{nuc}} \frac{\hbar^2 \nabla_I^2}{2M_I} - \sum_{i=1}^{N} \frac{\hbar^2 \nabla_i^2}{2m_e} - \frac{1}{4\pi\epsilon_0} \sum_{i,I} \frac{e^2 Z_I}{|r_i - R_I|} + \frac{1}{4\pi\epsilon_0} \sum_{i<j} \frac{e^2}{|r_i - r_j|} + \frac{1}{4\pi\epsilon_0} \sum_{I<J} \frac{e^2 Z_I Z_J}{|R_I - R_J|} \tag{2.2}$$

The indices in upper case (*viz* I, J) and lower case (*viz* i, j) represent nuclei and electrons respectively, with the corresponding positions R_I and r_i. M_I and m_e represent the nucleus mass and electron mass, Z is the atomic number and ϵ_0 is the vacuum permittivity. In the above equation, the first two terms of the Hamiltonian consist of the kinetic energy, first one due to ionic motion and second one due to the motion of electrons, rest of the terms represent the interaction part where the third term represents electron-ion attraction followed by electron-electron repulsion and ion-ion repulsion represented in the fourth and fifth term respectively.

The above Hamiltonian can be rewritten as

$$\hat{\mathcal{H}} = -\sum_{I=1} \frac{\hbar^2 \nabla_I^2}{2M_I} - \sum_{I=1} \frac{\hbar^2 \nabla_i^2}{2m_e} + V_{n-e}(r_i, R_I) = -\sum_{I=1} \frac{\hbar^2 \nabla_I^2}{2M_I} + \hat{\mathcal{H}}_e(r_i, R_I) \tag{2.3}$$

where V_{n-e} represent the electrostatic interaction term and $\hat{\mathcal{H}}_e$ represent the electronic Hamiltonian when the ionic position (R_I) vary parametrically.

Consider that the solution to the time-independent electronic Schrödinger equation,

$$\hat{\mathcal{H}}(\{r_i\};\{R_I\})\Psi(\{r_i\};\{R_I\}) = E_k(\{R_I\})\Psi_k(\{r_i\};\{R_I\}), \tag{2.4}$$

is understood for all possible nuclear configurations, R_I. This is the way used to develop electronic and nuclear DoFs. Thereafter the total wavefunction is expanded in terms of the orthonormal eigenstates to $\hat{\mathcal{H}}_e$,

$$\Phi(\{r_i\};\{R_I\};t) = \sum_{l=0}^{\infty} \Psi_l(\{r_i\};\{R_I\})\chi_l(\{R_I\};t) \tag{2.5}$$

where χ_l is the time-dependent expansion coefficient. The enormous complications associated with the quantum many-body problems was well stated by Dirac in 1929 [34] : "*The fundamental laws necessary to the mathematical treatment of large parts of physics and the whole of chemistry are thus fully known, and the difficulty lies only in the fact that application of these laws leads to equations that are too complex to be solved.*"

Last century, Born [35] introduced this method which separates the dynamics of the light particle, the electrons, from that of the heavy particle, the nucleus. By inserting equation (2.1), multiplying the conjugate of wavefunction $\Psi_l^*(\mathrm{r}_i;\, \mathrm{R}_I)$ and further integrating over all electronic coordinates r_i we obtain a set of coupled differential equations,

$$\left[-\sum_I \frac{\hbar^2}{2M_I}\nabla_I^2 + E_k(\{R_I\})\right]\chi_k + \sum_l C_{kl}\chi_{kl} = i\hbar\frac{\partial}{\partial t}\chi_k \tag{2.6}$$

with

$$C_{kl} = \int \Psi_k^* \left[-\sum_I \frac{\hbar^2}{2M_I}\nabla_I^2\right]\Psi_l dr + \frac{1}{M_I}\sum_I \left\{\int \Psi_k^* \left[-i\hbar\nabla_I\right]\Psi_l dr\right\}\left[-i\hbar\nabla_I\right]. \tag{2.7}$$

The crossing terms between different states are given by matrix elements C_{kl}. Setting the coupling elements to zero, following the Born-Oppenheimer (BO) approximation, leads to a completely decoupled set of equations,

$$\left[-\sum_I \frac{\hbar^2}{2M_I}\nabla_I^2 + E_k(\{R_I\})\right]\chi_k = i\hbar\frac{\partial}{\partial t}\chi_k \tag{2.8}$$

Though the interaction between different states has been lifted, still the system will remain in its initial quantum state throughout the dynamics. In the next step, the nuclei wavefunctions χ_k are approximated as classical point particles.
This is done by taking the wave function in terms of an amplitude factor A_k and a phase factor S_k

$$\chi_k(\{R_I\};t) = A_k(\{R_I\};t)e^{\left(\frac{iS_k(\{R_I\};t)}{\hbar}\right)} \tag{2.9}$$

Using the following transformation for the momenta of the nuclei,

$$P_I = \nabla_I S_k \tag{2.10}$$

the Newtonian equations of motion $\dot{P}_I = -\nabla_I V_k(\{R_I\})$ can be written as

$$\frac{dP_I}{dt} = -\nabla_I E_k \tag{2.11}$$

or

$$M_I \ddot{R}_I(t) = -\nabla_I V_0^{BO}(R_I t). \tag{2.12}$$

In the Born-Oppenheimer approximation the potential, V_k^{BO}, is restricted to the ground state of the time-independent Schrōdinger equation, Equation (2.3), thus

$$V_0^{BO} = \int \Psi_0^* \hat{\mathcal{H}}_e \Psi_0 = E_0(\{R_I\}) \tag{2.13}$$

the BO approximation can be motivated mainly by the fact that electrons usually move much faster than the nuclei, often by 3 orders of magnitude (hence electronic wavefunction depends parametrically on nucleus position but not velocities of ions).

After Born-Oppenheimer approximation, the effective Hamiltonian can now be rewritten as

$$H = -\sum_i \frac{\hbar^2}{2m_i}\nabla_i^2 + \sum_{i \neq j} \frac{e^2}{2} \frac{1}{|r_i - r_j|} - \sum_{i,I} \frac{eZ_I}{R_I - r_i} + V_{ion} \tag{2.14}$$

where the first term describes the kinetic energy of electrons, followed by electron-electron interaction and the attractive Coulomb interaction between electrons and static ions. The last term is the additive energy for the ion-ion interaction calculated using Born-Oppenheimer approximation. Further simplification of the Hamiltonian requires decoupling of the electron-electron interactions, regardless in practice this approximation has proved to accurately describe a large number of interesting systems.

This approximation fails in some instances, for example, when one wishes to explore the dynamics of the decay of an excited state to a lower state, i.e, at the conical intersection, and when the nucleus is light such as isotopes of hydrogen.

In *ab initio* molecular dynamics the potential V_k^{BO} is calculated directly but since this is computationally expensive it is often approximated further. In classical molecular dynamics V_k^{BO} is expanded in a set of many-body interactions.

2.2 Classical Molecular Dynamics

Classical molecular dynamics models the behavior of atoms using classical or Newtonian mechanics. This approach assumes that the atomic interactions being modeled can be done reasonably well without explicitly accounting for the electrons and molecular orbitals. Fortunately, this can be validated for many systems such as biological molecules, ions in aqueous media, etc. because their behavior and dynamics are dominantly controlled by the hydration energy, charge and mass. These quantities can be modeled accurately by treating the atoms as point charges with an assigned mass and describing their interactions using classical physics.

As we discussed in the previous section, classical molecular dynamics is driven by Newtonian mechanics and the potential is expanded by many-body interactions which are discussed below.

2.2.1 Potential functions

The potential energy of a molecular system can be decomposed into bonding and non-bonding interactions. The bonding interactions comprise of bond, angles, proper and improper dihedrals while the non-bonding interactions are van der Waals and electrostatic interactions. Therefore, the total potential energy can be written as:

$$V(r_N) = V_{bonding} + V_{non-bonding} \tag{2.15}$$

Where $V_{bonding}$ can be written as

$$
\begin{aligned}
V_{bonding} &= \frac{1}{2}\sum_{bonds} k^{r}_{ij}(r_{ij} - r_{eq})^2 \\
&+ \frac{1}{2}\sum_{angles} k^{\theta}_{ijk}(\theta_{ij} - \theta_{eq})^2 \\
&+ \frac{1}{2}\sum_{dihed.}\sum_{m} k^{\phi,m}_{ijkl}(1 + cos(\phi_{ijkl} - \gamma_m))
\end{aligned}
\tag{2.16}
$$

The bonds involve the separation $r_{ij} = ||r_i - r_j||$ between adjacent pairs of atoms in a molecular framework. Similarly, θ_{ij} and ϕ_{ijkl} are the angle and dihedral of the system. r_{eq}, θ_{eq}, and γ_m are the equilibrium bond length, angle, and dihedral of the system.

Similarly, $V_{non-bonding}$ can be written as

$$
V_{non-bonding} = U_{ab}(r_{ij}) + U_c(r_{ij}) \tag{2.17}
$$

$$
U_{ab}(r_{ij}) = 4\epsilon_{ab}\left[\left(\frac{\sigma_{ab}}{r_{ij}}\right)^6 - \left(\frac{\sigma_{ab}}{r_{ij}}\right)^{12}\right] \tag{2.18}
$$

$$
U_c(r_{ij}) = \left(\frac{1}{4\pi\epsilon_0}\right)\frac{q_a q_b}{r_{ij}} \tag{2.19}
$$

where, σ_{ij} and ϵ_{ij} are van der Waals parameters, calculated using an arithmetic average and geometric average respectively. The ϵ_0 is the permittivity of vacuum, ϵ_r is the relative dielectric constant and q_i and q_j denotes the partial charges on different atoms. The mathematical terms in 2.16, 2.18, and 2.19 are called as a force-field, where the parameters are either obtained from experiments or from fundamental quantum calculations. It is often difficult to derive a sufficiently accurate force-field for a molecular system of interest which is based on assumptions, approximations and simplifications and is thus subjected to the property of interest, methodology, and adapted algorithms.

2.3 *Ab initio* Molecular Dynamics

Ab initio molecular dynamics (AIMD) has great advantages over classical molecular dynamics in the sense that the former is extremely accurate. Also in AIMD, there is no need to fit any parameters and all that has to be specified is the atomic positions and the atomic number of the element, and everything else will be derived from fundamental laws of physics. It is important to note that at each of the MD step, density of the system ($n(r_i)$) will be updated accordingly, on other hand classical MD have fixed information of potential, which is the main drawback. The calculation of the density of the system ($n(r_i)$) is discussed in section 2.4. AIMD has been extremely expensive because of the difficulty associated with solving the numerical equations. However, due to advancements in theory and the exponential growth of computer power, many more interesting problems are now solvable. Note that in AIMD, electrons are treated as quantum particles (wavefunction) however ions are treated as classical particles. Path integral techniques helps to treat both particles (electrons and ions) quantum mechanically, which we have discussed in section 2.5.

2.4 Density Functional Theory (DFT)

In *ab initio* molecular dynamics there are no empirical potentials, hence the time-independent Schrödinger equation, Equation (2.1), needs to be solved directly. In the Schrödinger equations, there are approximately 10^{24} dependent variables for a real material, which makes it impossible to solve this equation directly. Though it can be reduced by the symmetry of the crystal there are still several hundreds of dependent variables in the wavefunction to solve. Since the independent one-electron wavefunction is a very good approximation in many cases, a Slater-determinant of independent one-electron wavefunctions can help in solving this with less trouble. Density Functional Theory (DFT) exploits this fact by substituting our system of dependent variables (in a simple potential) with a system of independent variables (in a complicated potential) while hiding all the complicated many-body interactions in an effective potential.

Hartree proposed that the many-body electronic wave function can be written as a product of single electron wave functions $\phi(r_1, r_2, ..., r_N) = \phi_1(r_1)\phi_2(r_2)...\phi_N(r_N)$. Each

wave function $\phi_i(r_i)$ has as independent Schrödinger equation and the effective potential experienced by an electron as a result of the Coulomb interaction with remaining electrons and ions given by the second and third terms in the following Schrödinger equation,

$$-\frac{\hbar^2}{2m_i}\nabla_i^2\phi_i(r) + e^2\int\frac{\sum_{i\neq j}|\phi_j(r')|^2}{r-r'}dr' = \epsilon_i\phi_i(r). \tag{2.20}$$

The total energy is given by,

$$E = \sum_i \epsilon_i - \frac{e^2}{2}\int\int\frac{\rho_i(r)\rho_j(r')}{|r-r'|}drdr' \tag{2.21}$$

where the second term accounts for the double counted electron-electron interaction, also known as the Hartree energy. Note that $\rho(r) = |\phi(r)|^2$ denotes the electron density. Thus, a self-consistent solution of the Schrödinger equation is obtained by the variational approach, where the total energy is minimized with respect to either wave function or electron density. The resultant eigenenergy is the sum of many single-particle energies. However, the Hartree approach does not take into account the Fermi-Dirac statistics for electrons. The antisymmetric nature of electronic wave function ϕ expressed using the Slater determinant is addressed within the Hartree-Fock approximation. The exchange interaction between two anti-parallel electrons lowers the Coulomb energy of the system due to a reduction in electron-electron repulsion, this energy gain is known as the exchange energy. The Schrödinger equation for Hartree-Fock approximation is

$$\left(-\frac{\hbar^2}{2m_i}\nabla_i^2 + V_{ion}(r_i) + \int\frac{\sum_{i\neq j}\rho_j(r')}{r-r'}dr' - e^2\sum_{i\neq j}\int\frac{\phi_i^*(r)\phi_j(r')}{|r-r'|}dr'\right) = \epsilon_i\phi_i(r)0. \tag{2.22}$$

While the first two terms represent the Hartree approximation, the last term for the exchange energy contribution arises from the Pauli exclusion principle. Thus, Hartree-Fock approximation represents a remarkable simplification of the original many-body problem. However, electronic energies beyond the exchange interaction (for example, electronic correlation) are absent. This results in an underestimation of the chemical

bond strength. Typically the band gaps are overestimated due to the non-local nature of exchange interaction.

2.4.1 The Hohenberg-Kohn formulation

Around sixty years ago, Hohenberg and Kohn [36, 37] made a phenomenal realization of a practical solution to the Schrödinger equation. They described the density $n(r)$ as the basic variable. They were not the first in the field, but perhaps made the most important contribution. This theorem states that the ground-state density $n(r)$ of a bound system of interacting electrons in an external potential $v(r)$ determines this potential uniquely.

Theorem 1: *For any system of interacting particles in an external potential* $\nu_{ext}(r)$*, the potential* $\nu_{ext}(r)$ *is determined uniquely, except for a constant, by the ground state particle density* $n_0(r)$*.*

Theorem 2: *A universal functional for the energy E[n] in terms of the density n(r) can be defined, valid for any external potential* $\nu_{ext}(r)$*. For any particular* $\nu_{ext}(r)$*, the exact ground state energy of the system is the global minimum value of this functional, and the density n(r) that minimizes the functional is the exact ground state density* $n_o(r)$*.*

Hohenberg and Kohn showed that the electronic density ρ(r) uniquely determines the external potential V (r) of the many-body system within a trivial additive constant [36, 37]. Since the Schrödinger equation can be solved using ρ(r), one can also obtain the wave function. Consequently, the identification of ground state electronic density results in complete information of physical observables of the system, in principle. Simply put, the electronic properties are a functional of the electronic density. Hohenberg and Kohn further demonstrated that the electronic density which minimizes the energy functional is the ground state density. However, in the absence of an exact form of the energy functional, the density functional approach remains impractical.

The energy functional was successfully computed by Kohn and Sham′s non-interacting particle approach. [37] They considered an auxiliary system of non interacting particles with single particle wavefunction ϕ(r) that behaved in the same manner as the electronic density of the many-body system. To achieve this, a new Kohn-Sham energy functional is defined where the kinetic energy of interacting electrons is combined with the correlation

energy, and the non-interacting kinetic energy contribution is written explicitly. Thus, the Kohn-Sham functional is

$$E_{KS}[\rho] = -\sum_i \frac{\hbar^2}{2m}\nabla_i^2 + \frac{1}{2}\int\int \frac{\rho(r)\rho(r')}{|r-r'|}drdr' + E_{xc}[\rho] + E_c[\rho] \tag{2.23}$$

where the first term is the kinetic energy functional of the non-interacting electrons, the second term is the Hartree energy, and the last two terms are the exchange and correlation energy functionals. Conveniently, these are treated together as $E_{xc}[\rho]$. Applying the variational principle, the above energy functional is minimized with respect to the density $\rho(r)$ and wavefunction $\phi(r)$ to obtain the ground state properties in a self-consistent manner. Note that the single particle wave function in Kohn-Sham equations do not represent the actual electronic wave function. However these wave functions are crucial for constructing the electronic density within the self-consistent loops (using the relation $\rho(r) = \sum_i |\phi(r)^2)$.

2.4.2 Exchange-correlation functional

The exact functional for exchange and correlation is unknown since these interactions inherently arise from many-body interactions and can only be approximated up to a certain limit. Thus, the accuracy of a DFT based calculation depends on the assumptions in the underlying exchange-correlation functional $\mathrm{E}_{xc}[\rho]$. The $\mathrm{E}_{xc}[\rho]$ is split into kinetic and potential energy terms. The kinetic energy part includes the energy difference between the non-interacting and correlated system and the potential energy involves energy difference between many-body and Hartree energies. Since both exchange and correlation effects lower the energy of the system by increasing the distance (or decreasing the repulsion) between electrons, the exchange part takes into consideration the Pauli exclusion principle as well as corrects for the spurious repulsive interaction of electron with its density (self-interaction) that is added to the Hartree energy in DFT formalism. The electronic density for real system is inhomogeneous and various approximations for the exchange-correlation functional have been proposed to either reduce the computational complexities or mimic the experimental results.

2.4.3 Local Density Approximation (LDA)

The LDA is the simplest approximation among all exchange-correlation functional which treats the electronic density as locally homogeneous. Thus, the density is locally constant and numerically accurate. The LDA E_{xc} is given as

$$E_{xc}^{LDA}[\rho] = \int \rho(r) E_{xc}^{homo}[\rho] dr \tag{2.24}$$

E_{xc}^{homo} is the exchange-correlation energy for homogeneous electron density. The LDA is successful for ideal metals such as Na, as well for non-homogenous materials where the exchange-correlation effects are short-range and are thus sufficiently captured within LDA. The local nature of LDA does not completely cancel the self-interaction energy and can result in higher energy for obtaining a localized ground state. This can lead to excess delocalization, reduction in band gap and incorrect magnetization. The self-interaction error persists in GGA as well.

2.4.4 Generalized gradient approximation (GGA)

The extent of density localization is increased within GGA by considering the gradient of electronic densities:

$$E_{xc}^{GGA}[\rho] = \int \rho(r) E_{xc}(\rho(r)) dr + \int F_{xc}(\rho(r), \nabla(\rho(r)) dr \tag{2.25}$$

The additional exchange contribution from the enhancement factor F_{xc} results in higher exchange energies than LDA for high and moderate electronic densities, which is consistent with the domination of exchange interaction over correlation for the above density regimes. For low densities, GGA behaves like LDA. In general, GGA improves the binding energy and overestimates the bond length over LDA. Majority of the calculations in this thesis are performed using the Perdew- Burke-Enzerhof functional (PBE), which is a widely used form of GGA [38]. The major drawbacks of the LDA and GGA functionals, especially for semiconductors and transition-metal doped systems, are overcome by the following functionals.

2.4.5 Hybrid functional

The shortcomings of LDA/GGA functional (DFT) and Hartree-Fock method in estimation of band gap can be overcome by hybrid functionals. Typically, the exchange-correlation functional of DFT is mixed with partial exchange contribution from Hartree-Fock method. The Becke-3-Lee-Yang-Parr (B3LYP) [39, 40], PBE0 [41], CAM-B3LYP [42] and Hyde-Scuseria-Ernzerhof [43] hybrid functionals involve separation of the short range Hartree-Fock exchange and a rapid screening of the long-range Hartree-Fock exchange terms. [38, 39, 41–43] Further α, short-range Hartree-Fock exchange is mixed with the β, short-range DFT exchange.

$$E_{xc}^{hybrid} = \alpha E_x^{HF(short)} + \beta E_x^{DFT(short)} + E_x^{DFT(long)} + E_c^{DFT} \tag{2.26}$$

This α and β are derived from the library of the systems and tabulated in the references [42–44].

2.4.6 DFT+U

The treatment of the d, f electrons present in strongly correlated materials is grossly delocalized in LDA/GGA functionals and thus the magnetic moments are underestimated. A repulsive interaction between the localized d, f electrons forces the system to prefer localized states with high-spin configuration. Such an approach is synonymous to the Hubbard model and the repulsive interaction added to DFT is known as Hubbard U. The repulsive U is applied only for d, f electrons, and the otherwise delocalized s, p electrons are treated with conventional DFT approach. The total energy for DFT + U is given by,

$$E^{DFT+U}[\rho(r), n_d] = E^{DFT}[\rho(r)] + E^{U}[n_d] - E_{double}[n_d] \tag{2.27}$$

where the first term calculates the total DFT energy, the second term is the on-site Coulomb repulsion based on the occupancy of the d (or f) orbital, and the last term compensates for the double-counting of repulsive interaction in DFT calculation[38].

2.4.7 Iterative method

As shown in flowchart 2.1, the ground state density is determined by an iterative method. Firstly, an initial density $n_0(r)$ needs to be generated which can be done, for instance, by simply adding single atom densities. From this density generated an effective potential $V_{eff}(r)$ is constructed and further the Kohn-Sham equation is solved, giving rise to a new set of wavefunctions. Through the summation of these wavefunctions, a new density n(r) will then be to constructed which is compared with the original density to check convergence. If the difference falls within the criteria initially set then the calculation ends or else a new input density $n_{k+1}(r)$ is constructed by mixing the output density with previous densities. By doing the mixing efficiently, the convergence will be as effective as possible. Using the output density directly as input density will result in very slow and oscillating convergence if any. When the output density comes sufficiently close to the input density $n_k(r)$, the calculation converges, and the total energy, E[n(r)], forces, etc., can then be calculated.

2.4.8 Basis set

To solve Kohn-Sham equations, the wavefunction needs to be expanded in a basis. This expansion can be done using different types of basis sets. For example, it can be Gaussian functions, plane wave, atomic orbitals or a mixture of two or more types of basis set. For all the DFT calculations presented in this thesis, the wavefunctions were expanded using plane wave basis and localized (Gaussian) wave basis set $e^{i(k+G)r}$ ($e^{\alpha x^2}$, α is the coefficient), where k is the wavevector at which Kohn-Sham equations are solved and G reciprocal lattice vector. The plane wave becomes discrete only when periodic boundary conditions are used. The energy parameter E_{cut}, which determines the number of plane waves or the size of the basis set employed, is given by the equation:

$$\frac{\hbar\,|k+G|^2}{2m_e} < E_{cut}. \tag{2.28}$$

In practice this is determined by checking its convergence with the quantity of interest. There are several advantages associated with using a plane wave, like: (i) Since there is the absence of Pulay forces [45], as the basis is independent of atomic position, the forces can be conveniently calculated using the Hellman-Feynman theorem [46], (ii) A

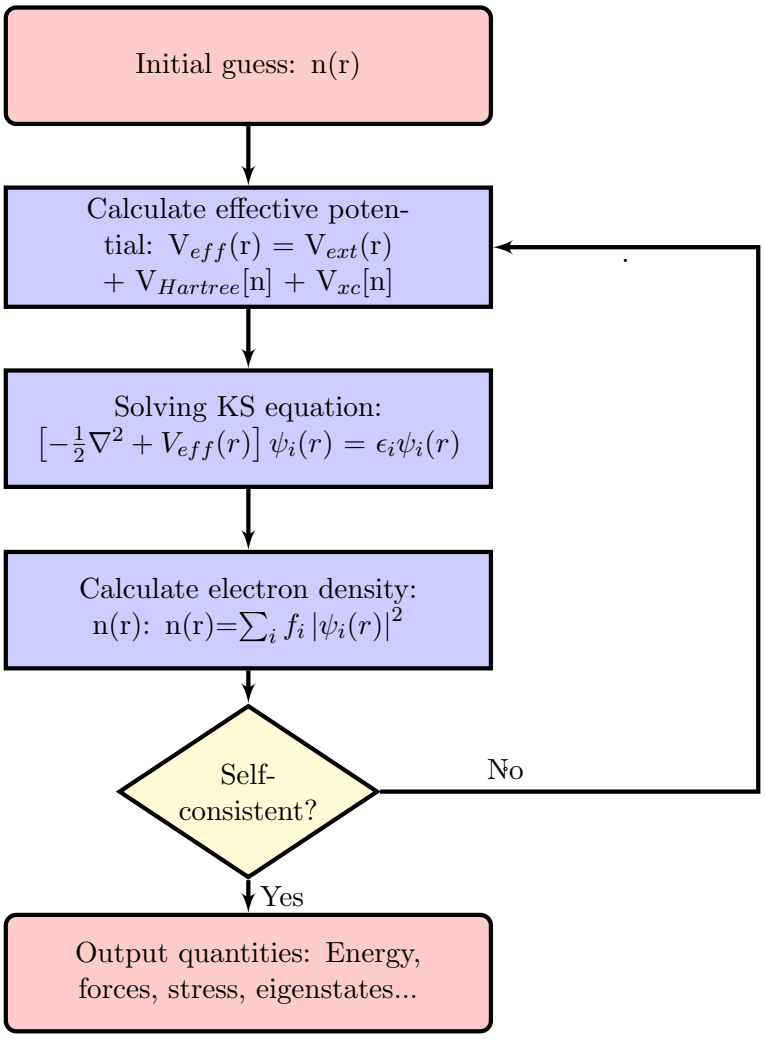

FIGURE 2.1: Schematic representation of the self-consistent loop for the solution of Kohn-Sham equations.

single parameter controls the quality of the basis set and (iii) it is easy to implement while coding.

However, a disadvantage associated with using a plane wave basis is that a large number of plane waves are required to expand the wavefunctions in the core region, since the core electrons wavefunctions are highly peaked, and valence electron wavefunctions have several oscillations. This problem is rectified using pseudopotentials as described below.

2.4.9 Pseudopotentials

The effective potential experienced by the valence electrons when the core electrons are frozen is called the pseudopotential. It is obtained by pseudizing the wavefunction of

the valence electrons, i.e. removing the oscillations of the wavefunction of the valence electrons in the core region and replacing it with a smooth function. The pseudo and all electron wavefunction after a particular value of the radial distance from the center of the nucleus r_c. r_c is chosen so that the last node of the all electron wave function lies within it. If the same pseudopotential can be used in different environments of the atom, the pseudopotential is said to be transferable. As r_c increases, the number of plane waves required to represent a pseudo wavefunction generally decreases, but the transferability also decreases. There are many types of pseudopotential like norm-conserving, ultrasoft, etc.

In norm-conserving pseudopotentials, in the core region, the norm of the pseudo-wavefunction is equal to the norm of the all electron wavefunction thereby ensuring the transferability of the pseudopotential. Relaxation of the norm-conservation condition leads to Vanderbilt's ultrasoft potential [47] which allows one to use a very low energy cut-off. However, upon doing so the orthonormality requirements of the atomic orbitals and the norm conservation is lost. The issue of the orthonormality requirements can be solved by considering a generalized eigenvalue problem, where a generalized orthogonality constraint is expressed in terms of an augmentation charge that is localized within the core regions.

2.4.10 Hellman-Feynman Theorem

To determine the ground state structure of a system one needs to minimise the forces and stresses. Hence it is necessary to calculate the forces acting on the individual atoms and the stresses acting on the unit cell, so as to optimize the atomic positions and lattice vectors of the unit cell. When the forces acting on the atoms are zero, it signifies that the atomic coordinates are relaxed. Zero stress implies that the unit cell lattice vectors have been optimized.

The forces are calculated using the Hellman-Feynman [46] theorem that is expressed as:

$$F_I = -\frac{\partial E}{\partial R_I} \tag{2.29}$$

Where $E = \langle\phi|\hat{\mathcal{H}}_e|\phi\rangle + E_{II}$. The force can be written as

$$F_I = -\frac{\partial E}{\partial R_I} = -\langle \frac{\partial \phi}{\partial R} | \hat{\mathcal{H}}_e | \phi \rangle - \langle \phi | \frac{\partial \hat{\mathcal{H}}_e}{\partial R} | \phi \rangle - \langle \phi | \hat{\mathcal{H}}_e | \frac{\partial \phi}{\partial R} \rangle - \frac{\partial E_{II}}{\partial R_I} \tag{2.30}$$

Since at the exact ground state the energy is at an extreme point with respect to any variation in the wavefunctions, the second and third terms will vanish.

$$F_I = -\langle \phi | \frac{\partial \hat{\mathcal{H}}_e}{\partial R} | \phi \rangle - \frac{\partial E_{II}}{\partial R_I} \tag{2.31}$$

This is often called the Hellmann-Feynman theorem (2.31) or the force theorem. Further, it is possible to show that F_I only depends on the electron density and the positions of the nuclei

$$F_I = -\int dr n(r) \frac{\partial V_{ext}(r)}{\partial R_I} - \frac{\partial E_{II}}{\partial R_I}. \tag{2.32}$$

2.4.11 Solving KS equations

The Kohn-Sham secular equation can, of course, be solved directly using standard linear algebra diagonalization. For large systems, this will be slow and a substantial bottleneck in the solution of the Kohn-Sham equations, especially for a system with very large basis sets, like in the case of plane waves, even with the use of pseudo-potentials. Instead of the direct diagonalization of the problem, an iterative solution method can be used. A direct diagonalization scales as $\mathrm{N}_e\mathrm{N}_b$ where N_e is the number of eigenstates in the system and N_b is the size of the basis set.

2.5 Path Integral Molecular Dynamics (PIMD)

Up to now, we discussed how to treat electrons quantum mechanically. However, ions (nucleus) are still treated as classical point particles. In this section, we will demonstrate path integral formalism for quantumness of the system (mainly nuclear wavefunction).

Feynman path integrals (FPI): Feynman path integrals turns a quantum mechanical problem into a series of classical problems. The action is defined as $\int Ldt$, L is the Lagrangian. Classically, a particle follows a single path from its starting point "x" to a new position "x′", corresponding to the path of least action [48, 49]. Using the path integral representation of quantum mechanics the particle, the particle samples all paths from "x" to "x′ " simultaneously, where each path has a given amplitude. The probability that a particle at position x will later be observed at position "x" is the square modulus of the sum of these interfering amplitudes.

PIMD: The canonical one particle partition function can be written as,

$$Z(\beta) = Tr(e^{-\beta H}) = \int dx \langle x|(e^{-\beta H})|x\rangle \tag{2.33}$$

The Hamiltonian in the exponent is the sum of two non-commutative operators, the KE and PE. Therefore, to separate the term into the product of two non-coupled exponentials, the $Trotter$ expansion must be used

$$e^{\lambda(A+B)} = lim_{P\longrightarrow\infty}\left[e^{\frac{\lambda}{2P}A}e^{\frac{\lambda}{P}B}e^{\frac{\lambda}{2P}A}\right] \tag{2.34}$$

This expression is only exact in the limit P goes to ∞. The error in the Trotter expansion is order τ^2 where $\tau \equiv \frac{\beta}{P}$. With this approximation, one is lead to the following expression for the partition function,

$$Z_P(\beta) = \left(\frac{mP}{z\pi\beta\hbar^2}\right)^{\frac{P}{2}} \int dx_1 dx_2 ... dx_P \left(e^{-\sum_{i=1}^{P}\left[\frac{mP}{2\beta\hbar^2}(x_{i+1}-x_i)^2+\frac{\beta}{P}\phi(x_i)\right]}\right)_{x_{P+1}=x_1} \tag{2.35}$$

This expression is known as the discretized path integral. This Hamiltonian looks precisely like a set of P coupled oscillators in some external potential U_{eff} where,

$$U_{eff}(x_1, x_2, ..., x_P) = \sum_{i=1}^{P} \left[\frac{mP}{2\beta\hbar^2}(x_{i+1} - x_i)^2 + \frac{1}{P}\phi(x_i) \right]_{x_{P+1}=x_1} \tag{2.36}$$

However, in order to perform a molecular dynamics simulation on this Hamiltonian, we must add in conjugate momenta. Doing so makes the partition function,

$$Z_P(\beta) = N \int dp_1 dp_2 ... dp_P \int dx_1 dx_2 ... dx_P e^{-\beta \left[\sum_{i=1}^{P} \frac{P_i^2}{2m_i} + U_{eff}(x_1, x_2, ..., x_P) \right]} \tag{2.37}$$

where N is a constant. Notice that since these additional degrees of freedom are quadratic and decoupled (Gaussian), and thus merely change the overall normalization factor, not the overall dynamics. The effective Hamiltonian becomes,

$$H(p, x) = \sum_{i=1}^{P} \left[\frac{P_i^2}{2m_i} + \frac{1}{2} m\omega_p^2 (x_{i+1} - x_i)^2 + \frac{1}{P}\phi(x_i) \right]_{x_{P+1}=x_1} \tag{2.38}$$

We are now ready to perform molecular dynamics simulations. There are now P "beads" per quantum mechanical particle. Each bead can be treated as a classical particle in a molecular dynamics simulation with the interaction U_{eff}. Note that every bead interacts only with the two beads that are nearest neighbors in **imaginary time**. Hence the one particle is represented by a necklace with P beads. The number of beads ($P \to \infty$) large will give the quantum picture. However, this is an impossible situation to compute. Now thermostat can reduce the number of beads to the finite number (which can compute within reasonable resources) still maintaining the quantum picture.

2.5.1 Thermostat

As we discussed the introduction of PIMD, MD simulation is in the constant energy micro-canonical ensemble. A thermostat is usually required to sample the partition function at a constant temperature canonical ensemble. Note that necessarily this is unphysical since one is adding degrees of freedom to the system which are not truly present and changing the conserved quantity (the Hamiltonian). Nevertheless, there has been much success with correctly reproducing the correct canonical distribution through thermostatting. We discuss Langevin thermostat and Generalized Langevin thermostat [50]. The Langevin thermostat makes use of the Langevin Equation to mimic a heat

bath and it thus stochastic. It employs the Einstein relation between friction and the random force to set the temperature.

Langevin Thermostat This thermostat consists of a friction term and a thermal noise term,

$$\frac{\partial}{\partial t} q_i^{(k)} = \frac{p_i^{(k)}}{m_i} \tag{2.39}$$

$$\frac{\partial}{\partial t} p_i^{(k)} = -m_i \omega_k^2 q_i^{(k)} - \gamma^{(k)} p_i^{(k)} + \sqrt{\frac{2 m_i \gamma^{(k)}}{\beta_n}} \xi_i^{(k)}(t) \tag{2.40}$$

where $\gamma^{(k)}$ are the friction coefficients and $\xi_i^{(k)}(t)$ is a normally-distributed random force. Here our conserved quantity changes from the total energy of the system to the total energy minus the accumulated heat absorbed by the thermostat. The Langevin thermostat ensures canonical dynamics no matter the value of $\gamma^{(k)}$, though better values should lead to faster convergence. The optimal values of $\gamma^{(k)}$ can be determined recursively [49]. However, for our purposes, this made little difference to the efficiency of the simulation. Thus we let each $\gamma^{(k)}$ be unity.

Incorporation of Generalized Langevin Equation (GLE)

Another version of the langevin thermostat is generalised lagevin equation where the friction term is memory dependent and as a result of fluctuation-dissipation theorem, the random noise term also becomes memory dependent. But keeping a track of what happened in the long past is difficult to handle. So, fictitious degrees of freedom are introduced to make the equation memory independent. This thermostat can be used to sample the quantum fluctuations to produce the nuclear quantum effect. The system is in contact with a quantum thermal bath, where the dynamics follow a generalized Langevin equation (GLE) and the vibrational delocalization is mimicked by a quantum thermostat. In such an approach, the otherwise white noise spectrum of the Fourier Transform of the stochastic force correlation function is filtered (colored [50]) in such a way that it ends up resembling the spectral density of the correlation function for a quantum harmonic oscillator with ZPE contribution included.

More strictly, in GLE, the particle of unit mass, which position is described by the generalized coordinate q, with a conjugate momentum p, and is subject to a potential

V(q), yields the following equations of motion:

$$\dot{q} = p(t) \tag{2.41}$$

$$q(t) = -V'(q) - \int_{-\infty}^{t} K(t-s)p(s)ds + \xi(t) \tag{2.42}$$

where $\xi(t)$ is a time-correlation function of the random force and K(t), is the memory kernel, introducing the dependence of the system evolution on its history in terms of a non-Markovian stochastic differential equation. Such definition, however, requires the use of differential equations, leading to a serious numerical challenge. Alternatively, one may map the non-Markovian dynamics onto an equivalent, Markovian dynamics in an extended space "n", by introducing auxiliary fictitious momenta "s", linearly coupled to the physical momentum p:

$$\dot{q} = p(t) \tag{2.43}$$

$$\begin{pmatrix} \dot{p} \\ \dot{s} \end{pmatrix} = \begin{pmatrix} -V'(q) \\ 0 \end{pmatrix} - \begin{pmatrix} a_{pp} & a_p^T \\ a_p & A \end{pmatrix} \begin{pmatrix} \dot{p} \\ \dot{s} \end{pmatrix} + \begin{pmatrix} b_{pp} & b_p^T \\ b_p & B \end{pmatrix} (\xi) \tag{2.44}$$

where s is the vector of n additional degrees of freedom; ξ denotes n+1 dimensional vector of uncorrelated Gaussian numbers [17]; a_{pp} stands for a friction coefficient and b_{pp} denotes the intensity of the random force, both linked by the so-called **fluctuation-dissipation** (FD) theorem ($\mathbf{b_{pp}^2 = 2a_{pp}mk_BT}$). The matrices in Equation(2.43),(2.44) are related by the so-called drift matrix C:

$$A_pC_p + C_pA_p^T = B_pB_p^T \tag{2.45}$$

Where $A_p = \begin{pmatrix} a_{pp} & a_p^T \\ a_p & A \end{pmatrix}$ and $B_p = \begin{pmatrix} b_{pp} & b_p^T \\ b_p & B \end{pmatrix}$. This allows one to predict the response properties analytically.

For a quantum thermostat, it is, however, required to relax the fluctuation-dissipation theorem, which leads to non-equilibrium GLE dynamics. This may be realized by noting that the kinetic energy distributions of both classical and quantum harmonic oscillator take the form of a Gaussian, with the widths differing only in the standard deviation.

While the effective temperature can be defined as:

$$T^*(\omega) = \frac{\hbar\omega}{2k_B} coth\left(\frac{\hbar\omega}{2k_BT}\right) \tag{2.46}$$

one can take advantage of GLE dynamics by thermostatting the different vibrational modes present in the system at different effective temperatures T^*. In such a way, the kinetic energy distribution with deviation

$$\sigma_q^2 = \frac{\hbar}{2m\omega} coth\left(\frac{\hbar\omega}{2k_BT}\right) \tag{2.47}$$

can be imposed by using purely classical simulations.

After PIGLET simulations [49], we have collected random snapshots from the trajectories and then computed spectroscopic properties (*viz* TDDFT). The time-dependent density functional theory discussed in the next section 2.6.

2.6 TDDFT

Density functional theory has proven to be very useful for the description of ground state properties of a system. For many applications [51–54], however, the calculation of the excited states of a system is essential. Time-dependent treatment has taken place after a few years of the development of K-S equations. Runge and Gross proved a theorem stating that the time-dependent density uniquely determines the time-dependent external potential and vice versa in 1984.

Theorem *For every single-particle potential V(r,t) which can be written into a Taylor series with respect to the time coordinate around t=t_0, a map G:V(r,t) →n(r,t) is defined by solving the time-dependent Schrödinger equation with a fixed initial state $\phi(t_0)$ =ϕ_0 and calculating the corresponding densities n(r,t). This map can be inverted up to an additive merely time-dependent function in the potential.*

This theorem can be seen as the similar of the Hohenberg-Kohn theorems for the time-independent case. So again, if the exact time-dependent electron density of a system is known, all other properties of the system can be calculated. The deviation from "3N" spatial coordinates to three coordinates is the same as for the time-independent case [55–57].

A system, initially in its ground state, subject to a time-dependent perturbation will lead to a modified effective potential

$$V_{eff}(\bar{r},t) = V(\bar{r},t) + \int \frac{\rho(\bar{r}',t)}{|r-\bar{r}'|} d\bar{r}' + V_{xc}(\bar{r}',t) \tag{2.48}$$

which can be used to derive the time-dependent Kohn-Sham equation

$$\left[-\frac{1}{2}\nabla^2 + V_{eff}\right]\psi_i(\bar{r}',t) = i\frac{\partial}{\partial t}(\bar{r}',t) \tag{2.49}$$

The exchange-correlation potential here is the functional derivative of the time-dependent exchange-correlation functional $\mathrm{A}_{xc}\,[\rho]$, which is approximated by $\mathrm{E}_{xc}\,[\rho \mathrm{t}]$ (the exchange-correlation functional of time-independent Kohn-Sham theory) for the density at fixed t

$$V_{xc}(\bar{r}',t) = \frac{\delta A_{xc}[\rho]}{\delta\rho(\bar{r}',t)} = \frac{\delta E_{xc}[\rho_t]}{\delta\rho(\bar{r}')} \tag{2.50}$$

This is known as the adiabatic (low frequency) approximation. The time-dependent Kohn-Sham orbitals give the true time-dependent charge density

$$\rho(\bar{r}',t) = \sum_{i\sigma} f_{i\sigma}|\psi_{i\sigma}(r,t)|^2 \tag{2.51}$$

The linear response to a perturbation $\omega(\mathrm{t})$ is given by

$$\delta\rho_\sigma(\bar{r}',\omega) = \sum_{ij} \psi_{i\sigma}(\bar{r})\delta P_{ij\sigma}(\omega)\psi^*_{j\sigma}(\bar{r}) \tag{2.52}$$

where

$$\delta P_{ij\sigma}(\omega) = \frac{f_{j\sigma} - f_{i\sigma}}{\omega - (\epsilon_{i\omega} - \epsilon_{j\omega})} \times \left[\omega_{ij\sigma}(\omega) + \sum_{kl\tau} K_{ij\sigma kl\tau}\delta P_{kl\tau}\right] \tag{2.53}$$

is the response of the Kohn-Sham density matrix in the basis of the unperturbed molecular orbitals. The coupling matrix K describes the linear response of the self-consistent field ν^{SCF} (the last two terms in Equation 2.48) to changes in the charge density.

Since the dynamic polarizability, $\alpha(\omega)$, describes the response of the dipole moment to a time-dependent electric field, it may be calculated using the response of the charge density. For the time-dependent, electric perturbation

$$\omega(\bar{r}', t) = z\epsilon_z(t) \tag{2.54}$$

where ϵ_z(t) is the applied field strength, the xz-component of the dynamic polarizability cab be expressed as

$$\alpha_{xz}(\omega) = \frac{2\bar{x}}{\sqrt{P}[\Omega - \omega^2 1]\sqrt{P}}\bar{z} \tag{2.55}$$

by using equation 2.53. Here we have defined

$$P_{ij\sigma_k l\tau} = \frac{\delta_{\sigma,\tau}\delta_{i,k}\delta_{j,l}}{(f_{k\tau} - f_{l\tau})(\epsilon_{l\tau} - \epsilon_{k\tau})} > 0 \tag{2.56}$$

and

$$\Omega_{ij\sigma,kl\tau} = \delta_{\sigma,\tau}\delta_{i,k}\delta_{j,l}(\epsilon_{l\tau} - \epsilon_{k\tau})^2 + 2\sqrt{(f_{i\sigma} - f_{l\tau}(\epsilon_{j\sigma} - \epsilon_{i\sigma})} \times K_{ij\sigma,kl\tau}\sqrt{(f_{k\tau} - f_{l\tau})(\epsilon_{l\tau} - \epsilon_{k\tau})} \tag{2.57}$$

According to sum-over-states relation,

$$\bar{\alpha}(\omega) = \sum_I \frac{f_I}{\omega_I^2 - \omega^2} \tag{2.58}$$

the poles of the dynamic polarizability determine the excitation energies, ω_I , and the residues, f_I, determine the corresponding oscillator strengths. A careful comparison of Eqs. (2.55) and (2.58) shows that excitation energies and oscillator strengths can be obtained by solving the matrix eigenvalue problem

$$\Omega \bar{F}_I = \omega_I^2 \bar{F}_I \tag{2.59}$$

where oscillator strengths are obtained from the eigenvectors $\bar{\mathrm{F}}_I$.

Chapter 3

Nuclear Quantum Effects in an HIV/Cancer Inhibitor: The Case of Ellipticine in water

3.1 Introduction

Ellipticine (5,11-dimethyl-6H-pyrido[4,3-b]carbazole) is a natural plant alkaloid that exhibits both anti-HIV activity [58, 59] and anti-cancer [60–62]. Due to its potential applications in pharmaceutical, understanding its physical and chemical properties have been of immense interest in biochemical research [63–66]. Though it is well established that ellipticine shows high toxicity against tumor cells, there are very few clinical trials of ellipticine because of its low solubility in both aqueous media and organic solvents [67, 68]. With the development of new drug delivery techniques, it has been possible to deliver ellipticine in vitro by covalently linking them with polymers or peptides [69–71].

In order to develop more efficient ways of delivering ellipticine to the tumor cells, it is important to understand the mechanism through which ellipticine is delivered to its target. A common way to experimentally understand the mechanism of drug delivery and to monitor it is to observe the changes in the photophysical properties of the drug molecule that is sensitive towards its environment. Some recent studies show that ellipticine exhibits interesting photophysical properties, particularly in the presence of different protic solvents [72–74]. In the gas phase, ellipticine exists in its normal form

[73], as shown in Figure 3.1. Depending on the polarity of the solvent and their ability to exchange protons, ellipticine can either exist in its normal form (only pyrrole N forms an N-H bond), a protonated form [75](both the pyrrole N and pyridine N forms N-H bonds), the tautomeric form (only pyridine N forms an N-H bond) or a linear combination of one or more of these forms [73, 75, 76].

One of the main techniques that have been used to probe the optical properties of ellipticine and to infer the changes in its protonation state is fluorescence studies [73]. Several different experiments have shown that in polar solvents ellipticine can be characterized by either dual fluorescence or a single fluorescence peak [75]. Although there is a consensus that the two peaks arise from the presence of two types of species/forms, of which one of them is the normal one, there is a disagreement on the molecular origin of the second peak. Moreover, possible mechanism of its formation is not well understood and also quite contentious [73, 75, 76]. In particular, Miskolczy *et al.* have argued that the second peak originates from the protonated form of ellipticine, formed due to an excited state proton transfer from the solvent. Their conclusion was based on the fact that they observed dual fluorescence even when they replace the H atom bound to the pyridine N with a methyl group. On the other hand, Banerjee *et al.*, based on time-resolved fluorescence studies, have interpreted this peak in the emission spectra as originating from the tautomeric form of ellipticine formed through solvent mediated excited state proton transfer from pyrrole N to pyridine N. According to them the formation of the tautomer involves solvent reorganization around ellipticine resulting in cyclic solvated species that is followed by rapid proton transfer along the chain. It was also suggested that in the case of ethylene glycol, both ground state and excited state that are solvent mediated tautomerization reactions, contribute to the long wavelength emission.

In contrast, there are very few studies of ellipticine's photophysical properties in water, which is the most common solvent in a biological membrane. Sureau *et al.* found that the fluorescence spectra of ellipticine in water is very sensitive to its pH [77]. From their pH-dependent study of the fluorescence spectra they showed that at high pH (12.2) and at low pH (6.0) there is only one fluorescence peak at about 430 and 520 nm, respectively. On varying the pH in this range, they observed that the intensity of the 520 nm peak decreases and that of the 430 nm peak increases with increase in pH. At intermediate pH values (about 7.4) both these peaks coexist. From these measurements, they determined

the pK_a of ellipticine to be around 7.4. It was also hypothesized that the long wavelength emission peak originated from the protonated form of ellipticine [77].

Polar solvents which form the medium in which ellipticine features interesting photophysical properties are characterized by hydrogen bonding interactions. Hence, the molecular details of the hydrogen bonding between ellipticine and the surrounding solvent is likely to play an important role in tuning the optical properties. One rather important aspect of hydrogen bonding that is receiving growing interest is the role of nuclear quantum effects (NQE) in hydrogen-bonded systems [10, 19, 78, 79]. In the last two decades, numerous theoretical, computational and experimental works have elucidated the role of NQE in organic, inorganic, aqueous systems, and biological systems consisting of light hydrogen atoms [16, 18, 80].

An aspect of the role of NQE that has been examined much less in biological systems is their effect on perturbing electronic and optical properties. The effect on these properties is anticipated given the large changes that NQE induces on structural fluctuations. Recently, Giberti *et al.* studied the effect of quantum fluctuations on the electronic properties of protonated water [81]. Their simulations show that the quantum fluctuations result in the introduction of new electronic states that were previously inaccessible, thereby altering the band gap of water. The role of quantum effects on optical spectra have been examined theoretically for nucleobases [82], inorganic clusters [83] and also some biological model systems [84, 85]. The common feature in all these studies is that NQE tunes the broadening of the spectra as well as the absorption peaks.

In this work, we examine the role of NQE in a highly relevant biological system, the HIV and cancer inhibitor ellipticine. Given that this molecule functions in an aqueous environment in the cell, a deeper understanding of the coupling of its structural and electronic properties in a hydrogen-bonded environment such as water, is crucial. As a first step towards this, here, using both classical molecular dynamics (MD) and path-integral ab initio MD we examine how hydrogen bond interactions and quantum fluctuations of the nuclei alter the optical properties of ellipticine. Moreover, since isotope effects (replacing H by D) are an important experimental tool to probe the significance of NQE [10, 19, 86–88] we also study the changes in spectra induced by isotopic substitution, hoping to bridge the gap between theory and experiments.

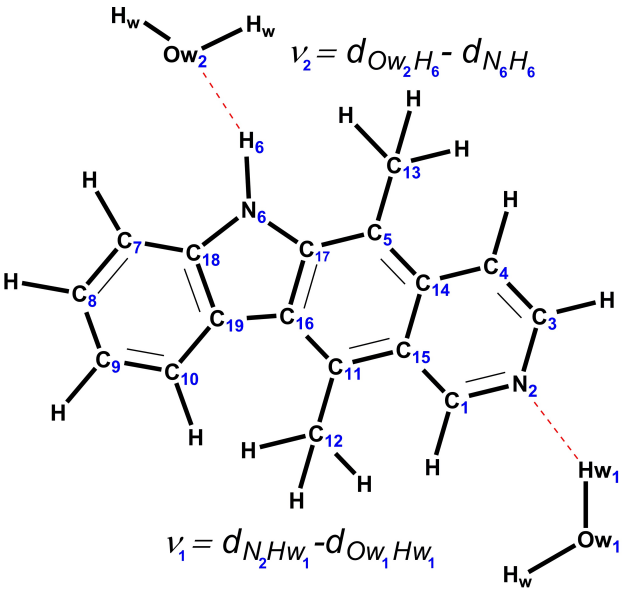

FIGURE 3.1: Schematic of ellipticine molecule in its normal form. Also shown are the proton donation (υ_1) and acceptance (υ_2) coordinates. d_{XY} in the figure denotes distance between atoms X and Y.

The rest of the chapter is organized as follows. In Section 3.2 we describe the details of the different simulation techniques used in this work and describe to calculate time-averaged absorption spectra. Section 3.3.1 contains the results of NQEs on the structure of ellipticine and a common biological solvent (water). In Section 3.3.2 we show the changes in the absorption spectra of hydrated ellipticine due to NQE. We also separate out the effect of solvation and NQE on the absorption spectra. Finally, in Section 3.4, we end with some discussion and conclusions of our results.

3.2 Computational details

In order to study the influence of NQE on structure, dynamics and optical properties of ellipticine in water, we have used different levels of theory. The details of the same are as follows:

3.2.1 Classical molecular dynamics simulations

We have carried out classical MD simulations using the GROMACS-4.5.5 software (with double precision). The water molecules are explicitly represented and described by the TIP3P water model. [89] The MD simulations were based on the general amber force field

(GAFF) [90] parameters. Ellipticine was optimized followed by Merz-Kolmann charge calculation [91] using Hartree-Fock theory with 6-31G(d) basis set using Gaussian 09 [92]. Antechamber module of AMBERTools [93] was used for calculating restrained electrostatic potential charge (RESP) [94] and generation of General Amber Force Field (GAFF) [90]. Finally, the coordinates and topology were converted to GROMACS format using amb2gmx.pl program [95].

Ellipticine was placed in a cubic box of length 31.5 Å and solvated with 983 TIP3P water molecules. For the NVT simulations, a constant temperature of 300 K was maintained by coupling the system to a thermal bath with the Andersen algorithm and a time constant of 1 ps, whereas for the NPT simulations a constant pressure of 1 bar was maintained using the Berendsen barostat [96] with isotropic scaling and a time constant of 2 ps. All Lennard-Jones interactions were cut off at 10 Å and a particle mesh Ewald correction to the long-range electrostatic contribution was applied. The integration step was set to 2 fs and the X-H (X, heavy atom) stretching modes were frozen using LINear Constraint Solver (LINCS) algorithm [97].

The protocol for the classical simulations was as follows: after 2000 steps of energy minimization, we performed simulated annealing (annealing time of 100 ps) under NPT conditions to heat the system to 300 K. This was followed by equilibration at 300 K for 100 ps in the NPT ensemble. Starting from the equilibrated system, MD trajectories were recorded for 10 ns in the NVT ensemble. The last 8 ns of productions were used for analysis.

3.2.2 Born-Oppenheimer molecular dynamics (BOMD) and PIGLET simulations

In the BOMD simulations, the nuclei are treated classically, while the electrons are treated at the level of density functional theory. Performing these simulations for the enormously large system mentioned in the previous section is prohibitively expensive. Hence, we extract a configuration from the end of the classical MD runs and truncated the solvent molecules till second solvation shell based on where the radial distribution function plot plateaus (Figure A.1 in Appendix A). The resulting system how consists of one ellipticine molecule surrounded by 87 water molecules placed in a cubic box length 14.9 Å. Figure A.1 shows that the results of the g(r) between the center of mass of

ellipticine and O of water obtained from the classical molecular dynamics simulations. The first and second solvation shells are at 5.4 and 7.45 Å (blue dashed lines, Figure A.1) respectively. This procedure likely creates some broken hydrogen bonds at the boundary. However, we found that the system equilibrates rather quickly within a few picoseconds. Furthermore, as we will see later, in this work, the periodic BOMD simulations, in any case, are primarily used to extract *cluster configurations* for computing the absorption spectra.

These calculations were performed using the Quickstep module of the CP2K package [98]. The electronic exchange and correlation energies were described using the Becke-Lee-Yang-Parr (BLYP) exchange-correlation functional [40]. The core electrons have been described using Goedecker-Teter-Hutter (GTH) pseudopotentials [99]. Wave functions were expanded in the Gaussian polarized triple-zeta split-valence (TZVP) basis set, whereas the electronic density was represented using an auxiliary plane wave basis, with a kinetic energy cutoff of 300 Ry. A convergence criteria of 5×10^{-7} a.u. was used for the optimization of the wavefunction. The D3 Grimme dispersion corrections for the van der Waals interactions were used [100]. The simulations were performed within the NVT ensemble at 300 K temperature using the canonical-sampling velocity-rescaling thermostat (CSVR) [101]. The simulations were run for 55 ps. Integrations were performed with 0.5 fs time step. The system equilibrated within the first 5 ps of the run. Snapshots were selected from the remaining 50 ps trajectory for further analysis.

Starting from a random snapshot from the equilibrated BOMD trajectory, we begin the PIMD simulations with a generalized Langevin equation (GLE) based colored-noise thermostat for incorporating the quantum effects [15, 50]. The purpose of the coloured noise thermostat with PIMD (PIGLET) is to enhance the sampling of the kinetic and potential energy terms and thus reduce the number of beads necessary for the PIMD simulations. Based on literature reports [17, 84], we have used six beads for the path integral simulations. The total simulation was run for 8 ps with a time step of 0.5 fs. The first 2 ps of the run was treated as equilibration and snapshots from the last 5 ps were used for further analysis. To achieve this we have used a recently released code i-PI [17]. In the rest of the chapter, we will refer to the classical simulations as BOMD and the PIMD simulations as PIGLET.

3.2.3 Excited State Calculations

To understand the effect of NQE on the optical properties of ellipticine in water, we have computed the time-averaged absorption spectra using snapshots from both the BOMD and the PIGLET trajectories. In order to compute the absorption spectra from our BOMD simulations, we randomly select 90 snapshots from the BOMD trajectory, to compute the absorption spectra of each using time-dependent density functional theory (TDDFT) and the final spectrum is the average of the spectra of these 120 snapshots. A convergence test of the absorption spectra as a function of the number of snapshots showed that one can obtain a well-converged spectra with 90 snapshots (figure A.9 in Appendix A). The absorption spectra from the PIGLET simulations were constructed using a formalism previously developed by Marx and co-workers [83]. 20 frames were selected randomly from the PIGLET run were used to compute the spectra. For each frame, all 6 beads were used.

Due to the strong interaction between the solvent and solute molecules, the absorption spectra is sensitive to whether the solvent molecule is explicitly included in the calculations. Hence to compute the absorption spectra for each snapshot, we cut out geometries from the ground state molecular dynamics trajectory ("finite cluster" model) and perform TDDFT calculations. However, performing TDDFT calculations with ellipticine and 87 water molecules to obtain a spectrum for an energy window of about 2-6 eV (25 empty electronic states) is very expensive. Hence there is a need to strike a balance between computational cost and accuracy. A convergence test of the absorption spectra of an individual snapshot as a function of the number of water molecules showed that at least 26 explicit water molecules are necessary for accurately computing the spectra. Details regarding the choice of the number of water molecules and their effect on the spectra are given in Appendix A.

Moreover, recent studies by Isborn *et al.* [102] showed that TDDFT calculations for π-π^* transitions in solvated conjugate molecules using the above mentioned "finite cluster" model often results in spurious low lying charge transfer (between solvent and molecule) excitations due to the partial negative charge acquired by the water molecules at the edge of the solvation shell because of the abrupt breaking of the H-bonds between the water molecules during the snapshot curving process. Therefore one needs to perform careful studies of the effect of edge waters on the absorption spectra. We performed

a thorough study of the above mentioned effect on our system, details of which are given Appendix A. Our calculations suggest that the spurious effects on the absorption spectra due to the "finite cluster" can be circumvented by using a PCM model along with explicit water molecules. Hence the explicit waters were then surrounded by a polarizable continuum model (PCM) with a dielectric constant of 80.

The TDDFT calculations were performed on each snapshot using the Davidson algorithm as implemented within Gaussian 09 Revision D.01 software [92]. The wave functions are expanded in a 6-311++g(d,p) basis set. It is well known that the absorption spectra is sensitive to the theoretical method chosen to compute it [103] and for TDDFT in particular, it is sensitive to the choice of the exchange-correlation functional and usually hybrid functionals are preferred over the most commonly used functionals derived from generalized gradient approximations [44]. We have used different flavors of hybrid functionals, namely B3LYP [39, 40], PBE0 [41], HSEH1PBE [104], and Coulomb-attenuated method B3LYP (cam-B3LYP) functional [42] to study the dependence of the spectra on the type of exchange-correlation functionals used. In this chapter, we present the results of B3LYP only, while the results obtained with other functionals are given in Appendix A.

To separate out the role of NQE and solvation on the spectra, we computed the absorption spectra in three ways: (a) the spectra of the dehydrated ellipticine molecule where we remove all the water molecules, (b) the spectra of ellipticine molecule with implicit solvent, i.e. solvent effects are included through a continuous PCM model [105] and (c) spectra containing ellipticine, 26 water molecules, and the PCM model.

3.3 Results and discussion

3.3.1 Nuclear Quantum effects on structural properties of ellipticine in water

The normal form of ellipticine contains two nitrogen atoms, namely a pyridine N (labeled as N_2 in Figure 3.1) and a pyrrole N (labeled as N_6 in Figure 3.1) bonded to an H atom. In polar solvents, the former might act as a proton acceptor while the latter as a proton donor. In order to determine whether proton transfer occurs in the ground

state, we have defined proton acceptance and donation coordinates and monitored the same throughout the MD simulations. The proton acceptance coordinate is defined as $\upsilon_1 = d_{N_2Hw_1} - d_{Ow_1Hw_1}$, where the subscript w denotes that the H/O atom belonging to the solvent water molecule, $d_{N_2Hw_1}$ is the distance between the pyridine N and the closest H atom of the nearest solvent molecule and $d_{Ow_1Hw_1}$ is the distance between O and H bond length in the same solvent molecule (Figure 3.1). On similar ground, the proton donation coordinate is defined as $\upsilon_2 = d_{Ow_2H_6} - d_{N_6H_6}$. Negative values of υ_1/υ_2 indicate that ellipticine has accepted/donated a proton from/to the solvent. While υ_1 is related to the fluctuations of the protons in the solvent, υ_2 is related to the fluctuation of the proton attached to the pyrrole N in ellipticine.

Figure 3.2 shows that the probability distribution function (PDF) of the two proton transfer coordinates in water as traced by the trajectories of classical and quantum nuclei simulations. For BOMD and PIGLET simulations, the PDF of υ_1 is peaked between 0.7 and 0.8 Å, depending on the type of simulation suggesting that most of the time during our simulations the proton of the water molecule is covalently bonded to the O and interacts with the pyridine N through H bonding. Likewise, the PDF of υ_2 is peaked around 0.9 and 1.1 Å, suggesting that the proton attached to the pyrrole N is covalently bonded to ellipticine mostly. Figure 3.3(a) as evidence shows a representative snapshot of the same taken from the PIGLET trajectory. We see that the typical N-H and N$\cdots$H bond lengths are 1.08 and 2.01 Å respectively. These values are more or less the same as those found in other organic molecules solvated in water [106]. When the protons are treated classically (BOMD simulations), we observe there is zero occurrences of υ_1/υ_2 of being negative, i.e. there is no proton transfer to (from) the pyridine N (pyrrole N) from (to) the solvent (Figure 3.2). Upon inclusion of NQE (PIGLET simulations) we observe the fluctuations of the quantum protons of both the solvent molecules and ellipticine increases enormously, which indicates more labile protons and results in a small yet significant fraction of occurrences (about 1 in 3×10^4 for υ_1 and 1 in 1.5×10^4 for υ_2) where the H atom of solvent and solute is close to the pyridine N and the solvent water molecule nearest to the pyrrole N respectively. This physically points to the situation where the proton on the solvent molecule (solute molecule) delocalize and transiently protonates (deprotonates) the ellipticine molecule.

Figure 3.3 (b) and (c) show two representative snapshots, for υ_1 and υ_2 respectively. In the snapshot for υ_1, we see that the O-H bond of the water molecule is increased by

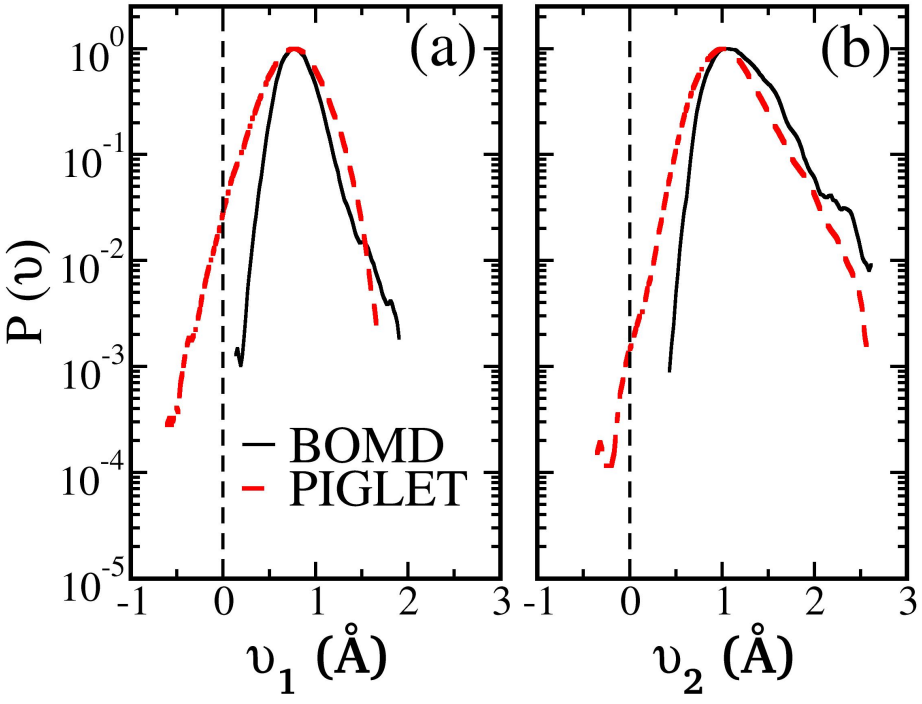

FIGURE 3.2: Probability distribution function of the proton transfer coordinates: (a) for proton acceptance coordinate (υ_1) and (b) for proton donation coordinate (υ_2) in water. The black solid line and the red dashed lines represent the PDFs obtained from BOMD and PIGLET simulations respectively.

0.60 Å from the conventional O-H bond length 1.05 Å, while the pyridine N$\cdots$H bond decreases by 1.02 Å (Figure 3.3(b)) from the usually observed 2.01 Å. Likewise for the case of υ_2, while the pyrrole N-H bond increased by 1.42 Å (as opposed to the typical value of 1.05 Å), the distance between the O of the closest water molecule and the H of the pyrrole N reduces to 1.07 Å (Figure 3.3(c)), which is similar to the typical O-H bond length of 1.05 Å in water. A zero value for $\upsilon_1, \upsilon_2 = 0$ υ_1 and υ_2 implies that the H atom is shared between the solvent molecule and ellipticine. The PDF suggests that pyridine N will be protonated in 1 in 10^2 configurations ($\upsilon_1 = 0$). However, for deprotonation of the pyrrole N, there will be 1 in 10^3 ($\upsilon_2 = 0$). This indicates that protonating the pyridine N is simpler compared to deprotonating the pyrrole N.

Amongst the many hypotheses used to rationalize the fluorescence spectra of ellipticine in different solvents, there is one where it is believed that there is an intramolecular proton transfer mediated by the solvent [76]. As mentioned in the Introduction, Banerjee *et al.* proposed that this proton transfer happens through the formation of cyclic species involving ellipticine and the solvent molecules. There is also a debate as to whether such a transfer happens in the ground state or in the excited state. On the time scales of the

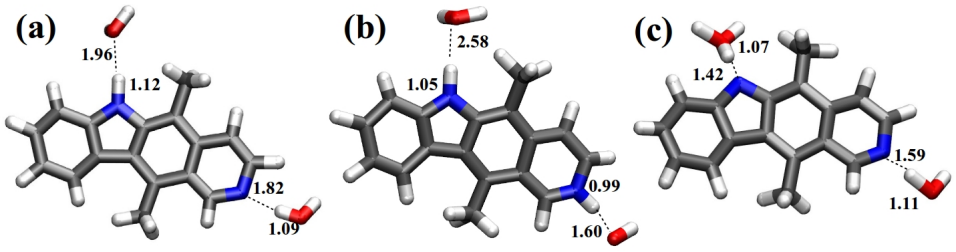

FIGURE 3.3: Representative snapshots from PIGLET simulations showing the position of the water molecules near pyrrole and pyridine N when (a) both υ_1 and υ_2 are positive (b) when only $\upsilon_1 < 0$ and (c) when only $\upsilon_2 < 0$.

current simulations, we do not observe any successful tautomerization events. If tautomerization was actually occurring as envisaged by previous studies, it could involve a fast proton transfer from ellipticine to water and vice versa, and would perhaps manifest itself in some correlation existing between the υ_1 and υ_2 proton transfer coordinates. Furthermore, it is also interesting to see how this could change with and without NQEs.

To check whether there are such correlations, we examined that the joint probability distribution ($\mathrm{P}(\upsilon_1, \upsilon_2)$) of the proton transfer coordinates (Please refer to Section A.2.0.2 in Appendix A for the definition of joint probability distribution). Figure 3.4 (a) and (b) show the $P(\upsilon_1, \upsilon_2)$ obtained from BOMD and PIGLET simulations respectively. The joint probability distribution obtained from the BOMD simulations (Figure 3.4(a)) show $\mathrm{P}(\upsilon_1, \upsilon_2)$ is zero both in the third quadrant and at the origin. In contrast, although the $\mathrm{P}(\upsilon_1, \upsilon_2)$ obtained from the PIGLET simulations (Figure 3.4(b)) is zero in the third quadrant, it is non-zero at the origin. $\mathrm{P}(\upsilon_1, \upsilon_2) = 0$ when both $\upsilon_1, \upsilon_2 < 0$ suggests that when there is a transient protonation event occurring at the pyridine N, the H already present at the pyrrole N remains attached to it. Similarly, during a transient deprotonation event at the pyrrole N, there is no protonation at pyridine. We also note that $\mathrm{P}(\upsilon_1, \upsilon_2)$ has a non-zero value when $\upsilon_1, \upsilon_2 = 0$ suggesting that there is a small but finite probability of proton sharing between the ellipticine and the water molecules simultaneously. However, the largely symmetric shape of $\mathrm{P}(\upsilon_1, \upsilon_2)$ suggests that these proton sharing events are most probably uncorrelated. Our results show that, for the present size of the simulation box and the length of the trajectories, even though we observe transient protonation and deprotonation in the ground state due to quantum fluctuations of the solvent and the solute protons, ellipticine tautomers are never formed.

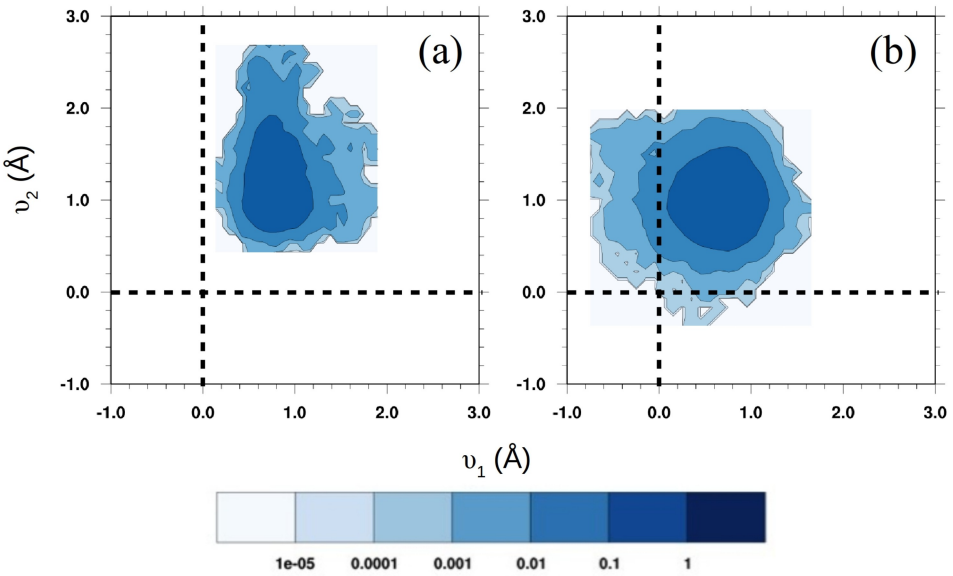

FIGURE 3.4: Contour plots of joint probability distribution function of the proton transfer coordinates υ_1 and υ_2 of water obtained from (a) BOMD and from (b) PIGLET simulations.

3.3.1.1 HB parameters

Recent studies by McKenzie *et al.* [88] and Li *et al.* [87] proved that H bonds strengths are reflected in the donor acceptor distances, donor-H-acceptor bond angles and the donor-H covalent bond length and that NQE studies usually ends up in longer (shorter) H-bonds for weak(strong)-H bonded systems. In order to determine the strength of the N_6-$H_6\cdots O_{w2}$ (pyrrole-H bond) and the O_{w1}-$H_{w1}\cdots N_2$ (pyridine-H bond) and the influence of NQE on them, we have plotted in Figure 3.5 the PDFs of the acceptor donor distances ($d_{N_6O_{w2}}$ for pyrrole-H bond and $d_{O_{w1}N_2}$ for pyridine-H bond), the covalent donor-H bond lengths and the donor-H-acceptor bond angles extracted from the BOMD and PIGLET trajectories. We note that unlike the systems considered in Ref.[87] and [88] where the donor and the acceptor have the same proton affinities, in the present system the proton affinities of the donors and acceptors are different. Earlier studies of proton affinities of N and O containing compounds showed that N has a larger proton affinity than O [107]. The average N-O bond distance from BOMD trajectories for the pyridine N is about 2.80 Å (Figure 3.5(a)) while that for the pyrrole N is 3.10 Å (Figure 3.5(d)) suggesting that the pyridine H bond is stronger than the pyrrole H bond. The inclusion of NQE using PIGLET simulations we find that the intermolecular distances decrease for both the cases. While for the former NQE reduces the average N-O distance by about 0.06 Å, for

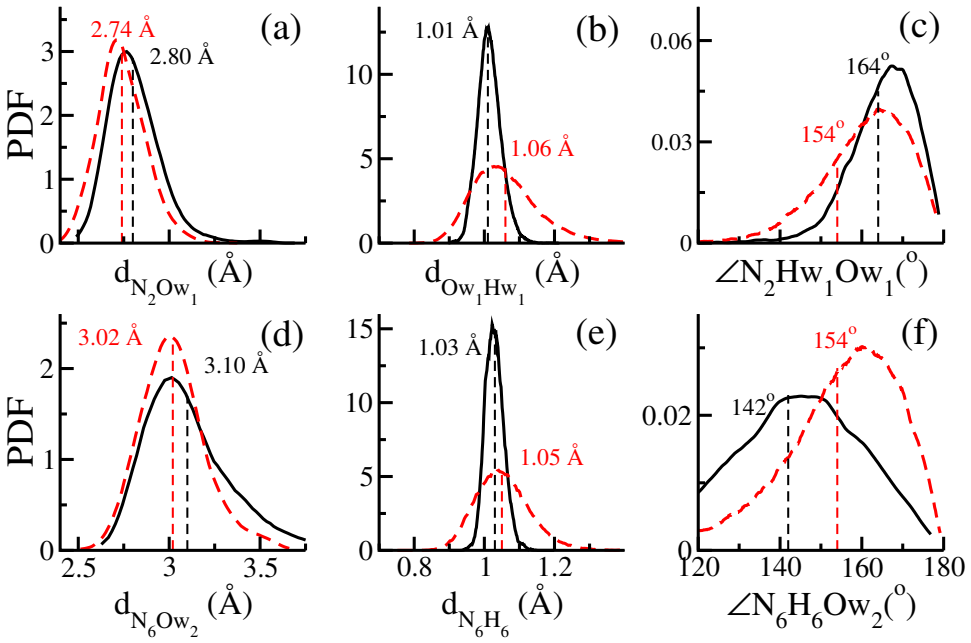

FIGURE 3.5: Probability distribution functions of the donor-acceptor distances ((a) and (d)), the donor-hydrogen covalent bond lengths (b), acceptor-hydrogen covalent bond lengths (e), and the donor-hydrogen-acceptor bond angle ((c) and (f)) obtained from BOMD (solid black lines) and PIGLET (dashed red lines) trajectories. The figures in the top panel ((a)-(c)) are for the strong pyridine H-bond while those at the bottom panel are for the weak pyrrole H-bonds. The average values of the above quantities for the BOMD and PIGLET trajectories are shown in black and red dashed lines, respectively.

the latter the N-O distance is reduced by 0.08 Å. Though the difference in the magnitude of reduction of the N-O distance due to NQE is small for the two types of H-bonds, in contrast to what has been observed for donors with same proton affinity, we find that in our case (donor and acceptors with different proton affinities) the NQE strengthens the relatively weaker H bond more than that of the stronger one. In accordance to the changes in the donor-acceptor distances, the donor-H covalent bonds become longer in the quantum simulations compared to the classical (Figure 3.5 (b) and (e)). Moreover for the stronger pyridine-H bond the elongation of the above mentioned covalent bond by the NQE (0.05 Å) is more pronounced compared to that of the weaker pyrrole-H bond (0.02 Å). The strengthening of the weak H bond due to NQEs is further reflected in the angle distribution (Figure 3.5(f)) where including the NQEs makes the hydrogen bond more linear. On the other hand, for the stronger hydrogen bond, its angular flexibility does not change significantly (Figure 3.5(c)).

3.3.1.2 Quantum effects on covalent bond

In addition to its effects on the protons of water and ellipticine, we find that the quantum nature of the nuclei also affects the heavy nuclei (namely C and N) in the molecule. Comparing the PDFs of the different C-C i.e, single and double bond lengths and C-N bond lengths of the ellipticine molecule obtained from the PIGLET and BOMD trajectories (Figure 3.6) we find that (a) there is significant broadening of the PDF, originating from the fluctuations induced by the quantum nature of the nuclei and (b) there is a slight increase in the average bond lengths. For most of the bonds, including the strong CN and C=C bonds, the full-width half maxima of the PDF almost doubles on the inclusion of NQE. This suggests that NQE not only affect the light protons but it is also important even for the heavier nuclei. The PDFs for the other bond lengths, average bond length values and the spread in the bond lengths are given in Table A.1 and Figure A.6 (Appendix A). We note that similar effects of NQE on the heavy nuclei have also been observed in inorganic systems like graphene [108], carbon tunneling in the rearrangement of carbene to cyclopentene [14], and complex biomolecules [79].

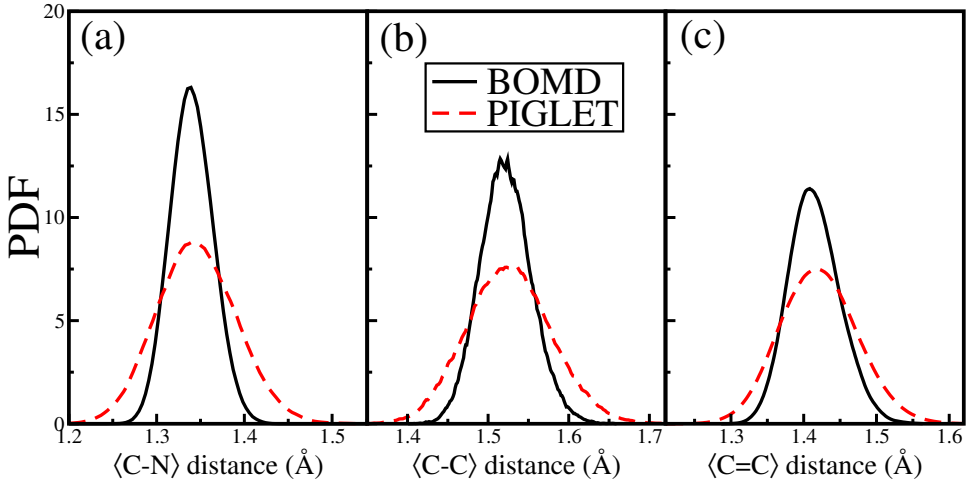

FIGURE 3.6: Probability distribution function of (a) $\langle C-N\rangle$ (b) $\langle C-C\rangle$ and (c) $\langle C=C\rangle$ bond lengths. The black solid line and red dashed lines represent the PDFs of the bond length obtained from BOMD and PIGLET simulations respectively.

3.3.2 Electronic absorption spectra of ellipticine in water

After investigating the effects of the quantum nature of the nuclei on the structure of the solute (ellipticine) and the solvent (water), in this section, we will now shed light on the effect of the NQE affect the electronic properties ellipticine in water.

3.3.3 Effect of quantum nuclei and solvent:

Figure 3.7 shows that the comparison of the experimental absorption spectra of ellipticine in water with that of the computed time-averaged spectra derived using snapshots from the trajectories obtained from PIGLET and BOMD simulations. We find good agreement between the computed spectra where NQE is included and the experimental spectra over the entire energy range considered in this study. Not only the peak positions are predicted reasonably accurately but also the overall shape and broadening of the peaks are nicely reproduced. The experimental spectrum (solid black line in Figure 3.7) displays two low-intensity broad peaks at (A) 420 nm and (B) 353 nm and dominant peak at (C) 300 nm. The latter is characterized by an asymmetric broadening. The computed PIGLET spectrum has two broad peaks at about 411.1 nm and 358.0 nm corresponding to peaks A and B respectively. The third dominant peak (corresponding to peak C in the experimental spectra) is at about 307.5 nm. We note that though the position of the peaks are sensitive to the type of exchange-correlation functionals used, the overall shape of the spectra is relatively independent of the choice of functionals. A detailed discussion on the effect of the functionals on the absorption spectra can be found in Appendix A. By inspecting the absorption spectra of the individual snapshots we find that peak A is primarily due to transitions from HOMO $\longrightarrow$ LUMO of the molecule, though we find a very small weight on the water molecule. Peak B and C arises primarily from excitation of electrons from HOMO $\longrightarrow$ LUMO+1, HOMO-1 $\longrightarrow$ LUMO. For certain snapshots there are also transitions with relatively less contributions from HOMO $\longrightarrow$ LUMO+3, HOMO $\longrightarrow$ LUMO+2 and HOMO-2 $\longrightarrow$ LUMO.

In order to understand the role of NQE, we have also plotted the absorption spectrum computed using the snapshots collected from our BOMD runs. A comparison of the two spectra shows that NQE results in dramatic changes in the computed spectra in the following ways: (a) an overall red shift of the spectra and (b) significant broadening of the peaks. If we compare the positions of the peaks A, B, and C, these are red shifted by 3.3, 11.3 and 8.7 nm respectively due to the incorporation of the NQE. To understand the origin of these shifts we have plotted the PDFs of the energy differences between LUMO and HOMO, LUMO+1 and HOMO, and LUMO and HOMO-1, for the different snapshots obtained from BOMD and PIGLET simulations. We note that the main contributions to the peaks in the absorption spectra results due to transitions between

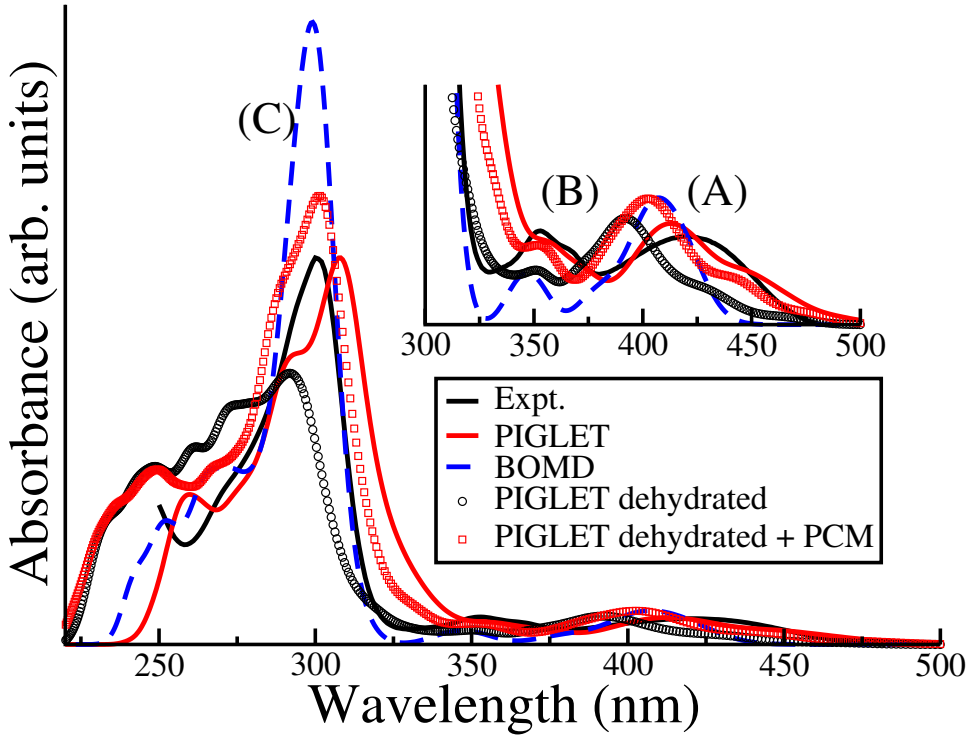

FIGURE 3.7: Comparison of the experimental absorption spectra [5] with the computed time averaged absorption spectra. The solid black line indicates the experimental spectra, solid red line denotes the computed spectra from PIGLET simulations, the dashed blue line indicates the computed spectrum from BOMD simulations, black open circles denote the computed absorption spectra of the dehydrated ellipticine molecule (from PIGLET) and the open red squares show the computed absorption spectrum of the dehydrated molecule with an implicit PCM model (from PIGLET). The inset shows that the zoomed in the region showing the two low-intensity peaks A and B.

these states. These distributions are shown in Figure 3.8. Like other properties, we find that the snapshots obtained from PIGLET simulations show a broader distribution of the energy eigenvalues differences compared to those obtained from the BOMD simulation. Furthermore, there is also an overall redshift of the energy differences for the snapshots from PIGLET, particularly for those between the LUMO+1 and HOMO and LUMO and HOMO-1. We note that these are the states involved in the transitions that give rise to peaks B and C. This explains a larger redshift observed for peaks B and C in the spectra on the inclusion of NQEs.

In order to filter out the effect of the solvent and NQEs, we have also plotted the time-averaged absorption spectra of the dehydrated molecule and that of the dehydrated molecule with PCM model. We find that the spectra of the dehydrated molecule is significantly blue-shifted with respect to the ones obtained using the PCM model and the

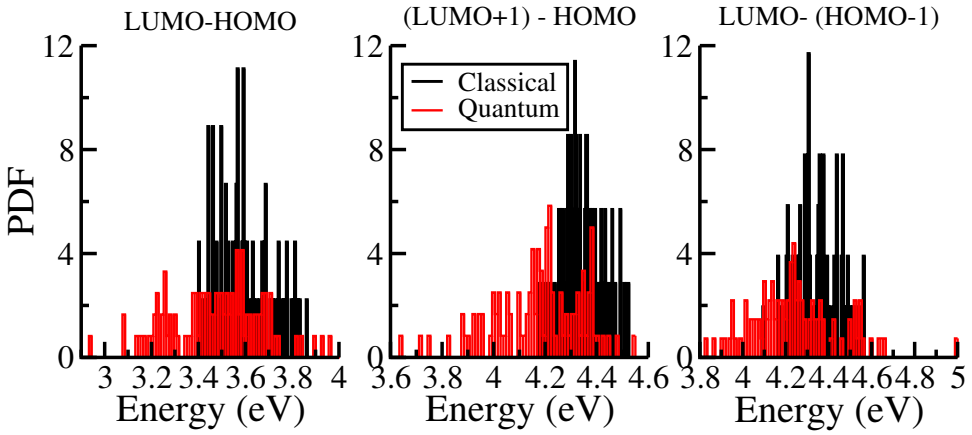

FIGURE 3.8: Probability distribution of energy eigenvalue differences of the different snapshots obtained from BOMD (black) and PIGLET (red) simulations.

explicit water molecules. This corresponds to the bathochromic effect on the spectra induced by the solvent. Furthermore, peak B is absent in the spectra of the dehydrated one. One also observe the hyperchromicity (enhancement of absorbance) in the presence of the solvent. On including the solvents effects through the polarizable continuum model, we see that the overall spectra shifts towards the longer wavelength side. However, to reproduce the broad features of the experimental spectrum, one needs to explicitly include water molecules in the calculation of the absorption spectra. This can be understood if one looks into the arrangement of the water molecules around the ellipticine and the wavefunctions corresponding to the states involved in the transitions. Water molecules interact with ellipticine either through the OH—π interactions or through the hydrogen bond. Plotting the spatial distribution of the frontier orbitals of the solvated ellipticine molecule (HOMO-1, HOMO, LUMO, LUMO-1) we find that in most of the snapshots there is a significant weight of these states on the water molecules. Figure 3.9 shows that these wave functions for a representative snapshot which show that these include significant contributions coming from water molecules hydrogen bonding with ellipticine. Hence a continuum PCM model cannot give a very accurate estimation of the oscillator strengths which depends on the expectation value of the transition dipole moment operator.

3.4 Conclusions

In conclusion, we have studied the nuclear quantum effects on the structure, dynamics, and spectroscopic properties such as optical properties of normal ellipticine in water

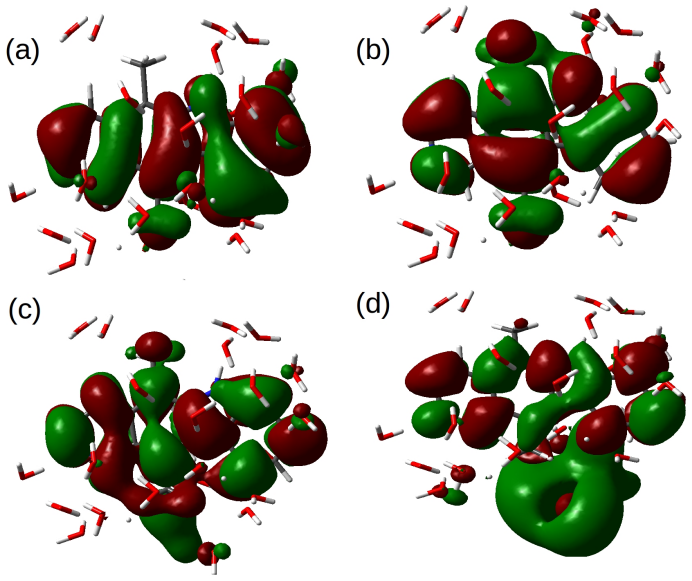

FIGURE 3.9: Isosurfaces of HOMO-1 (a) HOMO (b) LUMO (c) and LUMO+1(d) of a typical snapshot from PIGLET simulations. The green and red surfaces indicate the negative and positive part of the wave function.

using path integral molecular dynamics along with a recently proposed colored noise thermostat based on the generalized Langevin equation. We find that NQE increases the fluctuations, not only in the light protons of the hydrogen-bonded network of water and ellipticine molecule but also affects different ellipticine bond lengths formed from the relatively heavier C and N nuclei. For the total duration of our simulations, we find that there are small but significant instances of proton transfer to and from the solvent resulting in the protonated and deprotonated form of ellipticine. Our studies suggest that protonation or tautomerization of ellipticine in water is kinetically unfavorable and most probably occurs in the excited state. In contrast to the cases where the H bond donors and acceptors have same proton affinity, we find that for our case where the proton affinities of the donor and acceptor are different the NQE strengthens both the weak and the strong H bonds with the former being significantly more strengthened than the latter.

Further, the quantum nuclear fluctuations make the atoms quite labile, thereby influencing the electronic structure of the ellipticine-water complexes. This results in a significant redshift and broadening of the spectra. Our results show that in order to reproduce the experimental absorption spectra or to predict absorption spectra of solvated molecules, it is important to include nuclear quantum effects in the simulations. Both experimentally and computationally the role of nuclear quantum effects in these

systems can be further elucidated by studying the change in the absorption spectra induced by isotopic substitution of (a) the proton bound to the pyrrole N of ellipticine and (b) using D_2O as a solvent instead of water. While the former will elucidate the role NQE on the absorption spectra due to the weak pyrrole H bond, the latter will throw light on the effect of NQE on the absorption spectra due to the strong H bond at the pyridine N. Since our study shows that NQE strengthens both the H bond, we expect a blue shift of the adsorption spectra along with a reduction in the broadening of the peaks. Considering the fact that the transfer, release, and uptake of drugs are typically monitored by monitoring the changes in their optical properties and our studies show that NQE affects both qualitatively and quantitatively the drug's optical properties, we believe that our results should motivate future experimental and theoretical studies to correctly unravel the role of NQE on the microscopic mechanisms responsible for the optical response of drug molecules in biologically important hydrogen-bonded systems.

Chapter 4

Role of Nuclear Quantum Effects on solute-solvent and solvent-solvent Hydrogen bonding: The case of Ellipticine in protic solvents

4.1 Introduction

In the previous chapter, we have shown how NQEs affect the structural and electronic properties of ellipticine in water. Ellipticine has a pyrrole and a pyridine N. While the former has a H attached to it and acts as a proton donor, the latter acts as a proton acceptor. The attractive interaction of ellipticine is primarily due to the formation of H-bonds with the solvent through these two N atoms. Since the proton affinities of these N atoms are different from that of O in water, the solute (ellipticine)-solvent (water) H-bond belongs to the class of asymmetric H bonds. In contrast to H bonds involving symmetric donor-acceptor pairs [109, 110] we have found that for this specific case, both the weak and strong H bonds are strengthened when NQEs are considered in the simulations. However, it is not clear whether this effect is true for all other solvents.

TABLE 4.1: Properties of protic solvents. PA is the proton affinity, α is the hydrogen bond donating capacity, β is the hydrogen bond accepting capacity, π is the polarizability, ϵ is the dielectric constant, r is the refractive index, ρ is the dipole moment [7].

Solvent	PA (kJ/mol)	α	β	π Cm^2V^{-1}	ϵ	r	ρ Debye
H_2O	697	1.17	0.47	1.09	80.4	1.33	1.85
Met	761	0.98	0.66	0.60	32.7	1.33	1.69
EGL	816	0.90	0.52	0.92	37.0	1.43	2.36

In an effort to elucidate the generality of the conclusions made in the previous chapter, in this chapter we extend this study to two more protic solvents, namely, methanol and ethylene glycol. A comparison of the properties of water, methanol and ethylene glycol is given in Table 4.1. We find that as we move from water to methanol to ethylene glycol, the H-bond donor capacity of the solvent reduces suggesting that for the H-bonds will be weaker (stronger) where the solvent molecule acts as a donor (acceptor). Moreover, in the previous chapter, we had focussed primarily on the importance of NQEs on solute-solvent H-bond. In this chapter, in addition to the above-mentioned H-bonds, we will also discuss how the NQEs and the solute-solvent (asymmetric) H-bonds affect the solvent-solvent (symmetric) H bonds.

The rest of the chapter is divided as follows. In Section 4.2 we describe the details of the different simulation techniques used in this work. Section 4.3.1 contains the results of the change in the nature of H-bond between ellipticine and solvent molecules. Further, we have also discussed how NQEs affect these H-bonds. In Section 4.3.2 we have discussed how the H-bonds between the solvent molecules are affected due to ellipticine solvent H-bonding. In Section 4.3.3 we elucidate the role of NQEs in the absorption spectra of ellipticine in different solvents. Finally, we summarize and conclude in Section 4.4.

4.2 Computational details

4.2.1 Classical molecular dynamics simulations

We have carried out classical MD simulations using the GROMACS-4.5.5 software (with double precision). The protic solvent molecules are explicitly represented and described by the amber force fields [89, 111–113]. The MD simulations were based on the general

amber force field (GAFF) [90] parameters. Ellipticine was optimized followed by Merz-Kolmann charge calculation [91] using Hartree-Fock theory with 6-31G(d) basis set using Gaussian 09 [92]. Antechamber module of AMBERTools [93] was used for a restrained electrostatic potential charge (RESP) [94] calculation and generation of the general amber force field (GAFF) [90]. Finally, the coordinates and topology were converted to GROMACS format using amb2gmx.pl program [95].

TABLE 4.2: Force field parameters of the protic solvents with equilibrated cubic box length.

Solvent	No. of atoms in the box including EP molecule	Cubic box length length (Å)	Force field
Water	2979	31.55	TIP3P [89]
Methanol	2409	29.81	OPLS-AA [112, 113]
Ethylene glycol	3753	32.08	AMBER [111]

Ellipticine (EP) was placed in a cubic box and solvated with protic solvents. Table 4.2 shows the information of the equilibrated box of the EP in protic solvents. For the NVT simulations, a constant temperature of 300 K was maintained by coupling the system to a thermal bath with the Andersen algorithm and a time constant of 1 ps, whereas for the NPT simulations a constant pressure of 1 bar was maintained using the Berendsen barostat [96] with isotropic scaling and a time constant of 2 ps. All Lennard-Jones interactions were cut off at 10 Å and a particle mesh Ewald correction to the long-range electrostatic contribution was applied. The integration step was set to 2 fs and the X-H stretching modes were frozen with the LINear Constraint Solver (LINCS) algorithm [97].

The simulation protocol for the classical simulations was as follows: after 2000 steps of energy minimization, we performed simulated annealing (annealing time of 100 ps) under NPT conditions to heat the system to 300 K. This was followed by equilibration at 300 K for 100 ps in the NPT ensemble. Starting from the equilibrated system, MD trajectories were recorded for 10 ns in the NVT ensemble. The data sampled every 1 ps during the last 7 ns were used for analysis.

4.2.2 Born-Oppenheimer molecular dynamics (BOMD) and PIGLET simulations

In the BOMD simulations, the nuclei are treated classically, while the electrons are treated at the level of density functional theory. Performing these simulations for the enormously large system mentioned in the previous section is prohibitively expensive. Hence we extracted a configuration from the end of the classical MD runs and truncated the solvent molecules to its second solvation shell based on where the radial distribution function plot plateaus. The simulated system consists of one EP molecule surrounded by 62 (70) methanol (ethylene glycol) molecules placed in a cubic box of side 16.3 (18.96) Å.

These calculations were performed using the Quickstep module of the CP2K package [98]. The electronic exchange and correlation energies were described using the Becke-Lee-Yang-Parr (BLYP) exchange-correlation functional [40]. The core electrons have been described using Goedecker-Teter-Hutter (GTH) pseudopotentials [99]. Wave functions were expanded in the Gaussian polarized triple-zeta split-valence (TZVP) basis set, whereas the electronic density was represented using an auxiliary plane wave basis, with a kinetic energy cutoff of 300 Rydberg. A convergence criteria of 5×10^{-7} a.u. was used for the optimization of the wavefunction. The D3 Grimme dispersion corrections for the van der Waals interactions were used. [100] The simulations were performed within the NVT ensemble at 300 K temperature using the canonical-sampling velocity-rescaling thermostat. [101] The simulations were run for 55 ps. Integrations were performed with 0.5 fs time step. The system equilibrated within the first 5 ps of the run. Snapshots were selected from the remaining 50 ps trajectory for further analysis.

Starting from a snapshot chosen randomly from the equilibrated BOMD trajectory, we start the PIGLET simulations with a generalized Langevin equation based colored-noise thermostat to incorporate quantum effects [15, 50]. Based on literature reports[17, 84], we have used six beads for the path integral simulations. The total simulation of methanol (ethylene glycol) solvent was run for 10 (7) ps for with a time step of 0.5 fs. The first 2 ps of the run was treated as equilibration and snapshots from the remaining part of the trajectory were used for further analysis. To achieve this we have used a recently released code i-PI. [17] In the rest of the chapter, we will refer to the classical simulations as BOMD and the PIGLET simulations as PIGLET.

4.2.3 Excited State Calculations

To understand the effect of NQE on the optical properties of EP in solvents, we have computed the time-averaged absorption spectra using snapshots from both the BOMD and the PIGLET trajectories. In order to compute the absorption spectra from our BOMD simulations, we have randomly selected 120 snapshots from the BOMD trajectory, computed the absorption spectra of each using time-dependent density functional theory (TDDFT) and the final spectrum is the average of the spectra of these 120 snapshots. A convergence test of the absorption spectra as a function of the number of snapshots showed that one can obtain well-converged spectra with 120 snapshots. The absorption spectra from the PIGLET simulations were constructed using a formalism previously developed by Marx and co-workers[83]. 20 frames selected randomly from the PIGLET run were used to compute the spectra. For each frame, all 6 beads were used.

Due to the strong interaction between the solvent and solute molecules, the absorption spectra are sensitive to whether the solvent molecule is explicitly included in the calculations. Hence to compute the absorption spectra for each snapshot, we cut out geometries from the ground state molecular dynamics trajectory ("finite cluster" model) and perform TDDFT calculations. However, performing TDDFT calculations with ellipticine and entire solvated box to obtain a spectrum for an energy window of about 2.2-6 eV (25 empty electronic states, includes both bright and dark states) is very expensive. Hence there is a need to strike a balance between computational cost and accuracy. A convergence test of the absorption spectra of an individual snapshot as a function of number of methanol (ethylene glycol) molecules showed that at least 20 (13) explicit water molecules are necessary for accurately computing the spectra. Details regarding the choice of the number of solvent molecules and their effect on the spectra are given in Figure A.11, A.12, A.13 in section A.4 of Appendix A.

Since the computed absorption spectra are sensitive on the choice of the exchange-correlation functionals, to decide a suitable choice of functionals we have computed the transition energies for ellipticine molecule in the gas phase from TDDFT calculations with different hybrid functionals and compared them with more accurate equations of motion coupled-cluster-singles-doubles (EOMCCSD) based calculations. Figure 4.1

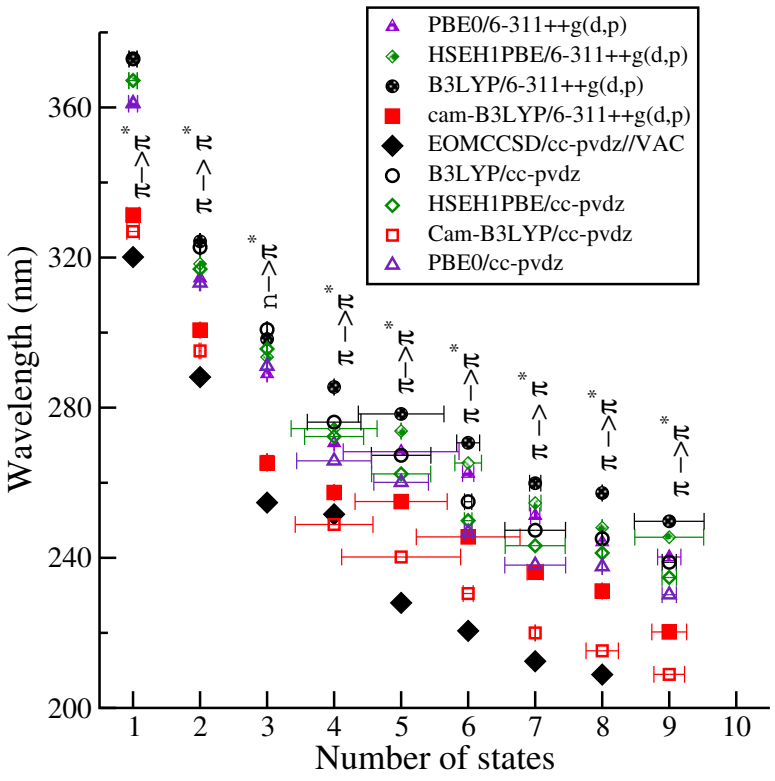

FIGURE 4.1: Comparison of excitation positions obtained from TDDFT calculations using hybrid functional with EOMCCSD calculations. The horizontal lines indicate the oscillator strength. These calculations are done in the gas phase.

shows the comparison of the TDDFT calculations with hybrid functional with EOM-CCSD calculations. We found that cam-B3LYP hybrid functional gives energies that are closest to those obtained with EOMCCSD calculations. Hence to compare absorption spectra of ellipticine across different solvents we have used results obtained from calculations performed with cam-B3LYP functional.

4.3 Results and Discussion

4.3.1 Effect of NQEs on ellipticine-solvent H-bond

In order to understand the effect of the quantum nature of the nuclei on the H-bonding between ellipticine and solvent molecules we have defined the proton acceptance and donation coordinates υ_1 and υ_2 respectively and monitored the same throughout our simulation trajectories. As mentioned in the previous chapter, a negative value of υ_1 and υ_2 implies the occurrence of proton transfer events. Figure 4.3 shows the probability distribution function (PDF) of the proton transfer coordinates (PTC) for the three

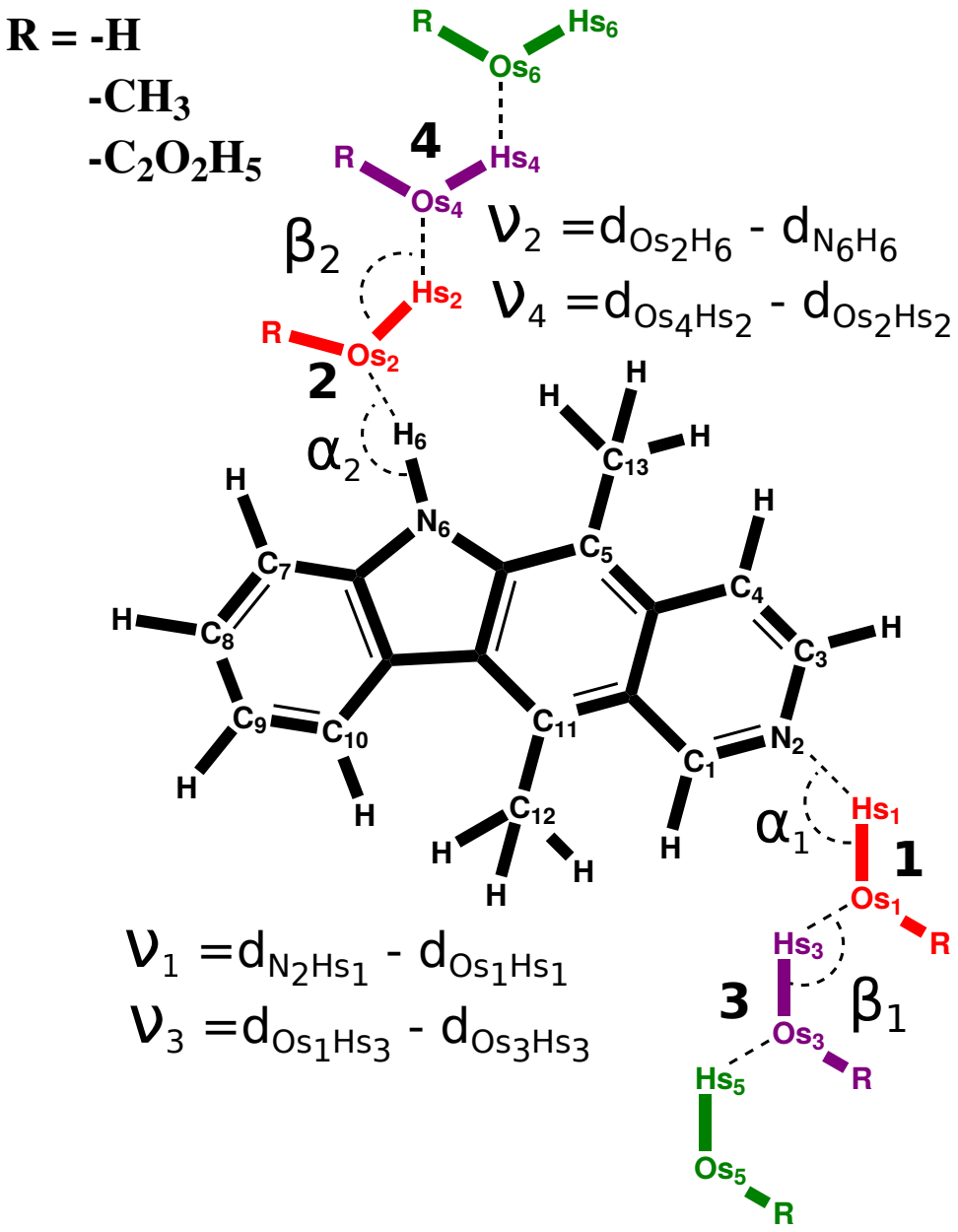

FIGURE 4.2: Schematic of ellipticine molecule in its normal form. Also shown are the proton acceptance (υ_1, υ_3) and donation (υ_2, υ_4) coordinates. α_1, β_1, α_2, and β_2 are HB angles at υ_1, υ_2, υ_3, and υ_4 respectively. d_{AD} in the figure denotes the distance between atoms A and D. Here, red colored labels denotes proton donating coordinates and blue colored labels denote proton accepting coordinates.

solvents. Those in the top panel of Figure 4.3 have been computed from the BOMD trajectories while those in the bottom panel are computed using the PIGLET trajectories. Similar to what we observed for water, we find that in the BOMD simulations where the nuclei are treated classically, not only there are no protonation and deprotonation events for both the proton transfer coordinates but also the protons remain strongly bound to the donor atoms through covalent bond ($\upsilon_{1,2}$ always greater than zero). In contrast, as

the NQE is turned on, we find that though most of the time there are no protonation/deprotonation events (the PDFs are peaked at positive values of υ_1 and υ_2), there are a few instances where one observes the occurrence of protonation/deprotonation events. We note that though these instances are small, they are not negligible. Moreover, we also find that there are a significantly large number of configurations where the protons are shared between the heavy atoms, $\upsilon_{1,2} = 0$. This is true for all the υ's in all the three solvents except for υ_2 in ethylene glycol. In ethylene glycol (EG) we do not observe any occurrence of deprotonation of the pyrrole (N) of ellipticine. This can be attributed to the steric repulsion that the bulky methyl group of EG face due to the presence of the -CH_3 group in ellipticine close to pyrrole N when EG tries to approach ellipticine. Hence our calculations show that the quantum nature exhibited by the light protons makes the H atoms more labile, thereby weakening the covalent donor-H bond. Moreover, as we move from water to methanol to ethylene glycol we find that the magnitude of the negative value of υ_1 decreases. This implies that the transferred proton from water to pyridine N is most strongly bound to the acceptor pyridine N for water and weakest for ethylene glycol. Additionally, we also find that the number of configurations where the proton is shared between pyridine N and the nearest solvent molecule also decreases from water to ethylene glycol. This shows that as we move from water to ethylene glycol the strength of the solute-solvent H bond weakens.

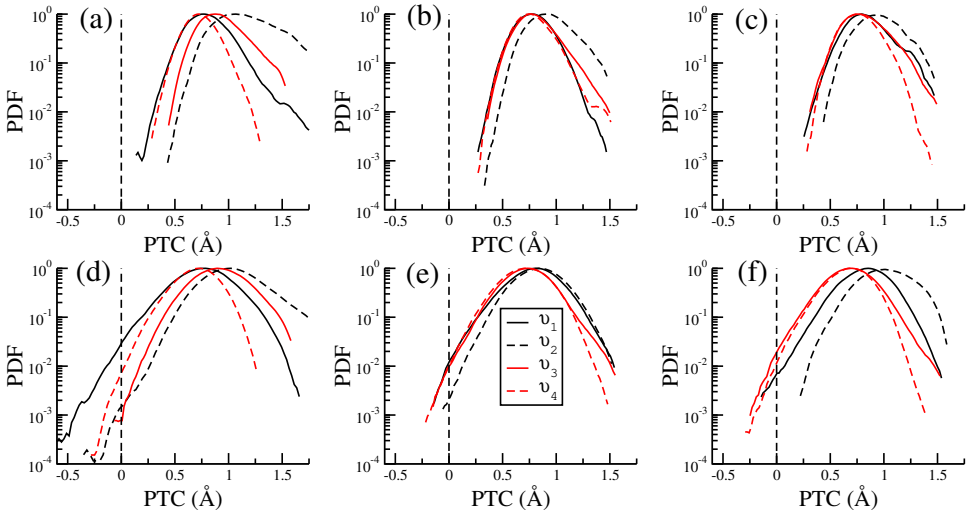

FIGURE 4.3: Probability distribution function of the different proton transfer coordinates (as described in Section 3.3.1 and 4.3.2) of ellipticine in water ((a) and (d)), in methanol ((b) and (e)), and in ethylene glycol ((c) and (d)). The PDFs in the top (bottom) panel are computed using data obtained from BOMD (PIGLET) simulations. For the definition of υ_{1-4}, the readers are referred to Figure 4.2.

TABLE 4.3: The values of the PDFs when υ_1 and υ_2 are zero.

Solvent	Water	Methanol	EGL
$\upsilon_1 = 0$	2.8×10^{-2}	1.2×10^{-2}	6.61×10^{-3}
$\upsilon_2 = 0$	1.5×10^{-3}	2.2×10^{-3}	No event

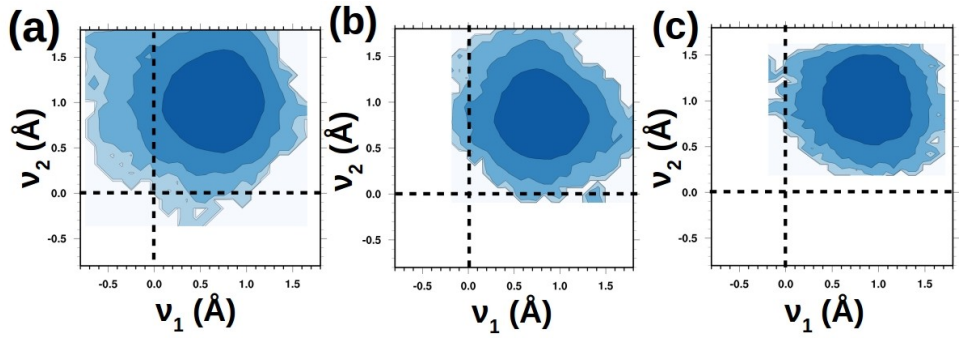

FIGURE 4.4: Contour plot of the joint probability distribution of the proton transfer coordinate υ_1 and υ_2 of a) water, b) methanol, and c) ethylene glycol obtained from PIGLET simulations

Similar to the case of water, ellipticine in methanol or ethylene glycol also shows dual fluorescence. The reason for the same has been attributed to either formation of protonated or tautomeric ellipticine in the solvents. Further, there is also a debate as to whether this forms in the ground or in the excited state. For the formation of tautomer, the pyridine N must be protonated while the pyrrole N must be in deprotonated. Hence for tautomeric configurations, both $\upsilon_{1,2}$ should be negative implying that there should be a correlation between υ_1 and υ_2. In order to determine whether there is any such correlation, we have plotted the joint PDF (JPDF) of υ_1 and υ_2. The contour plots of the same are shown in Figure 4.4. We find that similar to water, both for methanol and ethylene glycol the protonation and deprotonation events are not correlated. This tells us that while in the ground state it is possible to have a protonated form of ellipticine, however, it is unlikely that tautomers are also formed.

Now we proceed to study the effect of NQE′s on the H-bonds as a function of the solvent. Based on the distance between the donor (D) and acceptor (A), N and O respectively in our case, there are two types of H bonds between ellipticine and the solvent molecules. A weak H-bond between the pyrrole N and solvent and a relatively stronger one between pyridine N and solvent. An H-bond is typically characterized by the D-A distance, the covalent D-H bond length, and the D-H-A bond angle. For the pyridine N (pyrrole N) and solvent the donor is an O (N) atom while the acceptor is an N (O) atom. The

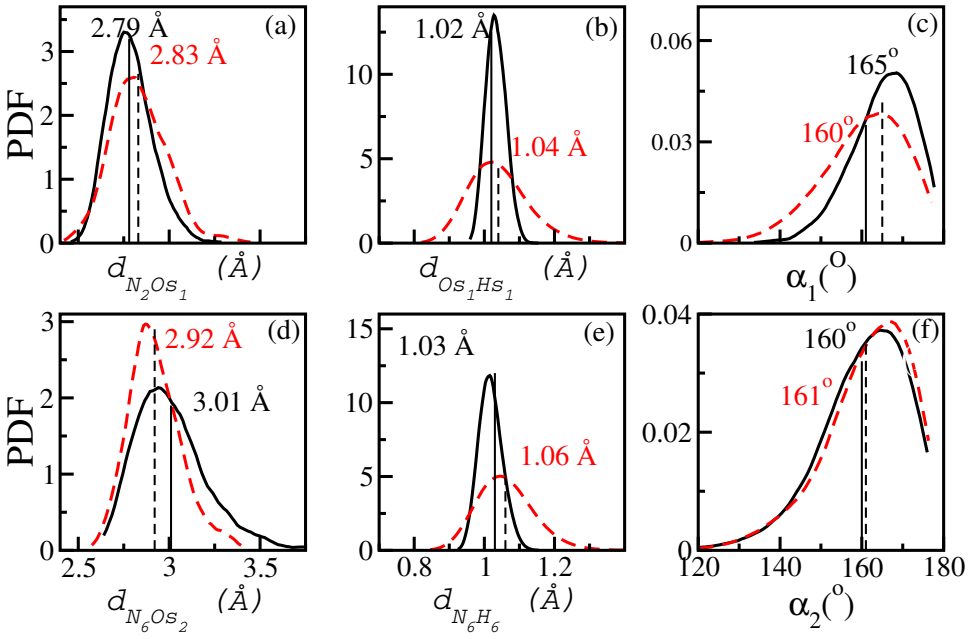

FIGURE 4.5: EP in methanol: Probability distribution functions of the donor-acceptor distances ((a) and (d)), the donor-hydrogen covalent bond lengths (b), acceptor-hydrogen covalent bond lengths (e), and the donor-hydrogen-acceptor bond angle ((c) and (f)) obtained from BOMD (solid black lines) and from PIGLET (dashed red lines) trajectories. The figures in the top panel ((a)-(c)) are for the strong H-bond while those at the bottom panel are for the weak H-bonds. The average values of the above quantities for the BOMD and PIGLET trajectories are shown in black and red dashed lines, respectively.

PDF plots of the heavy atom distances, the H-donor covalent bond, and the donor-H-acceptor bond angle for methanol and ethylene glycol are shown in Figure 4.5 and Figure 4.6 respectively. In contrast to what we have observed in water, we find that when the solvent is methanol, the NQEs weaken the strong H bond while it strengthens the weak one. The average N-O distance for the strong (weak) H-bond increase (decrease) from 2.79 Å (3.01 Å) to 2.83 Å (2.92 Å) on turning on the NQE′s in our simulations. (from PIGLET) (Figure 4.5). On the other hand for ethylene glycol, NQE weakens both the strong and weak H bonds (Figure 4.6). However, the effects are more dominant for the weak bond than the strong one. For example, the D-A distances for the strong H-bond obtained from our PIGLET simulations is 0.01 Å larger than that obtained from BOMD simulations. In contrast for the weak H-bond, the D-A distance is increased by about 0.15 Å. Such a large increase in the D-A distance is due to the dual effect, namely, the NQE and the steric repulsion faced by ethylene glycol when it approaches the pyrrole N of ellipticine. Further we find that the magnitude of the difference between the average donor-acceptor distances obtained from the BOMD and PIGLET for the strong H-bond, which is a measure of how strong the NQE′s are, decreases as we move from water to

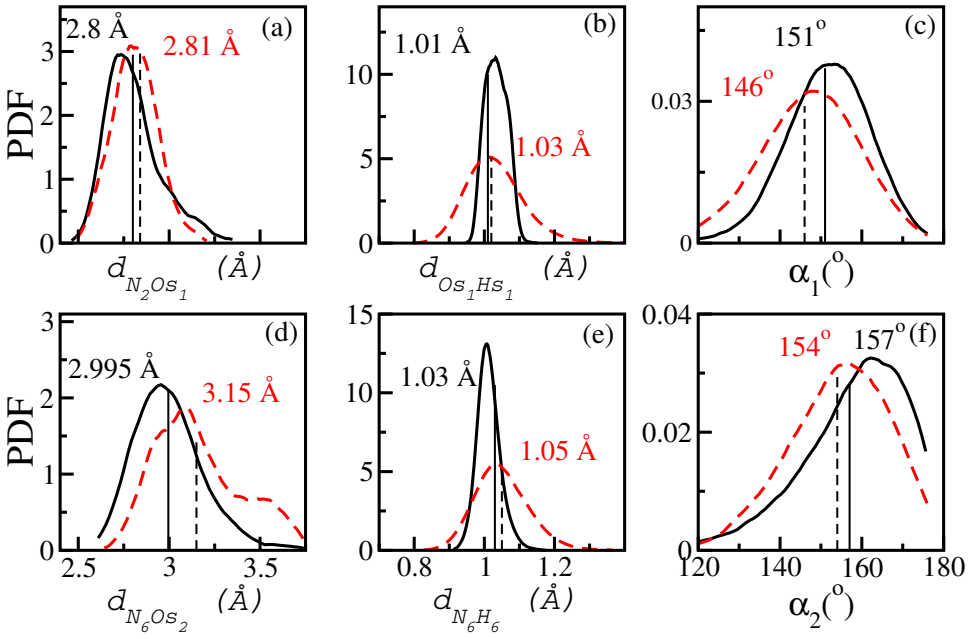

FIGURE 4.6: EP in ethylene glycol: Probability distribution functions of the donor-acceptor distances ((a) and (d)), the donor-hydrogen covalent bond lengths (b), acceptor-hydrogen covalent bond lengths (e), and the donor-hydrogen-acceptor bond angle ((c) and (f)) obtained from BOMD (solid black lines) and from PIGLET (dashed red lines) trajectories. The figures in the top panel ((a)-(c)) are for the strong pyridine H-bond while those at the bottom panel are for the weak H-bonds. The average values of the above quantities for the BOMD and PIGLET trajectories are shown in black and red dashed lines, respectively.

methanol to ethylene glycol. This implies that the importance of NQEs on the solute-solvent H-bond decreases as one goes from water to methanol to ethylene glycol.

To understand which property of the solvent correlates well with the decreasing importance of NQEs we looked into the variation of proton affinity (PA) and H bond donation ability (α) of the solvents. We note that these two are inversely related. We find that as one moves from water to methanol to ethylene glycol the PA increases while α decreases. It is expected that as the PA (α) of the solvent increases (decreases) it will act like a bad proton donor and hence will have a reduced propensity to form the H bond and for such cases the effect of NQEs decrease. For our system, for the case of the strong H bond, i.e., between pyridine N and solvent where the latter acts as a proton donor we find the importance of NQEs diminish.

4.3.2 Effect of NQE on H-bonding in explicit solvent environment

In this section, we elucidate how the H bond between two solvent molecules (one that is interacting with the solute and the second one that is closest to the previous one) are affected due to the H-bond between the solute and the solvent molecule. Further, we also discuss the role of NQEs for such H-bonds. To do so, in addition to υ_1 and υ_2, we have introduced two more proton transfer coordinates that will be useful to quantify the fluctuations in the H bonds within the solvent molecules. These are shown in Figure 4.2 where $\upsilon_3 = d_{Os_1Hs_1}$ - $d_{Os_3Hs_3}$, the subscript 1 denotes the solvent molecule that is forming a H-bond with the pyridine N and the subscript 3 denotes the solvent molecule that is closest to the solvent molecule 1 and forming H bond with it. A negative value of υ_3 denotes that a proton from solvent molecule 3 is transferred to solvent molecule 1. Analogous to υ_3 we have defined $\upsilon_4 = d_{Os_4Hs_4}$ - $d_{Os_2Hs_2}$. We note that υ_3 and υ_4 will provide information on the fluctuations in the H-bonding between the solvent molecules due to the fluctuations in the solvent-solute H bonding. In addition to υ_1 and υ_2, we also monitored υ_3 and υ_4 throughout the BOMD and PIGLET trajectories. Similar to υ_1, we find that for all the three solvents there are low but finite probabilities of a proton being transferred from solvent molecule 3 to solvent molecule 1 (interacts with ellipticine), which is corroborated by the fact that the PDF plots of υ_3 shows that there are low probabilities that υ_3 can have negative values. Additionally, we find that there is a significant fraction of configurations where the proton is shared between two solvent molecules. Moreover, the PDF plots for υ_3 and υ_4 are almost similar for methanol and ethylene glycol while they are significantly different for water.

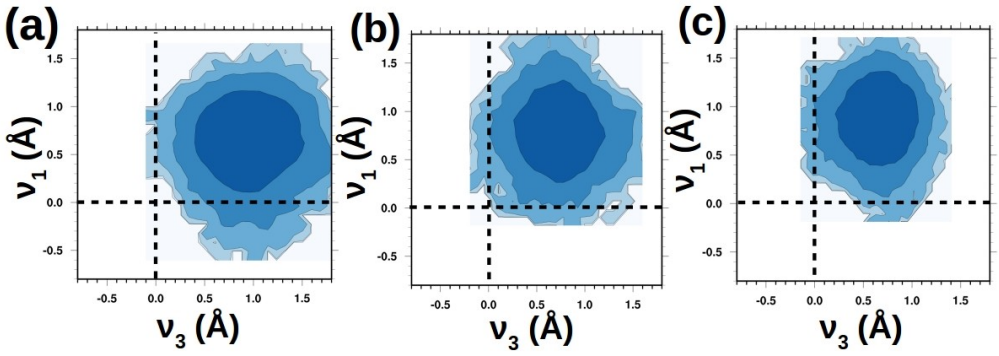

FIGURE 4.7: Contour plot of the joint probability distribution of the proton transfer coordinate υ_1 and υ_3 of a) water, b) methanol, and c) ethylene glycol obtained from PIGLET simulations

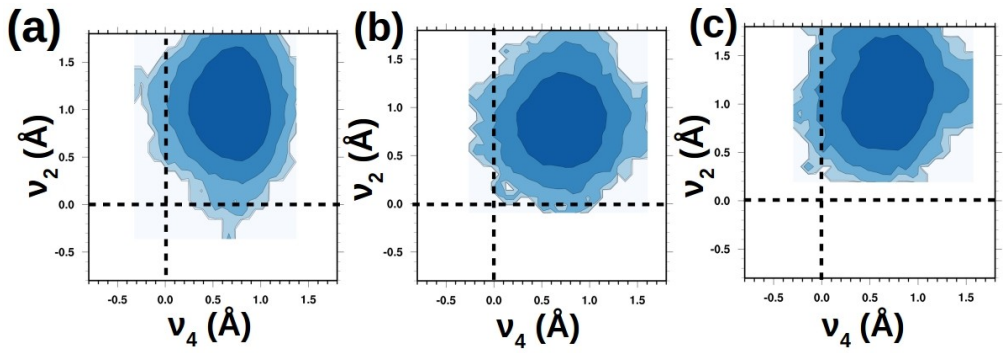

FIGURE 4.8: Contour plot of the joint probability distribution of the proton transfer coordinate υ_2 and υ_4 of a) water, b) methanol, and c) ethylene glycol obtained from PIGLET simulations

Figures 4.9, 4.10, 4.11 show some representative snapshots from our PIGLET simulations where $\upsilon_{3,4}$ are positive, zero and negative for water, methanol and ethylene glycol respectively. Figure 4.9(a) shows a representative snapshot of the ellipticine along with the water molecules that are used to define the proton transfer coordinates for the case where υ_3 and υ_4 are zero while Figure 4.9 (b) and (c) are representative snapshots where υ_3 and υ_4 are negative respectively. For $\upsilon_3 < 0$ we see that the water molecule (labeled as red in Figure 4.9 (b)) is converted to a hydronium ion (H_3O^+) with each of the -OH bond length being 1.07 Å. Moreover, the water molecule labeled as purple is converted to an OH^- ion. The hydrogen bond length between this H_3O^+ and OH^- ion is about 1.53 Å. In contrast, when $\upsilon_4 < 0$ we find that the H that is transferred from water molecule 2 (Figure 4.9 (c)) forms a relatively weaker bond with water molecule 4, to which the proton is transferred (1.33 Å). In contrast with water, for methanol and ethylene glycol we find that for both υ_3 and υ_4 the bond between the solvent molecule and the transferred proton is much weaker than a conventional -OH bond.

Additionally, we have also investigated if there is any occurrence of concerted proton transfer, analogous to Gröthus mechanism, i.e. when solvent molecule 1 accepts (donates) proton from (to) ellipticine it donates (accepts) another proton to (from) solvent molecule 2. To do so we have plotted the JPDF between υ_1 (υ_2) and υ_3 (υ_4). These are shown in Figure 4.7 and 4.8 (for classical analogous, See Figure Figure A.14 and Figure A.15). If the two events are correlated then we would expect non-zero probability when both υ_1 and υ_3 (or υ_2 and υ_4) are zero. However, for all the solvents, we find that the PDF to be zero in the third quadrant of the JPDF plots suggesting that these events are uncorrelated.

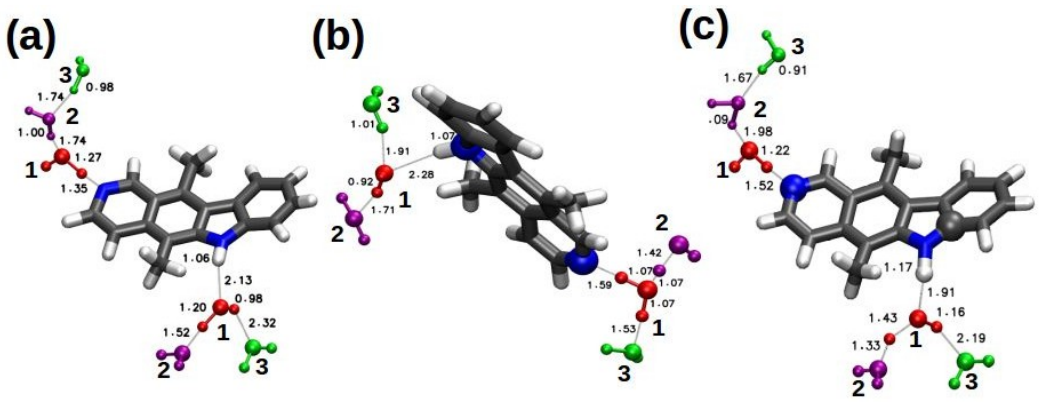

FIGURE 4.9: Representative snapshots for a) both υ_3 and υ_4 are positive, b) $\upsilon_3 < 0$, and c) $\upsilon_4 < 0$ for ellipticine in water. Red colored solvent is closest to ellipticine molecule and Purple (green) are the next closest water molecules. The molecule "1" is the first nearest H-bonded solvent molecule to the ellipticine. Further molecule "2" and "3" are next H-bonded solvents to the molecule "1". The bond lengths are given in Å.

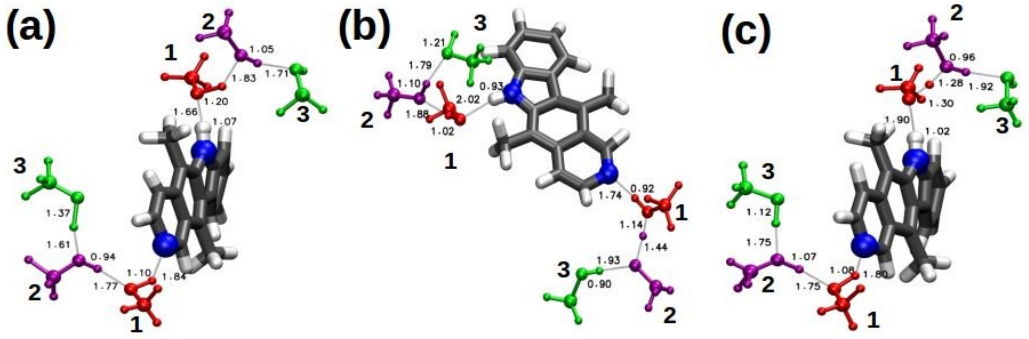

FIGURE 4.10: Representative snapshots for a) both υ_3 and υ_4 are positive, b) $\upsilon_3 < 0$, and c) $\upsilon_4 < 0$ for ellipticine in methanol. The red colored solvent is closest to ellipticine molecule and Purple (green) colored solvent is the next closest methanol molecules. The molecule "1" is the first nearest H-bonded solvent molecule to the ellipticine. Further molecule "2" and "3" are next H-bonded solvents to the molecule "1". The bond lengths are given in Å.

Now we proceed to understand how the strength of the H-bonds within the solvent molecules are affected due to the H bond between the solute and the solvent. If the solute-solvent H-bonds do not perturb the solvent H bonds, then the H bond formed between solvent molecules 1 and 3 and 2 and 4 should exhibit similar properties. As we had done in the previous section, we have plotted the PDF for the heavy atom distances, the O-H covalent bond distances and the ∠O-H-O bond angles for the solvent molecules near the two solute-solvent H bond. These are shown in Figure 4.12, 4.13, 4.14 for water, methanol and ethylene glycol respectively. For methanol, we find that for both the H bonds, the average D-A distances are similar and NQE slightly strengthens both the bonds (4.13). Similar behavior was also observed for ethylene glycol (4.14).

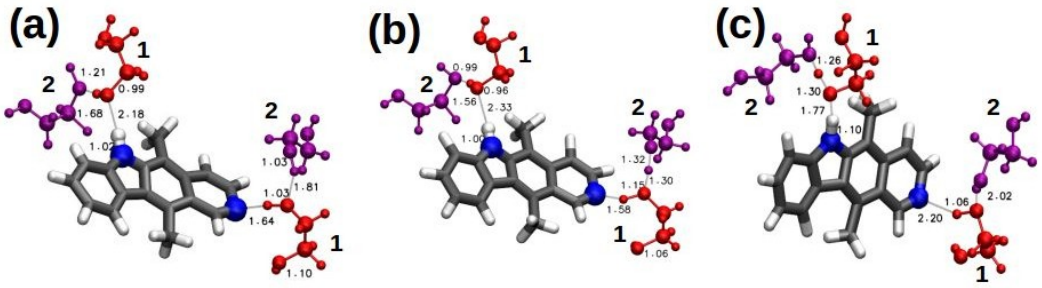

FIGURE 4.11: Representative snapshots for a) both υ_3 and υ_4 are positive, b) $\upsilon_3 < 0$, and c) $\upsilon_4 < 0$ for ellipticine in ethylene glycol. The red colored solvent is closest to ellipticine molecule and Purple is the next closest ethylene glycol molecules. The molecule "1" is the first nearest H-bonded solvent molecule to the ellipticine. Further molecule "2" is the next H-bonded solvents to the molecule "1". The bond lengths are given in Å.

However when water is the solvent we observe different behavior. For water, we find that average the D-A distance for the solvent H-bond close to the strong H-bond of ellipticine-water is about 2.73 Å, while for the other one it is about 2.89 Å. While the latter D-A bond distances are similar to that observed in bulk water [114] suggesting that the weak H bond between ellipticine and water is not affecting the H-bond strength within the solvent, the shorter D-A distance between two water molecules near the strong ellipticine-water H bond suggests that the solvent H-bonds are strengthened due to the strong ellipticine-water H-bond.

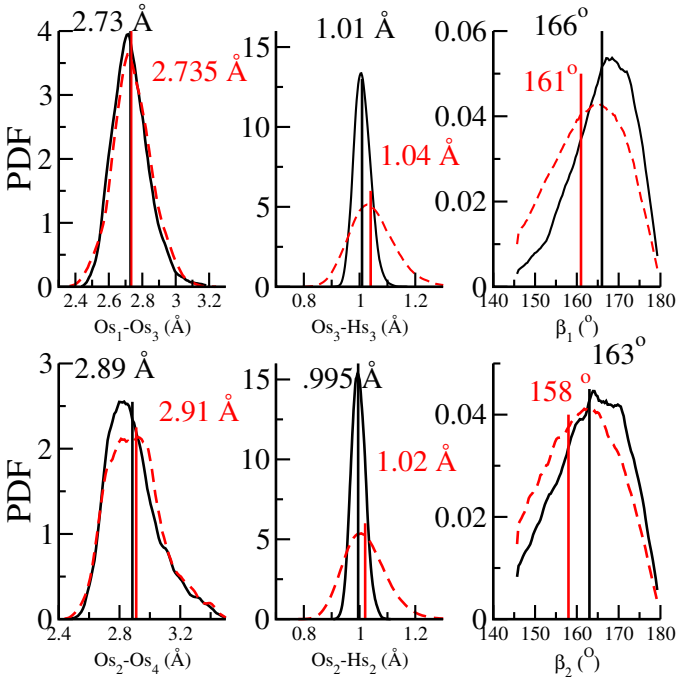

FIGURE 4.12: EP in water: Probability distribution functions of the donor-acceptor distances ((a) and (d)), the donor-hydrogen covalent bond lengths (b), acceptor-hydrogen covalent bond lengths (e), and the donor-hydrogen-acceptor bond angle ((c) and (f)) obtained from BOMD (solid black lines) and PIGLET (dashed red lines) trajectories. The figures in the top panel ((a)-(c)) are for the strong H-bond while those at the bottom panel are for the weak H-bonds. The average values of the above quantities for the BOMD and PIGLET trajectories are shown in black and red dashed lines, respectively. (Top panel: between solvent molecule 1 and molecule 3 and bottom panel: between solvent molecule 2 and molecule 4 as labeled in Schematic representation 4.2)

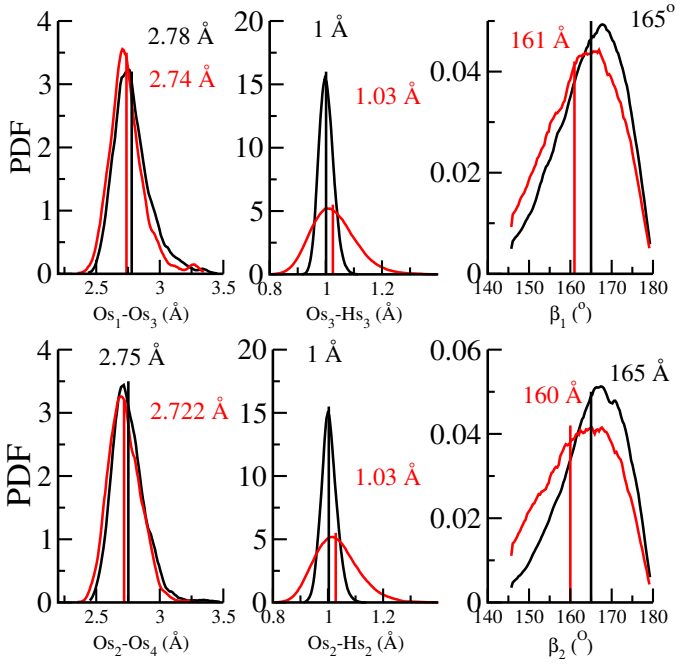

FIGURE 4.13: EP in methanol: Probability distribution functions of the donor-acceptor distances ((a) and (d)), the donor-hydrogen covalent bond lengths (b), acceptor-hydrogen covalent bond lengths (e), and the donor-hydrogen-acceptor bond angle ((c) and (f)) obtained from BOMD (solid black lines) and PIGLET (dashed red lines) trajectories. The figures in the top panel ((a)-(c)) are for the strong H-bond while those at the bottom panel are for the weak H-bonds. The average values of the above quantities for the BOMD and PIGLET trajectories are shown in black and red dashed lines, respectively. (Top panel: between solvent molecule 1 and molecule 3 and bottom panel: between solvent molecule 2 and molecule 4 as labeled in Schematic representation 4.2)

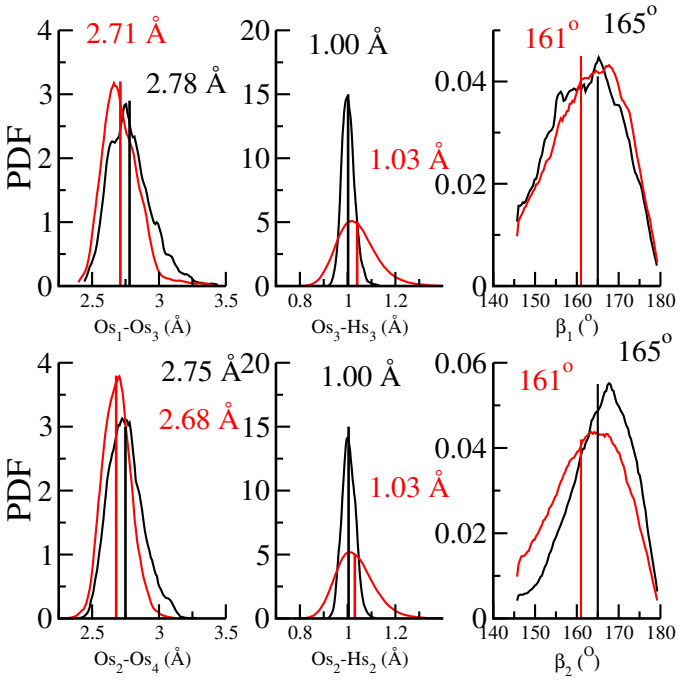

FIGURE 4.14: EP in ethylene glycol: Probability distribution functions of the donor-acceptor distances ((a) and (d)), the donor-hydrogen covalent bond lengths (b), acceptor-hydrogen covalent bond lengths (e), and the donor-hydrogen-acceptor bond angle ((c) and (f)) obtained from BOMD (solid black lines) and PIGLET (dashed red lines) trajectories. The figures in the top panel ((a)-(c)) are for the strong H-bond while those at the bottom panel are for the weak H-bonds. The average values of the above quantities for the BOMD and PIGLET trajectories are shown in black and red dashed lines, respectively. (Top panel: between solvent molecule 1 and molecule 3 and bottom panel: between solvent molecule 2 and molecule 4 as labeled in Schematic representation 4.2)

4.3.3 Electronic absorption spectra of EP in protic solvents

Figure 4.15 shows the experimental spectra of ellipticine in the presence of the three solvents. Also shown are the computed spectra obtained from BOMD and PIGLET trajectories. We find that compared to the experimental spectra, the computed ones are blue-shifted. However, within the computed spectra we find a stark difference between that obtained from PIGLET and BOMD simulations. We find that the PIGLET spectra are much broader compared to the BOMD ones and qualitatively reproduces the experimental ones. It even reproduces well the very broad features in the long wavelength regime of the experimental spectra. Further, we have also listed the λ_{max} in Table 4.4 for the absorption spectra of ellipticine in the three solvents. According to the experimental reports, we observe that λ_{max} is red-shifted as one goes from methanol to ethylene glycol to water. We note that our computed spectra from PIGLET simulations give the correct trend as observed in the experiments. In contrast, we find that the spectra obtained from the BOMD simulations were unable to capture correctly the qualitative behavior of the absorption spectra. This highlights the importance of incorporating the NQEs in the simulations where H-bonding is important to correctly describe the trends in the optical properties of the solvent.

TABLE 4.4: Comparison in the λ_{max} position for absorption spectra of ellipticine in different solvents computed using BOMD and PIGLET with the experimental results. These computed wavelengths are obtained from CAM-B3LYP exchange functional and 6-311++g(d,p) basis set.

Solvents	Experimental (λ_{max},nm)	Classical (λ_{max},nm)	Quantum (λ_{max},nm)
Methanol	285 [73, 76]	273	277
Ethylene glycol	295 [75]	277	279
Water	300 [115]	272	284

4.4 Conclusions

In summary, in this chapter, we have studied how the NQEs are manifested in different protic solvents. In addition to the NQEs on the solvent-solute H-bonding we also discussed the effects on the H-bonding within the solvent molecules. From our simulations we show that as the proton donation capability of the solvent molecules decreases, the strength of the H bond decreases and the NQEs also reduces. Further we find that if the

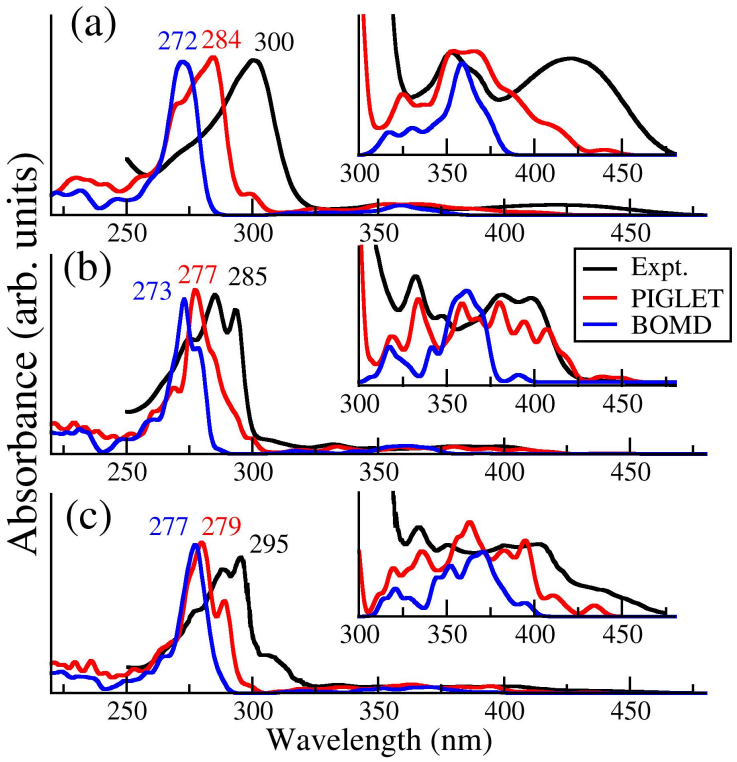

FIGURE 4.15: Comparison of experimental absorption spectra with computed spectra of ellipticine (with CAM-B3LYP exchange functional and 6-311++g(d,p) basis set) in (a) water, (b) methanol, and (c) ethylene glycol. The inset shows that the zoomed part of absorption spectra from 300 nm to 500 nm.

solvent-solute H bond is stronger, the H bonds between solvent molecules in the vicinity of the strong solvent-solute H-bond is strengthened. We find that the broadening of the absorption spectra can be attributed to both the presence of solvents and the importance of nuclear quantum effects in these systems. Finally, we also find that for this case, where H-bonding is important, it is crucial to incorporate the NQEs while computing the absorption spectra in order to reproduce the experimental results qualitatively.

Chapter 5

Descriptors to predict dye-sensitized semiconductor based photocatalyst for hydrogen evolution reaction

5.1 Introduction

As mentioned in the introduction of the thesis, H_2 produced from photocatalytic water splitting is one of the "green" ways to harness and store solar energy by converting it to chemical energy [116–120]. Moreover, H_2 is also used as a raw material for several important chemical reactions [121, 122]. Till date, to the best of our knowledge, the majority of the hydrogen used for the industrial purpose is produced from steam reforming, which is not environment-friendly. Hence it is desirable to produce H_2 from photocatalytic water splitting. However, production of hydrogen from (photo)catalytic water splitting is an endothermic process, requiring about 2.46 eV of energy. Therefore, there is a need for a suitable photocatalyst to speed up the reaction.

Typically semiconductors are used for this purpose. However, the most commonly available, cheap semiconductors like ZnO, TiO_2, etc. have a large band gap (about 3 eV) and hence can absorb only in the ultra-violet (UV) region [123–128]. Further, these have a large amount of defects (primarily in the form of O vacancies) that act as an electron-hole

recombination center, thereby reducing the efficiency of the process. For these reasons, there are efforts to modify these semiconductors such that the effective band gap is reduced (enabling it to absorb in the visible region) and the defects are passivated. Sensitizing semiconductors with dyes is one such way that has been used quite successfully in photovoltaics [31–33]. One of the first reports of using dye-sensitized semiconductors (DSS) is the use of $Ru(bpy)_3^{2+}$-sensitized $Pt/TiO_2/RuO_2$ by Grätzel and co-workers [30, 129]. Following this, there have been several other reports [126, 130–134]. However, the desired synergism for H_2 and O_2 production in a single dye-sensitized system is still far from the desirable solar-to-hydrogen conversion efficiency (30% in terms of quantum yield at 600 nm). For example excitation between NKX-2677-$Pt/H_4Nb_6O_{17}$ and $Pt/WO_3/IrO_2$ results in quantum yield (QY) of about 0.05% for H_2 production under 400 nm light irradiation [129] (NKX-series are derivatives of coumarin dyes with basic C-343 moiety). However, the quantum yield of NKX-2697 is increased by the increase of thiophene rings on NKX-2677 [135]. On the other hand, the rate of H_2 evolution using NKX-2587 (which has no thiophene ring) decreased drastically with increasing irradiation time [129, 135]. In contrast, it has been shown that only photocatalytic H_2 production, rather than the complete water splitting, using dye-sensitized semiconductor suspensions containing sacrificial agents exhibited a higher apparent quantum yield (AQY) [136–141]. For example Pal *et al.* reported about 50% AQY with 10% triethanolamine as the electron donor under 400 nm light irradiation [142]. Hence DSSs with sacrificial agents for H_2 production are widely investigated. Further, there are also a lot of efforts to design novel DSSs with improved efficiency.

Computational material science can help in rational designing of materials for DSSs. Using high throughput screening of semiconductor-dye combinations one can identify possible candidates for DSSs. However, to achieve so it is necessary to have "descriptors" that depends on material properties, correlate with the amount of H_2 production and is computationally inexpensive. Therefore, in this thesis, we have tried to propose some novel descriptors that are easy to compute and can be used to identify novel DSSs. In order to do so it is pertinent to understand the components that are necessary and the associated processes.

For photocatalytic H_2 production from the water reduction half-reaction, the main components are a semiconductor, dye molecules (adsorbed on the semiconductor), an H_2 production cocatalyst and an electron donor. In addition to the fact that the dye should

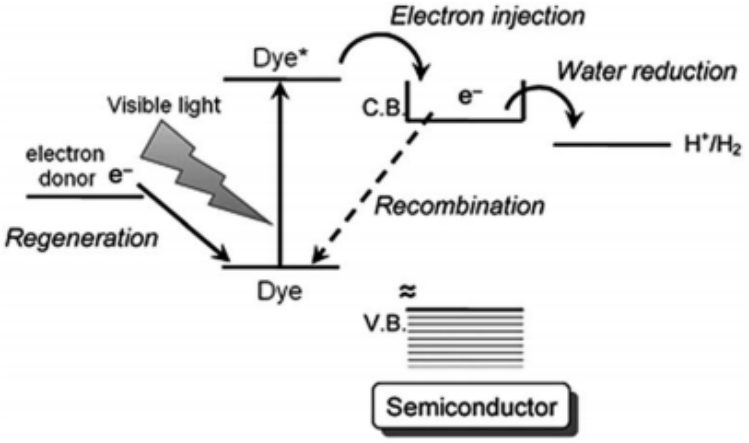

FIGURE 5.1: Typical principle of a dye-sensitized semiconductor for visible light-induced photocatalytic H_2 production from the water reduction half-reaction. Figure reproduced from [6] Copyright© RSC 2016

absorb in the visible region, the DSS composite should have the following properties: (a) the HOMO of the dye should lie in the gap region of the semiconductor and (b) the bottom of the conduction band should be more negative compared to the reduction potential. Further the relevant processes are (i) excitation of dye molecules and transfer of photoexcited electrons from HOMO to LUMO of the molecule, (ii) injection of photogenerated electrons from the dye to the semiconductor's CB, (iii) migration of the CB electrons to the semiconductor surface and H_2 production and (iv) regeneration of the dye molecule for cyclic utilization. In addition to this, there is a detrimental step, i.e., the recombination of the excited electron-hole. These processes are schematically shown in Figure 5.1.

Typically the band alignment is used as a descriptor for identifying possible candidates for DSS. However, to narrow down the material space we propose two novel descriptors, which can be used along with the band alignments of the composite with respect to the oxidation and reduction potentials. To do so we have focused on the injection probability (ease with which photoexcited electron are transferred) of injecting the excited electron from dye to semiconductor and recombination. For electron transfer, we note that the relevant parameters are the coupling strength between dye and semiconductor empty states and the lifetime of the coupled dye state. We also note that electron-hole recombination can be prevented if the electron and hole are spatially separated. Hence we have also taken the electron-hole separation (EHS) as our descriptor. To find the relationship between these three factors with the amount of H_2 evolution, we

have considered composites of ZnO nanoparticles and three azo-based dyes that have been synthesized by Nandini Devi's group at the National Chemical Laboratory, Pune, India. We note that these dyes are not only cheap and easy to synthesize but are also photo-stable. Further, the above mentioned experimental group have performed photocatalytic H_2 production experiments using these composites under similar conditions. Hence the amount of H_2 evolved from each of the samples are comparable. Using this experimental data and our computed value of the descriptors, we have found out the correlation between the descriptor and the amount of H_2 produced. This correlation was used to predict the amount of hydrogen production for another dye that has been experimentally synthesized. The predicted result was compared with the experimental one.

The rest of the chapter is divided as follows. In Section 5.2 we describe the details of computational methods that have been used to determine the lowest energy configuration of the dye and dye-ZnO composite. Section 5.3.1 contains results of the strucure and the electronic structure of the ZnO-Azo dye composite. The methodology to compute the descriptors and their correlation with the amount of hydrogen production for ZnO-azo dye are described in Section 5.3.2. Finally, we summarize our results in Section 5.4.

5.2 Computational details

5.2.1 Lowest energy structure of the dye

In order to determine the ground state of the dye molecules in gas phase we have performed DFT based calculations using the Gaussian Software (G09-rev-D) [92]. We have used PBE exchange-correlation functional [38] and 6-311++G(d,p) basis set. For each of the dyes, we started with the planar configuration and optimized the geometry. Further, we also scanned the potential energy surface (PES) by rotating the β-naphthol group about the $\angle C_1C_2N_1N_2$ and $\angle N_1N_2C_3C_4$, which are marked in Figure 5.2 (a). The results of the dihedral scan are shown in Figure B.1, and Figure B.2 in Appendix B, while the lowest energy configurations are shown in Figure 5.2. We find that the planar configuration is lowest in energy for 4ABBN. Further, we find that the ground state of the molecule is stabilized by the formation of an H bond between the -OH group in β-naphthol moiety and the N_1 atom of the azo group (see Figure 5.2 (a)). In the case of

3AB8HQ and 4AB8HQ, we find that in their lowest energy configuration the molecules are slightly that distorted from the planar structure with $\angle C_3N_2N_1C_2$ dihedral angles of 4° and 5° respectively (see figure 5.2 (b) and (c) for optimized structures). This can be attributed to lone pair (n) of a nitrogen atom (labeled as N_2 in Figure 5.2 (b) and (c)) repelled by nearest C-H of the quinoline moiety.

Similarly, in the case of oligothiophenes, we scanned PES by rotating the two dihedral angles $\angle S_1C_1C_2S_2$ and $\angle S_2C_3C_3S_4$, which are marked in Figure 5.2 (d). The potential energy surface as a function of $\angle S_1C_1C_2S_2$ and $\angle S_2C_3C_3S_4$ dihedral angles are shown in Figure B.3 in Appendix B. We found that the sulphur atoms are arranged in a trans-conformation. Moreover, derivatives of oligothiophenes deviates from the planar shape about 10-15° dihedral angle. This can be attributed to lone pair - lone pair repulsion on the sulphur and C-H bond.

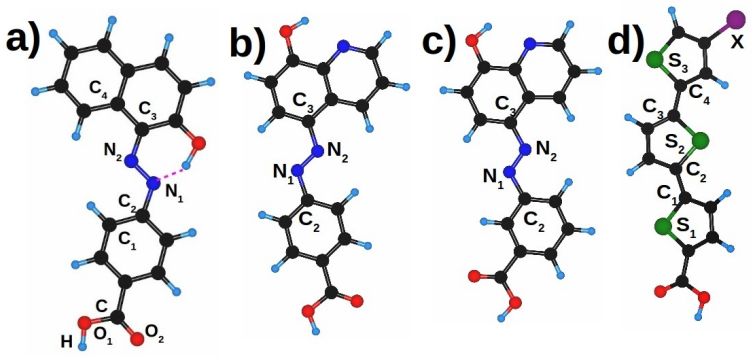

FIGURE 5.2: Lowest energy structure of a) 4ABBN, b) 4AB8HQ, c) 3AB8HQ, and d) oligothiophenes (T_3-X, where X is the substituting group discussed briefly in the text) in the gas phase. The red, black, cyan, dark green, purple, and blue spheres represent O, C, H, S, X, and N atoms respectively. X is the substituted atom such as halogen, electron withdrawing (donating) groups.

Since for the composites we have used Quantum ESPRESSO (QE) software [143], which is a plane wave based code, in order to compute the binding energies of the dye on ZnO, we have recomputed the optimized geometry and total energies of the dyes in gas phase using PBE exchange-correlation functional with QE. For this, we have placed the molecule in a big box such that separation between the periodic images along the three different directions are 8 Å, 6 Å, and 16 Å along x, y, and z-axis respectively (the molecular plane is placed along XZ plane). We find that this is sufficient to avoid the spurious interactions between them. Further, we have used kinetic energy cutoff of 35 Ry and 400 Ry for the plane wave and charge density respectively. We find that the

bond lengths and bond angles for most stable configurations obtained from both the calculations are similar.

5.2.2 ZnO nanoparticle and composite

The calculations were done using the Quantum ESPRESSO software [143], which is a plane wave based implementation of density functional theory (DFT). The electron-ion interactions were described using ultrasoft pseudopotentials [47]. The exchange-correlation potential had been described by the Purdew, Burke and Ernzenhof (PBE) parametrization within the generalized gradient approximation [38, 144]. We have used kinetic energy cut offs of 35 Ry and 400 Ry for the wavefunction and charge density respectively. To test the accuracy of the pseudopotentials used in the calculations, lattice parameters of bulk ZnO in its wurtzite structure and the bond length of an oxygen molecule in the gas phase were determined. The wurtzite structure of ZnO has a hexagonal unit cell. For bulk ZnO, the lattice parameter was found to be 3.29 Å and the c/a ratio to be 1.61. This is in excellent agreement with previously reported experimental values and calculations [145].

Within DFT, the band gap (E_g) of ZnO is severely underestimated (E_g DFT =0.78 eV and E_g experimental =3.3 eV). The wrong positions of the Zn 3d orbitals result in spurious interaction with the sp states of O, which is responsible for this severe underestimation. This can be corrected by many-body techniques, which are almost impossible to use for these large systems due to the enormous computational cost involved in these calculations. Hence we used an alternative technique, which was suggested by Janotti and coworkers [146] and later successfully used by Calzolari et al. [145]. We have used an ad hoc Hubbard U potential within the DFT+U scheme to correct for this band gap underestimation We note that the Hubbard U values included in our calculations are just empirical parameters to correct the gap. Following ref. [145], we have used Hubbard potentials of U = 12.0 eV on the 3d orbitals of Zn and U = 6.5 eV on the 2p orbitals of O. These values of U are obtained by fitting the experimental ZnO bulk band structure.

The ZnO nanoparticles used in the experiment are of diameters 3.5 and 30 nm, which is larger than the Bohr exciton radius of 2.87 nm in ZnO. Hence we expect that quantum confinement effects will not be significant. Therefore we have used the most stable non-polar ZnO $(10\bar{1}0)$ surface to model the ZnO-4ABBN composites. The ZnO $(10\bar{1}0)$ surface

was modelled with an asymmetric slab having six Zn-O bilayers. The slab is oriented such that the surface is normal to the z-axis. The 4ABBN molecule was placed on one side of the slab. To remove the spurious surface effects from the bottom of the slab, it was passivated with pseudo hydrogens [147, 148]. We have used a vacuum of about 20 Å after the molecule is adsorbed on the surface to minimize the interaction between the periodic images perpendicular to the slab. Additionally, to cancel the effects of the spurious dipole moment generated by the presence of the molecule on one side of the slab and pseudo-hydrogen atoms on the other side, we have also applied an external electric field in the direction opposite to that of the dipole moment. Since we are interested in the interaction of the molecule with the substrate, we have used a (5×2) supercell resulting in a minimum separation of about 8 Å between the periodic images of the molecules in the x-y plane. The Brillouin zone integrations had been done using the Gamma point only.

5.3 Results and Discussion

5.3.1 Structure, electronic structure and band alignment of ZnO-azo dye composites

The clean ZnO $(10\bar{1}0)$ surface contains ordered rows of buckled Zn-O dimers along the polar [0001] direction with a net electron accumulation on the O atoms. Our calculations show that 4ABBN binds vertically to the ZnO surface forming a bidentate Zn-O bond through the -COOH group. Further, we observe that, during the relaxation process, the dye molecule spontaneously deprotonates, releasing an H^+ ion from the -COOH group; the latter gets attached to the neighboring electron rich O of the ZnO surface. The newly formed Zn-O bond lengths are about 1.96 and 1.97 Å. We do not observe any distortion of the surface except at the adsorption site where the buckling of the Zn-O dimers are reduced to 0.19 and 0.07 Å compared to that of 0.33 Å on the clean surface. The binding energy of the dye molecule obtained from our calculations is about 1.95 eV, suggesting that 4ABBN is strongly anchored to ZnO.

For the other two azo-dyes, namely, 4AB8HQ and 3AB8HQ, we note that there are two possible ways in which the dyes can anchor to ZnO; either through the -COOH group in the benzoic moiety or through the -OH and N group in the hydroxyquinoline moiety. We

performed calculations for both the anchoring configurations and found that the dyes prefer to bind to ZnO through -COOH group. Similar to 4ABBN, for these two cases also we find that the dye gets deprotonated and form bidentate Zn-O bonds. The Zn-O bond lengths are similar (±0.03 Å variations compared to 4ABBN) to that observed for 4ABBN. However, the binding energy is about 0.5 eV lower than that observed for 4ABBN.

The density of states (DOS) of the ZnO-4ABBN is shown in Figure 5.3(a). The electronic states are aligned with respect to the energy at vacuum. We find that upon modifying the surface of the ZnO nanoparticles with 4ABBN, the effective band gap of the interface is reduced to 1.47 eV compared to that of 3.77 eV for the clean slab. Figure 5.3(a) also shows the contribution of the ZnO (red circles) and dye (blue) states to the total DOS. Our calculations show that the valence band maximum (VBM) of the interface is localized on the dye molecule (Figure 5.3(c)) and the conduction band minimum (CBM) is localized on the slab (Figure 5.3(d)). Additionally, there is a weight of the wavefunction on the O atoms of the azo-dye through which it binds to the ZnO slab indicating that there is a possibility of fast electron transfer from the dye to the ZnO. The interface is thus converted to a staggered type II interface, which facilitates absorption in the visible region as observed in the experimental absorption spectra of ZnO-4ABBN [149].

To explore the possibility of using the composites as photocatalysts for water splitting, we looked into the positions of the oxidation potential (OP) of oxidizing H_2O to O_2 and the reduction potential (RP) of reducing H^+ to H_2 with respect to the positions of VBM and CBM of the ZnO-4ABBN composite. The absolute values of the OP/RP are given by

$$E_{abs}^{OP/RP} = -4.5 - E_{NHE}^{OP/RP}, \tag{5.1}$$

where $E_{abs}^{OP/RP}$ is the absolute value of the OP/RP and $E_{NHE}^{OP/RP}$ is the OP/RP potential in V vs. the NHE at pH 0. E_{NHE}^{OP} is 1.23 eV and E_{NHE}^{RP} is 0.00 eV. From our calculations we find that the absolute values of OP and RP are -5.73 eV and -4.5 eV respectively. Thus the OP is about 0.06 eV above the VBM (Figure 5.3) and the RP is 0.18 eV below

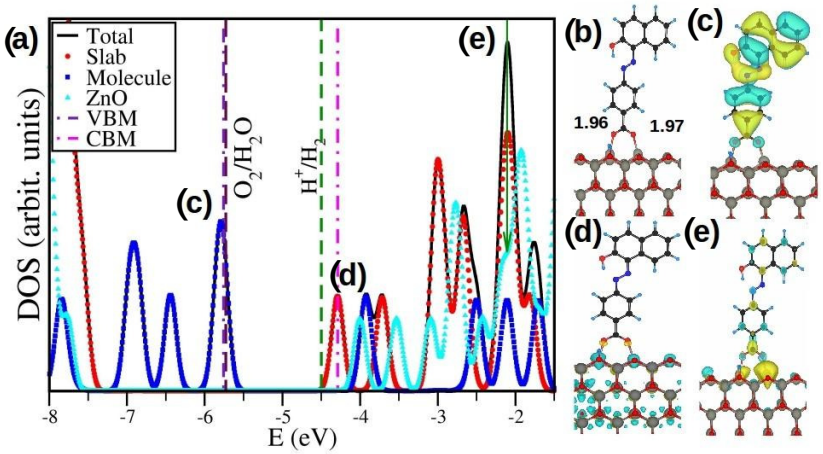

FIGURE 5.3: (a) DOS of the ZnO-4ABBN composite. Dot-dashed violet and magenta vertical lines mark the VBM and CBM respectively. The dashed brown and green lines mark the OP and RP. (b) Optimized structure of 4ABBN on ZnO($10\bar{1}0$). The grey, red, black, cyan and blue spheres represent Zn, O, C, H and N atoms respectively. The bond lengths are given in Å. (c) The wavefunction corresponding to the VBM. (d) The wavefunction corresponding to CBM. (e) The wavefunction of a coupled state.

the CBM (Figure 5.3). These results suggest that thermodynamically water splitting reaction will be catalysed by the ZnO-4ABBN composite.

Similarly, Figure 5.4 and Figure 5.5 show the density of states (DOS) and the wavefunctions of the frontier orbitals of 3AB8HQ and 4AB8HQ composites respectively. These two composites are iso-electronic with 4ABBN dye where the β-naphthol moiety of 4ABBN has replaced with the hydroxyquinoline (HQ) moiety. For 4AB8HQ the HQ moiety with N=N is placed at the ortho position of benzoic acid, while for 3AB8HQ it is placed at the meta position. The wavefunction corresponding to VBM of both composites are localized on the azide forming a "n" type state and VBM-1 is a "π" state that is delocalized over the dye molecules. We note that this is in contrast to what we observed for 4ABBN where the HOMO is a π-state delocalized over the molecule. Further we also looked into the position of VBM and CBM w.r.t. the OP and the RP for these two composites. For both the dyes we find that the position of VBM (CBM) is above the OP (RP) of water (H^+). This suggests that while oxygen evolution is thermodynamically unfavourable for these composites, hydrogen evolution is possible provided one uses some hole scavengers, eg. methanol, to remove the holes that can be accumulated in the dye during the reaction.

The positions of the important bands (CBM, VBM and the coupled empty state) for the three composites are summarized in Table 5.1. Additionally we also list the difference

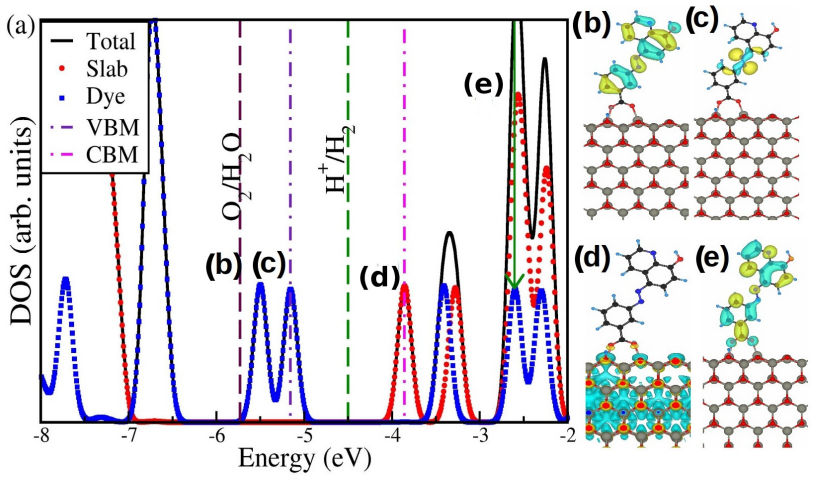

FIGURE 5.4: (a) DOS of the ZnO-3AB8HQ with -COOH anchoring. Dot-dashed violet and magenta vertical lines mark the VBM and CBM respectively. The dashed brown and green lines mark the OP and RP. (b) The wavefunction corresponding to the VBM-1. (c) The wavefunction corresponding to the VBM. (d) The wavefunction corresponding to CBM. (e) The wavefunction of a mixed state. The grey, red, black, cyan and blue spheres represent Zn, O, C, H and N atoms respectively. The bond lengths are given in Å.

between positions of RP and CBM.

TABLE 5.1: Important energy levels of 4ABBN, 4AB8HQ, and 3AB8HQ composites. All values are in eV. These dyes are arranged in decreasing order of resonance. All these dyes are iso-electronic.

Dye	VBM	CBM	Coupled	RP-CBM	Band gap
4ABBN	-5.79	-4.32	-2.11	0.18	1.47
4AB8HQ	-5.32	-3.98	-1.76	0.41	1.34
3AB8HQ	-5.16	-3.86	-2.60	0.57	1.30

5.3.2 Computation of descriptors

As discussed in the introduction, apart from the correct band-alignment, there are three more important aspects concerning the use of dye-sensitized semiconductors as photocatalysts for hydrogen evolution. They are (i) strength of coupling between the dye and the semiconductor states, (ii) lifetime of the coupled state when dye is excited and (iii) the separation between the electron and the hole in the coupled state. A rigorous computation of these quantities involves performing many body excited state calculations that are expensive [1, 2]. Rather, based on the recipe provided in Ref [150], we have used single particle ground state picture to have estimates of the above mentioned quantities.

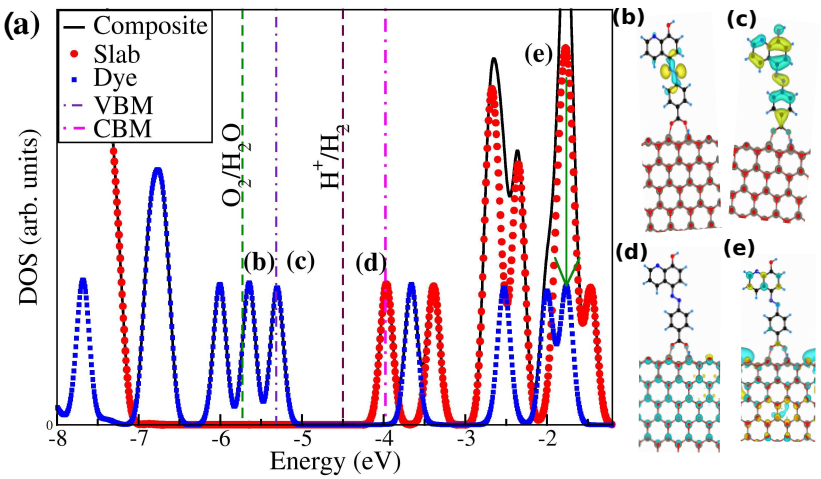

FIGURE 5.5: (a) DOS of the ZnO-4AB8HQ with -COOH anchoring. Dot-dashed violet and magenta vertical lines mark the VBM and CBM respectively. The dashed brown and green lines mark the OP and RP. (b) The wavefunction corresponding to the VBM-1. (c) The wavefunction corresponding to the VBM. (d) The wavefunction corresponding to CBM. (e) The wavefunction of a mixed state. The grey, red, black, cyan and blue spheres represent Zn, O, C, H and N atoms respectively. The bond lengths are given in Å.

The efficiency of the electron injection from the dye excited state to ZnO depends on the strength of the matrix elements coupling the dye empty states with the ZnO CB, the lifetime of the electron in the excited state within the dye and the availability of the density of the states in the CB of ZnO for the transfer to happen. A reasonably good estimate of the lifetime is given by the full-width at half maxima ($FWHM$, σ) of the peak of the empty states of the dye molecule in the projected DOS of the composite. The combined effect of the coupling strength and the availability of the density of states (DOS) can be incorporated in a single quantity called the coefficient of injection (C_{inj}) and is given as:

$$C_{inj} = \int_{\sigma} g_{dye}(E) g_{ZnO}(E) dE, \tag{5.2}$$

where g denotes the density of states (DOS) and E, the electronic energy. The integral is carried out over an energy interval equal to σ, centered about the empty state of the molecule.

If the electron is excited to a dye state that is long-lived and strongly coupled to the CB of ZnO, the probability of injecting the electron to ZnO will be easier. Moreover, for this state it is also desirable that the spatial separation of the electron and hole (EHS) is

large so that the probability of recombination can be reduced. The EHS of the electron and hole in the j^{th} state is approximated by:

$$EHS = \frac{\int r\rho^{j}(r)dr}{\int \rho^{j}(r)dr} - \frac{\int r\rho^{VBM}(r)dr}{\int \rho^{VBM}(r)dr} \tag{5.3}$$

where r is the position coordinate and ρ corresponds to the charge densities of the VBM and the empty coupled states. The first (second) term in equation 5.3 is an approximation of the center of mass of the electron (hole). We note that here we have implicitly assumed that the electron is always excited from the HOMO of the dye (VBM of the composite) to the empty state.

Figure 5.3 and Table 5.2 give that the values of the above-mentioned parameters for the first 15 empty states above the CBM of ZnO-4ABBN. We computed only up to CBM+15 because this particular state is the lowest energy one in the conduction band of the composite where one can observe a strong coupling. Additionally to incorporate all the effects together, we have also computed and reported the product of C_{inj} and EHS. We find that for the low-lying empty states the EHS are quite large because for these empty states the wavefunctions are localized on ZnO while the HOMO is localized on the molecule. Hence upon allowed excitation the holes will be spatially localized on the molecule and electrons on ZnO. For the state that has the strongest coupling (CBM+15, for the wavefunction please refer to Fig 5.3 (e) we also find that EHS is reasonably large suggesting that the electron excited to this state of the dye will be easily injected to ZnO.

We have performed a similar analysis for 3AB8HQ and 4AB8HQ composites. The different parameters related to charge injection for the most strongly coupled states is given in Table 5.3. Additionally we have also quoted the experimental values of the amount of hydrogen evolved when the three composites are used for hydrogen evolution reaction. The experiments are performed in presence of 35 $v/v\%$ methanol as hole scavenger for each of the composites. Other experimental details can be found in Ref [149, 151]. The amount of H_2 (AMH) evolved for these dyes as a function of the different parameters, namely C_{inj}, EHS, and $C_{inj} \times EHS$ are plotted in Figure 5.6. We find that while C_{inj} and $C_{inj} \times EHS$ are linearly correlated with the amount of H_2 production

TABLE 5.2: Descriptors for 4ABBN-ZnO composite for all the 16 states of CBM to CBM+15

j*th* coupled state	σ (eV)	C_{inj}	EHS (Å)	$C_{inj} \times EHS$
CBM	0.012	0.390899	1.724	0.67391
CBM+1	0.012	0.269202	15.221	4.09752
CBM+2	0.013	0.542891	15.245	8.27637
CBM+3	0.013	0.292074	15.841	4.62674
CBM+4	0.013	0.258176	14.679	3.78977
CBM+5	0.013	0.428301	15.261	6.5363
CBM+6	0.013	0.55075	13.962	7.68957
CBM+7	0.013	15.8351	3.245	51.3849
CBM+8	0.012	17.1248	2.681	45.9116
CBM+9	0.013	12.242	12.125	148.434
CBM+10	0.012	10.3373	14.123	145.994
CBM+11	0.013	0.519549	13.740	7.1386
CBM+12	0.012	0.348069	13.428	4.67387
CBM+13	0.012	1.1404	4.963	5.65981
CBM+14	0.013	59.9047	6.784	406.393
CBM+15	0.013	161.237	10.547	1700.57

(R= 0.998 for C_{inj} and R= 0.999 for the product), EHS shows a linear anticorrelation (R=0.995). The equations of the straight line obtained from the linear fit are given by:

$$\begin{aligned} AMH &= 0.03764(C_{inj}) - 2.43964 \\ AMH &= -0.631836(EHS) + 10.2043 \\ AMH &= 0.0071446(EHS \times C_{inj}) - 8.55841 \end{aligned} \tag{5.4}$$

The anti-correlation behavior for EHS can be understood as follows. For a given composite the largest possible EHS is obtained when the electron is completely localized on ZnO and the hole on the dye. However, this also implies that to achieve this the coupling between the empty state of ZnO and dye has to be negligible or zero and as explained earlier a weak coupling results in less efficient electron injection. Therefore one observes anti-correlation between EHS and the amount of H_2 evolved. This also implies that for the composite it is necessary to have an optimal value of EHS maintaining the subtle balance between prevention of carrier recombination and electron injection.

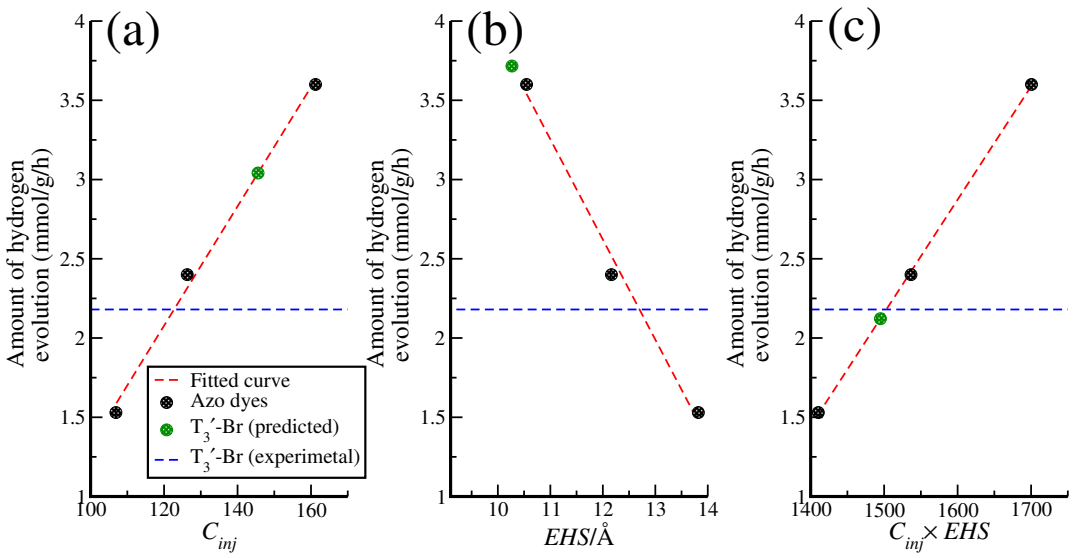

FIGURE 5.6: Amount of hydrogen evolution (AMH) in the reaction plotted against a) C_{inj}, b) EHS (Å), c) product of C_{inj} and EHS. Red dashed lines represents the fitted curve from azo dye composites. Blue dashed lines represent an experimental AMH of T_3'-Br.

TABLE 5.3: Descriptors of the coupled state of photosensitizers (azo dyes).

Sensitizers	C_{inj}	EHS (Å)	$EHS \times C_{inj}$	σ (eV)	Band gap (eV)	Amount of HER (mmol/g/8h)
4ABBN	161.237	10.547	1700.57	0.012	1.62	3.60
4AB8HQ	126.315	12.165	1536.56	0.013	1.34	2.40
3AB8HQ	106.89	13.821	1410.48	0.013	1.16	1.53

5.3.3 Testing the descriptors

In this section, we test how efficiently the descriptors can predict H_2 evolution for a different ZnO-dye composite. For this purpose, first, we have performed several calculations on composites of ZnO and oligothiophenes. Thiophene, which is a basic monomer unit of oligothiophene, is an aromatic heterocyclic compound having 6π-e^- cyclic system with two lone pairs of electrons on sulphur. One of the lone pair on sulphur atom in the thiophene moiety is involved in the aromatic sextet and the other is located in an sp^2 hybridized orbital in the plane of the ring. In our study we have considered parent oligothiophenes (up to a maximum of three thiophene rings) and their derivatives that are obtained by substituting the H in the "′" and "″" positions of the thiophene unit farthest from the -COOH anchoring group with halogens (viz Cl and Br) and electron withdrawing groups (-CN, -NO_2). These are schematically shown in Fig 5.7 and corresponding VBM and CBM of the composites are shown in Fig 5.9

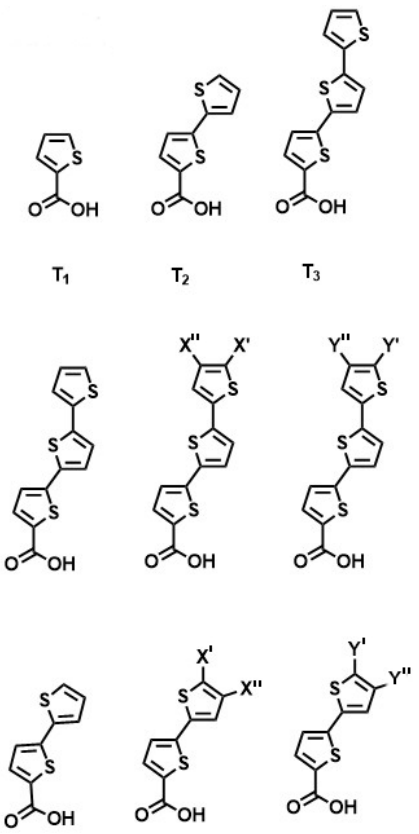

FIGURE 5.7: Sketch of oligothiophene-2-carboxylic acids, T_n, n ranges from 1 to 3 thiophene units. X - halogens (Cl and Br) and Y - electron withdrawing groups (-CN, $-NO_2$). X′ (Y′) and X″ (Y″) are substituting groups on first nearest carbon atom to sulphur atom and second position nearest carbon atom to sulphur atom of thiophene respectively.

Upon interacting with ZnO, we find that the molecules prefer to bind vertically to ZnO through the -COOH group. The molecules are distorted by 10 to 12° at dihedral angles $\angle C_1S_1C_2S_2$ and $\angle C_3S_2C_4S_3$. These distortions are due to the lone pair (n) on sulphur atom and nearest C-H bond of thiophene ring. Further these distortions change on introducing "X" group by ±3-4°. The binding energies of the different molecules are shown in Figure 5.8. The details of the DOS for each of the composites are given in Section B.3 in Appendix B.

To identify the most suitable candidates for H_2 evolution photocatalyst, we begin by computing the band structure and looking at the level alignment of the VBM and CBM with respect to the oxidation and reduction potentials. The band alignment is shown in Figure 5.9. For all the composites we find that the VBM is localized on the dye and the CBM is on ZnO slab. Further, we also find that most of the composites, except -C=N and $-NO_2$ substitutions on oligothiophenes are suitable for H_2 evolution. For the

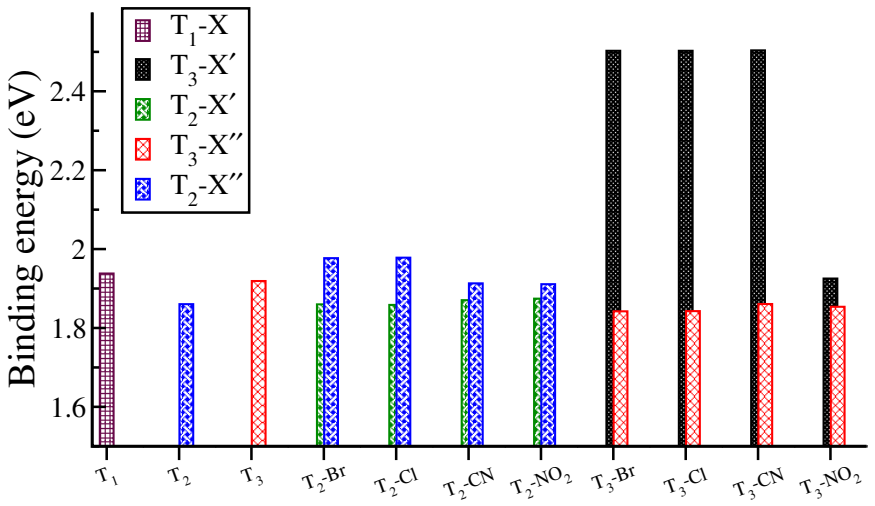

FIGURE 5.8: Binding energy of oligothiophene-2-carboxylic acid derivatives. X is the substitution group.

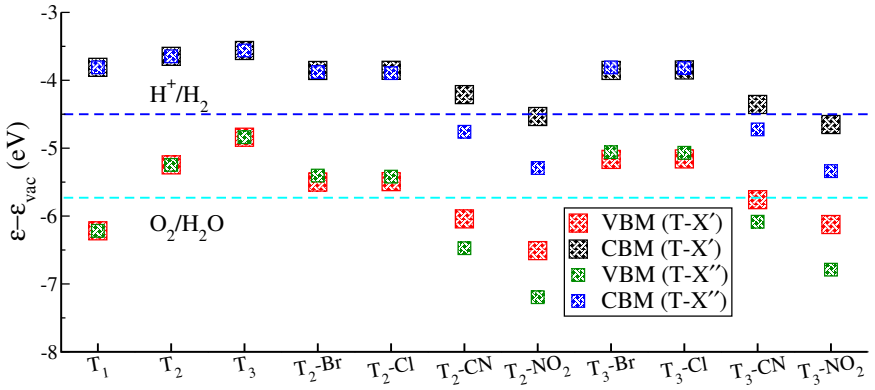

FIGURE 5.9: VBM (red and green) and CBM (black and blue) energy alignment for the considered oligothiophene molecules in the gas phase with electron withdrawing groups on ortho and meta position of thiophene molecule, shifted with respect to the vacuum level. The blue and cyan dashed lines are OP and RP of water splitting respectively.

cases where we observe the desirable band alignment, we computed σ, EHS, C_{inj} and $EHS \times C_{inj}$. These are listed in Table 5.4.

From our calculations, we find that the halogen-substituted oligothiophenes with three thiophene rings have largest value of C_{inj}. Amongst these, we have experimental results for T$_3$′-Br. Using the values of EHS, C_{inj} and $EHS \times C_{inj}$ from Table 5.4 for T$_3$′-Br composite in Equations 5.4, we have predicted the amount of H_2 that can be produced using T$_3$′-Br-ZnO composite and compared with the experimental results. The predicted values are plotted in Figure 5.6 (green filled circle). The experimental value for the same is indicated by the horizontal blue dashed line. We find that using EHS and C_{inj} individually as descriptors, the predicted and measured values are significantly different. In contrast, using the product of the two, i.e., $EHS \times C_{inj}$, as a descriptor,

TABLE 5.4: Descriptors of the coupled state of photosensitizers Oligothiophenes and their derivatives.

Sensitizers	C_{inj}	EHS (Å)	$EHS \times C_{inj}$	σ (eV)
T_1	26.818	7.8900	211.590	0.013
T_2	33.255	12.356	410.904	0.012
T_2	54.673	11.028	602.934	0.038
T_3	30.259	12.216	369.643	0.012
T_2''-Br	89.695	15.570	1396.81	0.013
T_2''-Cl	43.626	12.180	531.448	0.013
T_2'-Br	35.111	11.750	412.523	0.012
T_2'-Cl	26.816	11.710	313.935	0.012
T_2'-CN	30.228	11.320	342.146	0.012
T_2'-NO_2	19.019	6.3050	119.914	0.013
T_3'-Br	145.58	10.269	1494.96	0.012
T_3'-Cl	112.96	10.108	1141.81	0.013
T_3'-CN	16.737	8.2950	138.833	0.012
T_3''-Br	114.31	12.666	1447.83	0.015
T_3''-Cl	129.49	12.745	1650.39	0.016

we find that the predicted and measured values are in excellent agreement. The failure of the individual quantities to predict the amount of H_2 evolution can be understood from the fact that both these processes are interconnected and it is necessary to have a subtle balance between the two.

5.4 Summary

In summary, using a combination of computational tools and controlled experimental measurements we have proposed that the product of separation between the electron and hole and the electron injection efficiency of the composite can be used as descriptors to predict novel dye-sensitized-semiconductor composites as photocatalysts for H_2 evolution. We note that at present in our calculations we have neglected the solvent effect. Moreover, the data points are too few and more studies need to be done to validate this proposal.

Chapter 6

Summary and outlook

6.1 Part I

In this part, we have studied the nuclear quantum effects on the structural, dynamical, and spectroscopic properties of the normal form of ellipticine in protic solvents such as water, methanol, and ethylene glycol. We have used path integral molecular dynamics along with a recently proposed colored noise thermostat based on the generalized Langevin equation for nuclear quantum effects. From the results of our calculations on ellipticine in water, that are presented in Chapter 3 of this thesis we find that NQE increases the fluctuations, not only in the light protons of the H-bonded network of solvent and ellipticine molecule but also affects different ellipticine bond lengths formed from the relatively heavier C and N nuclei. For the total duration of our simulations, we find that there are small but significant instances of proton transfer to and from the solvent resulting in a protonated and deprotonated form of ellipticine. Our studies suggest that protonation or tautomerization of ellipticine in water is kinetically unfavourable and most probably occurs in the excited state. In contrast to the cases where the H-bond donors and acceptors have same proton affinity, we find that for ellipticine in water case, where the proton affinities of the donor and acceptor are different the NQE strengthens both the weak and the strong H bonds with the former being significantly more strengthened than the latter.

Further, to test whether this is a general phenomenon or not we extended our study to two more solvents, namely, methanol and ethylene glycol. As we move from water to

methanol to ethylene glycol, the H-bond donating capability of the solvent molecules decrease. Our results presented in Chapter 4 show that as the proton donation capability of the solvent molecules decreases, the strength of the H bond decreases and the importance of NQEs also reduces. Further, we also investigated how the H-bond between the solvent molecules are affected in presence of solute-solvent H-bonding. We find that if the solvent-solute H bond is strong, the H bonds between solvent molecules in the vicinity of the strong solvent solute H-bond is strengthened while the weak solute-solvent H bond does not perturb the H-bonding between solvent molecules.

Another important outcome of our simulations is the effect of the quantum nature of the nuclei on the optical properties of the solvated molecules. Our simulations show that even to qualitatively reproduce the experimental results, for example broadening of the absorption spectra and trends in the shift of the absorption spectra maxima, it is crucial to incorporate the NQEs in the simulations. Moreover, from the comparison of the absorption spectra obtained from BOMD and PIMD simulations, we could also separate out the contributions in the shift in the absorption maxima due to the effect of the solvent and delocalization of the light nuclei because of their quantum nature.

We propose that our predictions can be verified experimentally by (a) the proton bound to the pyrrole N of ellipticine and (b) using D_2O as a solvent instead of water. While the former will elucidate the role NQE on the absorption spectra due to the weak pyrrole H bond, the latter will throw light on the effect of NQE on the absorption spectra due to the strong H bond at the pyridine N. Since our study shows that NQE strengthens both the H bond, we expect a blue shift of the adsorption spectra along with a reduction in the broadening of the peaks.

6.2 Part II

In the second part of the thesis, we have proposed novel descriptors that can be used for screening semiconductors photosensitized with dyes to identify probable candidates as a photocatalyst for the photocatalytic hydrogen evolution reaction. To propose the descriptors we have used ZnO-azo based dyes. From our calculations and careful controlled experiments using these composites, we have shown that the product of the

computed electron injection probability from dye to ZnO and the electron-hole separation correlates linearly with the amount of H_2 gas evolved when these composites are used as a catalyst. To test this hypothesis we have scanned through a family of ZnO-oligothiophenes (both parent and substituted) composites, computed the descriptors for them, identified the best candidate and predicted the amount of H_2 that will be evolved when this will be used as a photocatalyst. Our predicted results were found to be in excellent agreement with the experimental performed on the same photocatalyst, thus suggesting that our proposed descriptor works reasonably well for this particular family of ZnO-dye composites.

Though the initial results are promising, we note that for both classes of dyes, the semiconductor is the same. To test the generality of the proposed descriptor we need to perform several calculations using a different class of semiconductor-dye systems. Moreover, we have done these calculations considering that the composite is in vacuum. However, in realistic scenario solvents are present. Therefore it will be interesting to study how these descriptors will behave in the presence of solvents.

Appendix A

Appendix A

A.1 Radial distribution function

Figure A.1 shows the results of the g(r) between the center of mass of ellipticine and O of water obtained from the classical molecular dynamics simulations. The first and second solvation shells are at 5.4 Å and 7.45 Å (blue dashed lines, Figure A.1) respectively. This has been computed from the trajectory of a classical molecular dynamics run with a larger system, we find that water around the EP is structured only till the second solvation shell. Hence, we extracted a smaller cubic system for BOMD and PIGLET simulations, which comprising of one ellipticine and 87 water molecules in a cubic box with sides 14.9 Å each. Therefore, we envisage that the results are not affected by the system size in ground state.

Figure A.2 and A.3 shows the g(r) plots of the O atoms of a water molecule and center of mass of ellipticine and oxygen in water respectively obtained from the BOMD trajectory.

A.2 NQE on structural properties of ellipticine:

Probability distribution functions of different bond lengths in ellipticine: We observe that the nuclear quantum effects (NQE) result in a significant broadening of N_6-H_6, aromatic C-H, and aliphatic C-H bonds. Though the average bond lengths for these three type of bonds increases by about 0.01-0.02 Å, is noteworthy is that the width of the PDFs of these bonds increases enormously because of the nuclear quantum effects.

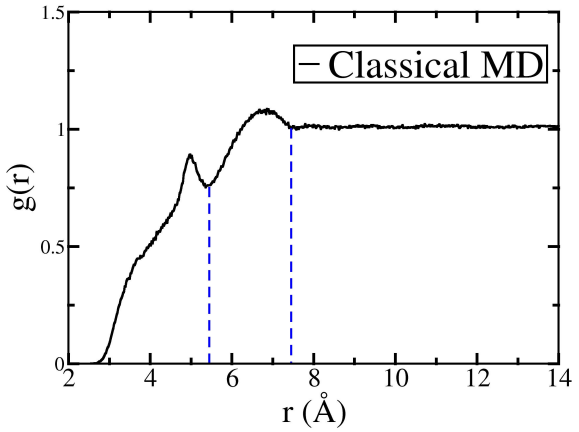

FIGURE A.1: The radial distribution function of the center of mass of ellipticine and oxygen of water molecule. The blue dashed lines indicate solvation shells. This RDF is obtained from classical MD simulations.

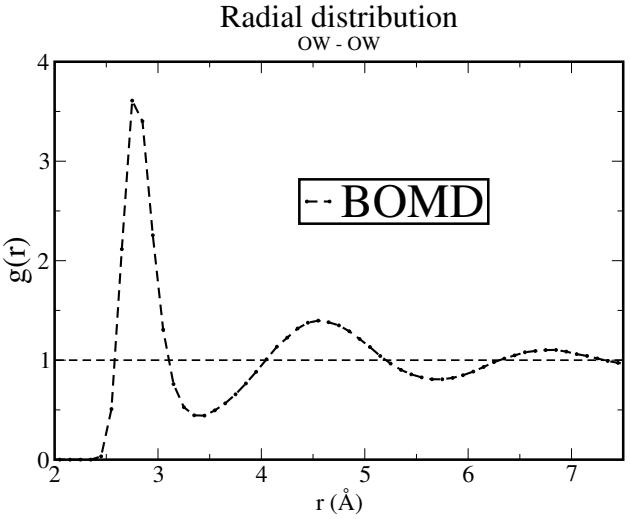

FIGURE A.2: The radial distribution function of the oxygen atoms of water molecule obtained from the BOMD simulations. The coordination number of oxygen atoms in the first solvation shell (at 3.42 Å) is 4.2 and the first peak position at 2.72 Å.

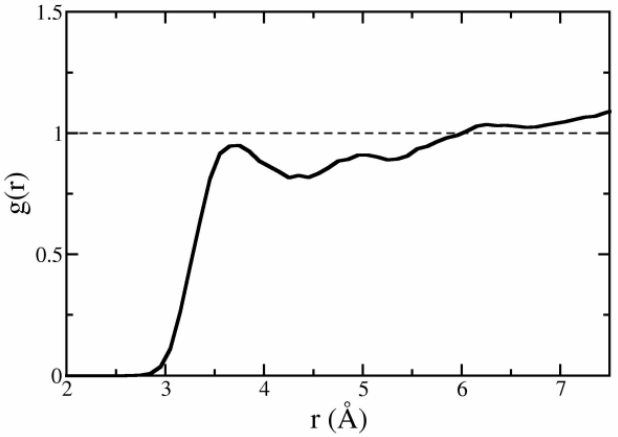

FIGURE A.3: The radial distribution function of the center of mass of ellipticine and oxygen in water molecule obtained from the trajectories of BOMD simulations.

A.2.0.1 Quantum effects on covalent bond

Inclusion of quantum nature of the nuclei not only changes the H-bond strengths involving the light protons of water and ellipticine, but also the bonds between the heavy nuclei (namely C and N) in the molecule. Comparing the PDFs of the different C-C i.e, single and double bond lengths and C-N bond lengths of the ellipticine molecule obtained from the BOMD and PIGLET trajectories we find that (a) there is significant broadening of the PDF, originating from the fluctuations induced by the quantum nature of the nuclei and (b) there is a slight increase in the average bond lengths. For most of the bonds, including the strong C=N and C=C bonds, the full-width half maxima of the PDF almost doubles on the inclusion of NQE. This suggests that NQE not only affect the light protons but it is also important even for the heavier nuclei. The PDFs for the other bond lengths, average bond length values and the spread in the bond lengths are given in Table A.1 and Figure A.6. We note that similar effects of NQE on the heavy nuclei have also been observed in complex biomolecules [79] and other inorganic systems like graphene [108].

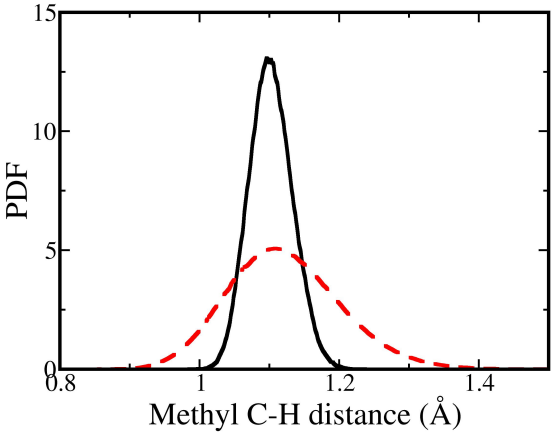

FIGURE A.4: Probability distribution function of methyl C-H bond length. The black solid line and red dashed line represent the PDFs of the bond length obtained from BOMD and PIGLET simulations respectively.

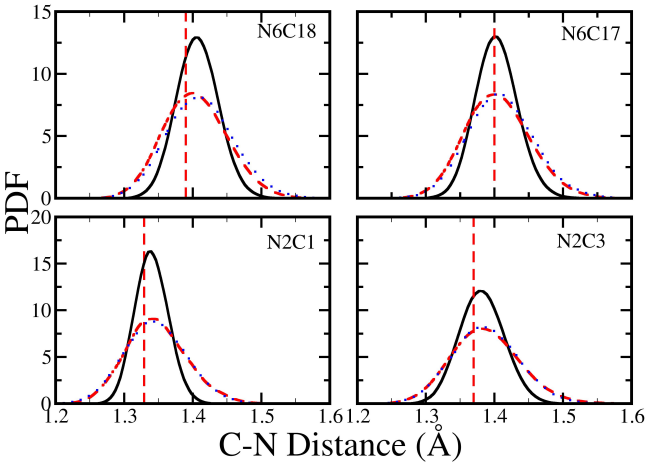

FIGURE A.5: Probability distribution function of $\langle C-N \rangle$ bond length. The black solid line and red dashed line represent the PDFs of the bond length obtained from BOMD and PIGLET simulations respectively.The vertical line represents the equilibrium bond length in gas phase geometry of EP.

TABLE A.1: Average bond lengths and full-width at half maxima (FWHM) of the PDF of the different C-C, C=C, C-N, C-H and N-H bonds are obtained from BOMD and PIGLET simulations of the normal form of ellipticine in water. Also given are the corresponding bond lengths of ellipticine in the gas phase.

Bond	Bond length BLYP/TZVP (Å)	Average bond length/ Peak maxima, (Å)		Broadening/ FWHM, (Å)	
		BOMD	PIGLET	BOMD	PIGLET
N_6-H_6	1.01	1.03	1.05	0.061	0.174
Methyl C-H	1.09-1.10	1.10	1.12	0.073	0.185
Aromatic C-H	1.09	1.09	1.10	0.065	0.183
N_2=C_1	1.33	1.34	1.34	0.058	0.109
N_2=C_3	1.37	1.38	1.38	0.078	0.117
N_6=C_{17}	1.40	1.40	1.41	0.072	0.116
N_6=C_{18}	1.39	1.40	1.41	0.072	0.117
C-C	1.52	1.52	1.53	0.077	0.120
C_8=C_9	1.41	1.42	1.42	0.063	0.117
C_7=C_8	1.40	1.41	1.42	0.060	0.113
C_7=C_{18}	1.41	1.42	1.42	0.061	0.115
C_3=C_4	1.38	1.39	1.39	0.062	0.113
C_{19}=C_{18}	1.43	1.44	1.44	0.065	0.117
C_{16}=C_{17}	1.46	1.48	1.48	0.070	0.118

A.2.0.2 The joint probability distribution function (JPDF):

Definition: Given random variables X, Y that are defined on a probability space, the joint probability distribution for X, Y is a probability distribution that gives the probability that each of X, Y falls in any particular range or discrete set of values specified for that variable. This is also known as bivariate normal distribution.

The bivariate normal distribution is the statistical distribution with probability density function

$$P(x_1, x_2) = \frac{1}{2\pi\sigma_1\sigma_2\sqrt{1-\rho^2}} exp\left[-\frac{z}{2(1-\rho^2)}\right], \tag{A.1}$$

where

$$z \equiv \frac{(x_1-\mu_1)^2}{\sigma_1^2} - \frac{2\rho(x_1-\mu_1)(x_2-\mu_2)}{\sigma_1\sigma_2} + \frac{(x_2-\mu_2)^2}{\sigma_2^2}, \tag{A.2}$$

and

$$\rho \equiv cor(x_1, x_2) = \frac{V_{12}}{\sigma_1\sigma_2} \tag{A.3}$$

is the correlation of x_1 and x_2 and V_{12} is the covariance. μ is the mean or expectation of the distribution, σ is the standard deviation, and σ^2 is the variance.

A.3 Convergence of absorption spectra with respect to the number of explicit water molecules

Before we compare our computed spectra with the experimental one we would like the highlight the importance of performing careful convergence test of the computed spectra as a function of number of explicit water molecules, particularly in case of PIGLET trajectory. Figure A.7 (a) and (b) show how the position of the main peak and the lowest energy peak evolves as a function of the number of water molecules for three randomly chosen snapshots from the BOMD and the PIGLET trajectories respectively. The water molecules are chosen based on the distance between the center of mass of ellipticine and water. We start from the one that has the smallest distance and keep on adding more water molecules. We find that at least 45 water molecules ($\sim$ the first solvation shell) are required to get converged spectra. A careful look at the plots of both the BOMD and PIGLET snapshots show that the fluctuations in the peak positions seem to saturate when about 25 water molecules are added. However, as we keep on adding more water molecules, we find that there is a sudden red shift in the peak positions after which the peak positions do not change. These are highlighted by the blue circles in Figure A.7 (a) and (b). Interestingly we find that these are the points where the water molecule that is close to the pyrrole N of ellipticine is explicitly included in the calculation of the absorption spectra. This tells us that it is important to include this particular water molecule explicitly, the reason being this water molecule interacts strongly with ellipticine through H-bond formation while the other water molecules interact with the ellipticine through OH-π interactions. This motivated us to check whether we can reproduce the time-averaged ellipticine spectra using 45 explicit water molecules with a lesser number of water molecules.

In Figure A.7 (c) and (d) we show the time-averaged spectra of ellipticine obtained from the BOMD and PIGLET trajectories respectively. The time-averaged spectra is computed in four different ways: (a) taking the dehydrated ellipticine obtained from the MD trajectories, (b) adding two explicit water molecules, one near the pyridine N that we found to be crucial from the analysis described in the previous paragraph and the second one near the pyrrole N, (c) 26 explicit water molecule, of which 25 water molecules are those whose center of mass is closest to that of the ellipticine and the 26^{th} one is the one forming H-bond with ellipticine and (d) with 45 explicit water molecules

as found from the convergence test above. In each of these cases we have included the implicit solvent effect through the PCM model. For the spectra obtained from BOMD trajectory (Figure A.8(c)), we find that the inclusion of explicit water primarily produces an overall redshift in the spectra compared to the one with implicit PCM model and the spectra with 26 and 45 water molecules overlap with each other. In contrast, we see large changes in the spectra obtained from PIGLET trajectory; upon inclusion of explicit water, there is not only a red shift in the spectra when explicit molecules are added but also a significant change in the broadening and the shape of the spectra is observed. Analogous to the BOMD spectra, here also we find the spectra computed with 45 and 26 water molecules are almost identical. This analysis suggests that one needs to do a careful convergence test of the number of explicit solvent molecules one should use when computing the absorption spectra of a molecule in solvent to correctly account for the hyperchromicity and bathochromic shifts observed in the experiments. We would also like to emphasize that these tests are particularly crucial when one wants to understand the NQE on the spectra.

A.3.0.3 Effect of "finite cluster" model on the absorption spectra

To compute the absorption spectra for each snapshot, we cut out geometries from the ground state molecular dynamics trajectory ("finite cluster" model) and perform TDDFT calculations. Recent studies by Isborn *et al.* (Reference [102]) showed that TDDFT calculations for solvated molecules using the above mentioned "finite cluster" model often results in spurious low lying charge transfer (between solvent and molecule) excitations due to the partial negative charge acquired by the water molecules at the edge of the solvation shell because of the abrupt breaking of the bonds between the water molecules during the snapshot curving process.

To understand this we have plotted the lowest energy excitation with respect to the number of water molecules using the B3LYP hybrid functional and the long-range corrected CAM-B3LYP functional as shown in Figure A.8. For the B3LYP functional (red dashed curve in Figure A.8 top panel) we find that the first excitation energy decreases rapidly with the addition of explicit water molecules. While with no water molecules the first excitation energy is about 3.24 eV, upon adding 50 water molecules it reduces by about 0.80 eV. A careful inspection of the wavefunctions of the electronic states involved in this

transition (i.e. HOMO and LUMO) shows that while the HOMO is localized on ellipticine, the LUMO is primarily localized on the outermost water molecules surrounding ellipticine resulting in spurious charge transfer excitations. This observation is similar to what is reported in Reference [102].

In contrast, with CAM-B3LYP we find that the shift in the lowest excitation peak position as a function of the number of water molecules is relatively small (about 0.09 eV, red dashed curve in Figure A.8(b)) compared to that with B3LYP. Inspection of the HOMO and LUMO of the "cluster" shows that while the former is localized on ellipticine, the later is on the water molecules at the edge. However, the electronic states involved in this transition are from HOMO to LUMO+1 or LUMO+2 or a combination of these (depending on the number of water molecules) are localized on ellipticine. Hence Cam-B3LYP is seen to correct the spurious low energy charge transfer excitation that is observed with B3LYP.

Isborne *et al.* (Ref. [102]) showed that this spurious charge transfer excitations can be related to the partial negative charge acquired by the water molecules at the edge of the solvation shell due to the abrupt breaking of the bonds between the water molecules during the snapshot curving process. To overcome this problem we have computed the absorption spectra including the PCM model in addition to the explicit water molecules. We find that on the inclusion of the PCM model, the LUMO is localized on the ellipticine for both the functionals and the TDDFT calculations show that the electronic states involved in the lowest energy excitation (π-$\pi*$ transition) is between the HOMO and the LUMO. For the B3LYP functional with the PCM model, we find that the lowest excitation energy changes only by about 0.07 eV upon adding 50 water molecules (black curve in Figure A.8 upper panel). Similarly, with Cam-B3LYP, the shift is about 0.06 eV upon adding the PCM model (black curve in Figure A.8 lower panel). Thus, our calculations suggest that the problem of spurious low energy charge transfer excitations can be circumvented by the inclusion of the PCM model. Hence we to compute the absorption spectra we have used the PCM model along with the explicit water molecules.

A.3.1 Results of the convergence test of the time-averaged spectra as a function of the number of snapshots

Figure A.9 shows the results of the convergence test of the time-averaged spectra of ellipticine in water as a function of the number of snapshots included. Each of the individual spectra is calculated with B3LYP functional. We find that we need to include at least 90 snapshots from our MD trajectory to get well-converged spectra. However, we have used 120 snapshots for consistency with other solvent molecules.

A.3.2 Effect of different exchange-correlation functionals on the absorption spectra:

Figure A.10 shows the dependence of the absorption spectra of ellipticine on the choice of exchange-correlation functionals. Among the different functionals considered in this study, we find that the spectra computed with CAM-B3LYP are blue-shifted compared to the ones computed with B3LYP, PBE0, and HSEH1PBE functionals. We find that though the absolute values of the peak positions depend on the choice of exchange-correlation functional, the overall shape of the spectra obtained from different exchange-correlation functionals are similar. Since the spectra calculated using B3LYP is in better agreement with the experimental one, we have used these spectra for all the discussions in Chapter 3.

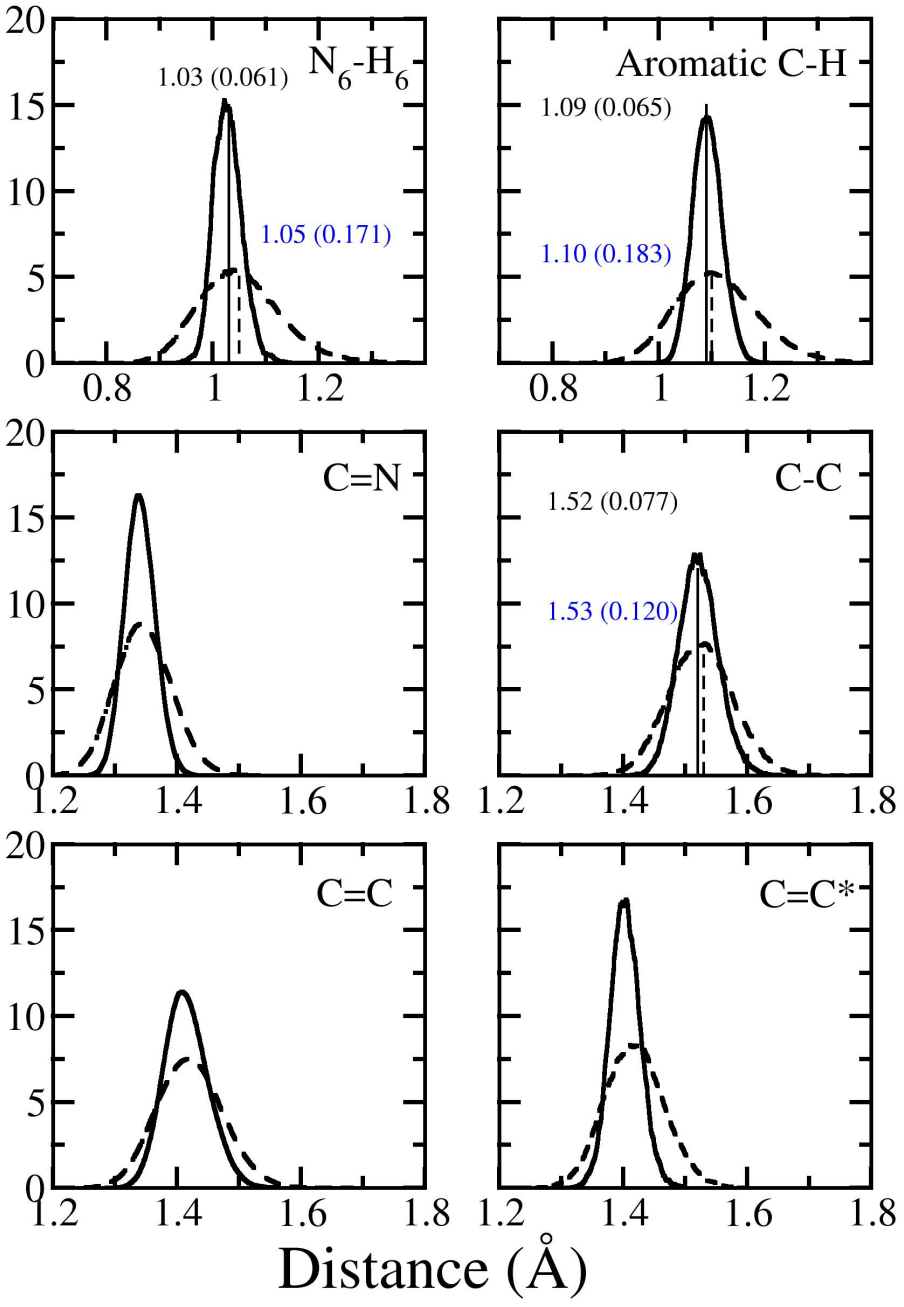

FIGURE A.6: The probability distribution function of N_6-H_6 and aromatic C-H bond lengths (quantum fluctuations causes asymmetric feature in PDF of PIGLET with light nuclei). FWHM is presented in brackets. The black solid line and black dashed line represent the PDFs of the bond length obtained from BOMD and PIGLET simulations respectively.The vertical line represents the equilibrium bond length in the gas phase geometry of EP.

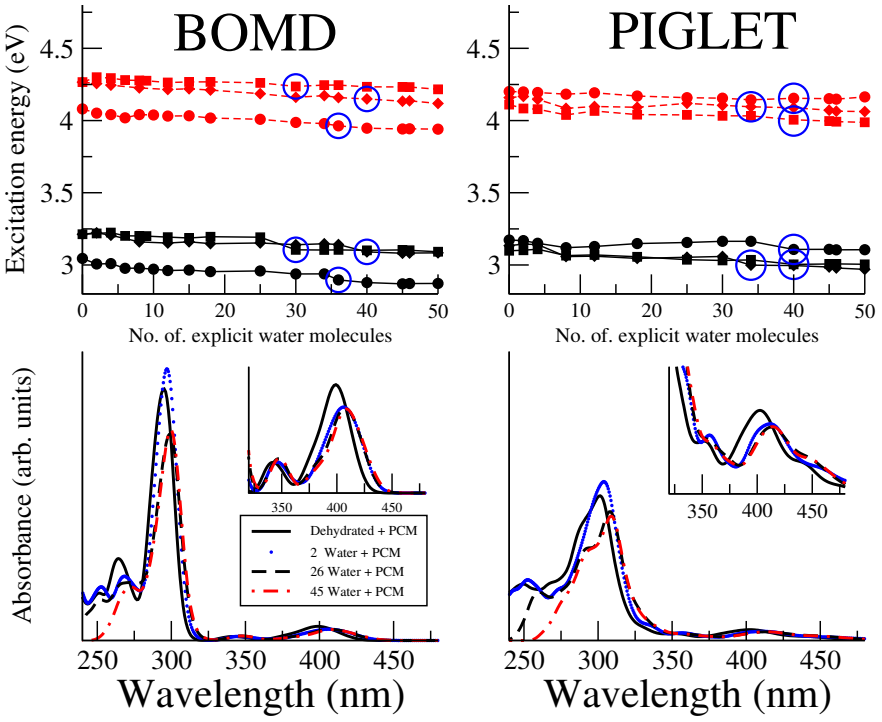

FIGURE A.7: Convergence of the peak positions as a function of a number of explicit water molecules of the absorption maxima and the lowest energy absorption peak for three randomly chosen snapshots from the BOMD trajectory (a) and PIGLET trajectory (b). (c) and (d) denote the time-averaged absorption spectra as a function of explicit water molecules with snapshots obtained from BOMD and PIGLET trajectories respectively. In (a) and (b), the red dashed lines and black solid lines denote the two absorption peaks while the filled circle, filled square and filled diamond denotes three different snapshots.

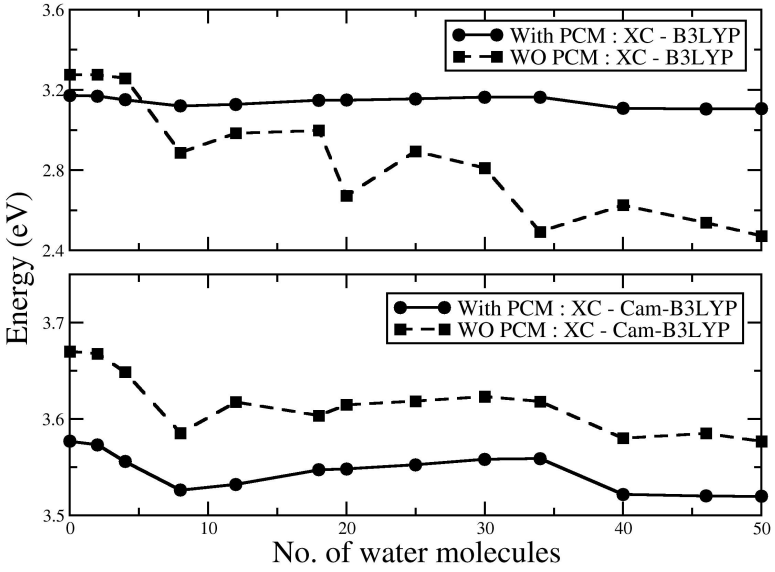

FIGURE A.8: Plot of lowest energy excitation as a function of the number of water molecules for a snapshot taken from the PIMD trajectory with the upper (lower) panel is B3LYP (long-range corrected CAM-B3LYP) exchange functional. The black solid curve is with PCM and the red dashed curve is without PCM.

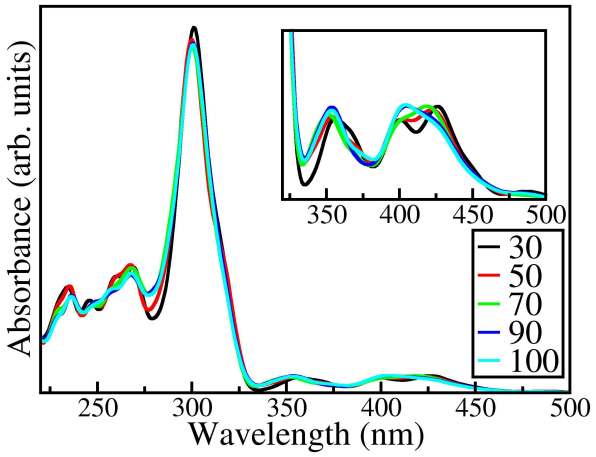

FIGURE A.9: The calculated time-averaged absorption spectrum as a function of the number of configurations. These random configurations are taken from the BOMD trajectory.

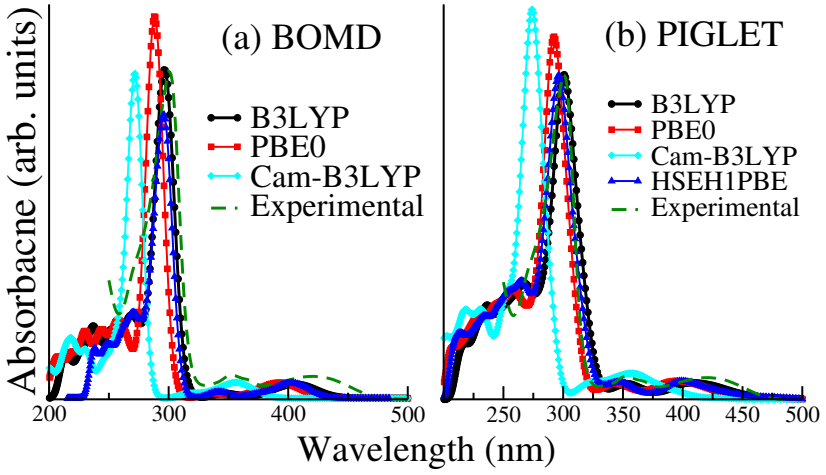

FIGURE A.10: The calculated time-averaged absorption spectrum as a function of exchange-functional.

A.4 Ellipticine in protic solvents

Figure A.11, A.12, A.13 shows convergence test for the number of explicit solvent molecules for methanol and ethylene glycol.

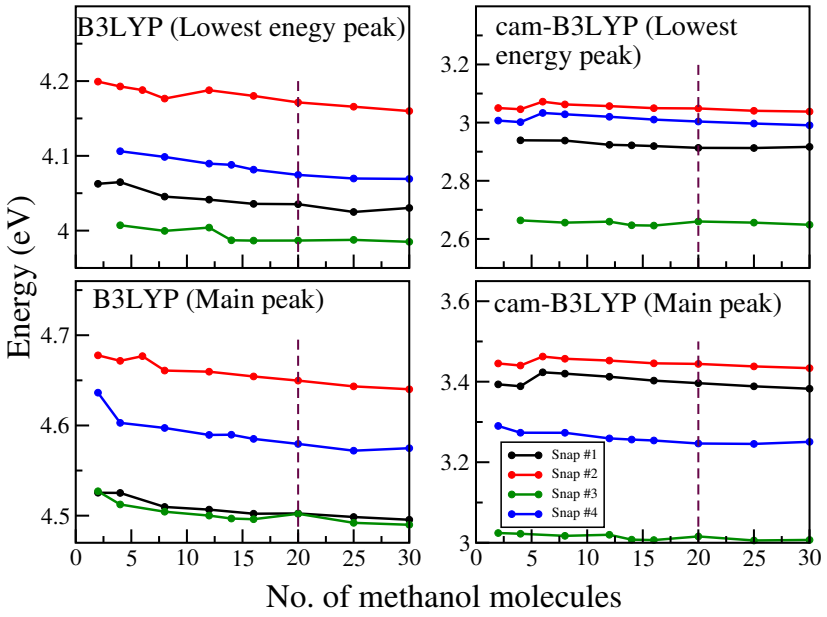

FIGURE A.11: Plot of lowest energy and maximum intensity excitation as a function of the number of methanol molecules for a snapshot taken from the PIMD trajectory with the upper (lower) panel is B3LYP (long-range corrected CAM-B3LYP) exchange functional.

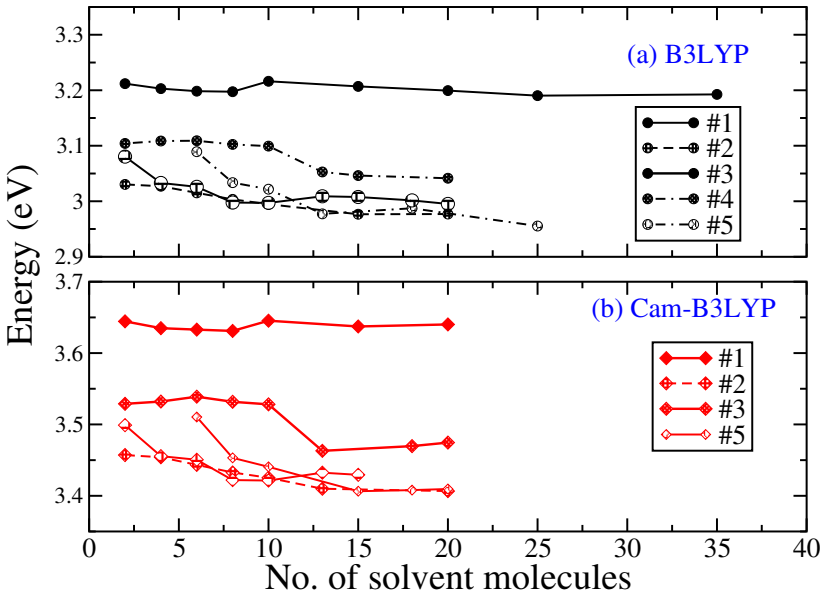

FIGURE A.12: Plot of lowest energy excitation as a function of the number of ethylene glycol molecules for a snapshot taken from the PIMD trajectory with the upper (lower) panel is B3LYP (long-range corrected CAM-B3LYP) exchange functional.

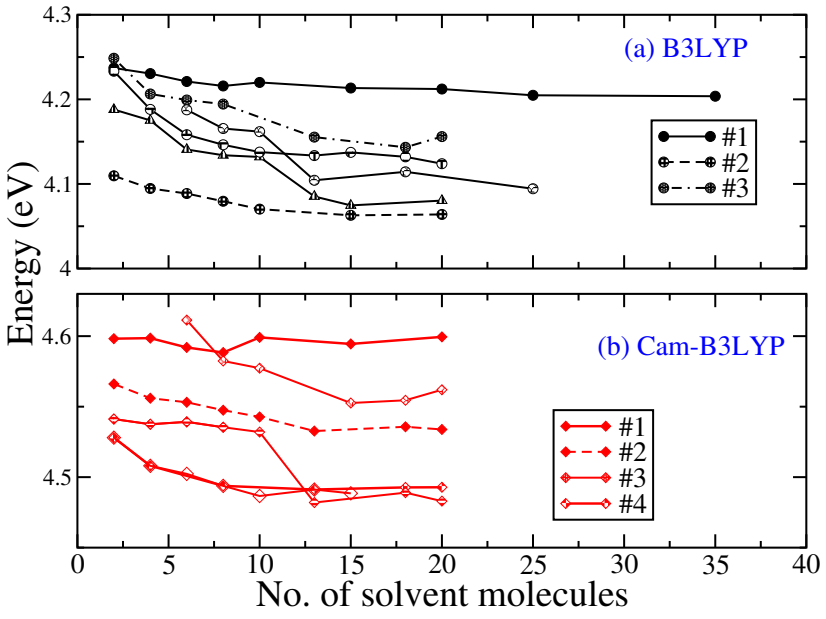

FIGURE A.13: Plot of maximum intensity excitation as a function of the number of ethylene glycol molecules for a snapshot taken from the PIMD trajectory with the upper (lower) panel is B3LYP (long-range corrected CAM-B3LYP) exchange functional.

Figure A.14 (Figure A.15) shows the contour plot of the joint probability distribution of the proton transfer coordinate υ_1 and υ_2 (υ_3) of a) water, b) methanol, and c) ethylene glycol obtained BOMD simulations. Similarly, figure A.16 shows the contour plot of the joint probability distribution of the proton transfer coordinate υ_2 and υ_4.

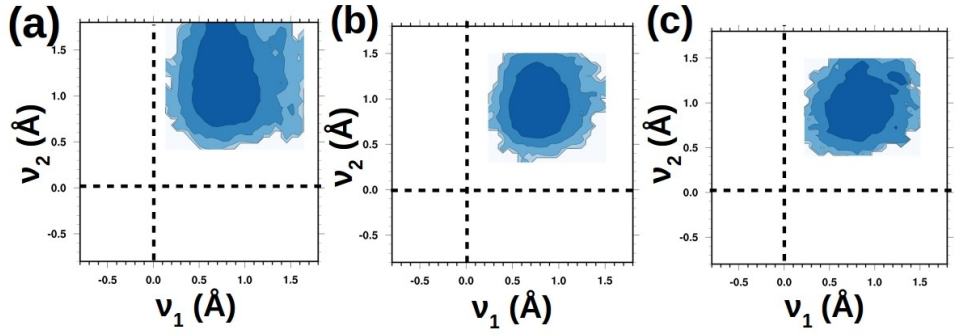

FIGURE A.14: Contour plot of the joint probability distribution of the proton transfer coordinate υ_1 and υ_2 of a) water, b) methanol, and c) ethylene glycol obtained from BOMD simulations

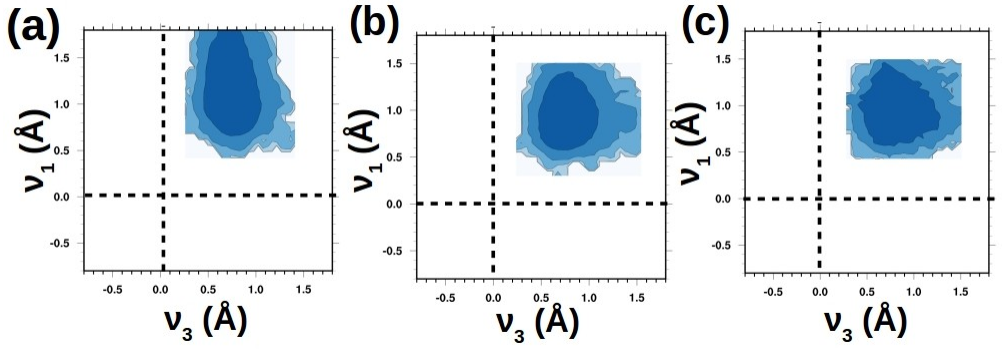

FIGURE A.15: Contour plot of the joint probability distribution of the proton transfer coordinate υ_1 and υ_3 of a) water, b) methanol, and c) ethylene glycol obtained from BOMD simulations

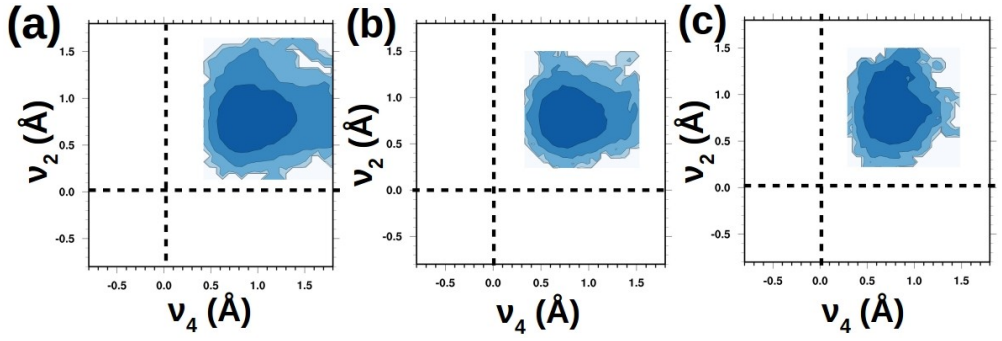

FIGURE A.16: Contour plot of the joint probability distribution of the proton transfer coordinate υ_2 and υ_4 of a) water, b) methanol, and c) ethylene glycol obtained from BOMD simulations

Appendix B

Appendix B

B.1 Lowest energy structure of the dye

The calculations of the different configurations of the dye in gas phase were done using the Gaussian Software [92]. We have used the PBE exchange-correlation functional and 6-311++G(d,p) basis set. Taking the lowest energy configuration obtained from this scan, we optimized it further with the Quantum ESPRESSO software [143] using the same exchange-correlation functional. For this, we have placed the molecule in a big box such that separation between the periodic images along the three different directions are 8 Å, 6 Å, and 16 Å along x, y, and z-axis respectively (the molecular plane is placed along XZ plane). We find that this is sufficient to avoid the spurious interactions between them. Further, we have used KE cutoff of 30 Ry and 350 Ry for the PW and charge density respectively. In order to determine the lowest energy structure of the 4ABBN in the gas phase we started with the planar structure and optimized its geometry. The optimized configuration is shown in Fig. 5.2 a). In this structure, the H of the -OH group forms an H bond with the N of the azo group, which stabilizes this molecule. However, the molecule can rotate about the dihedral angles $\angle C_1C_2N_1N_2$ and $\angle N_1N_2C_3C_4$, which are marked in figure 5.2 a).

For all the cases, we find that the planar starting configuration shown in Fig. 5.2 a) to be the lowest in energy. This gives us confidence that indeed the planar configuration shown in Fig. 5.2 a) corresponds to the global minima of 4ABBN in the gas phase.

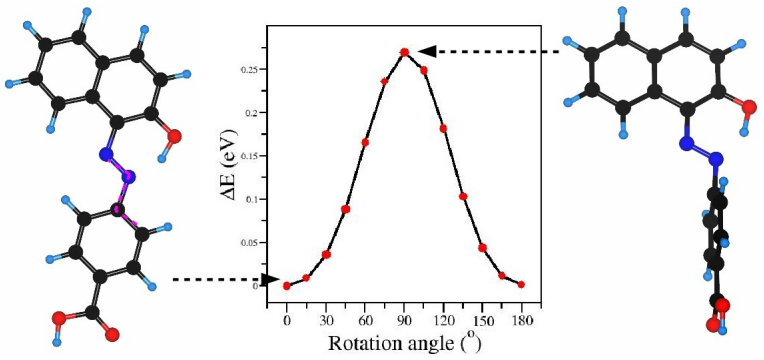

FIGURE B.1: Potential energy profile as a function of the $\angle C_1C_2N_1N_2$ dihedral angle as marked with magenta lines in the figure.

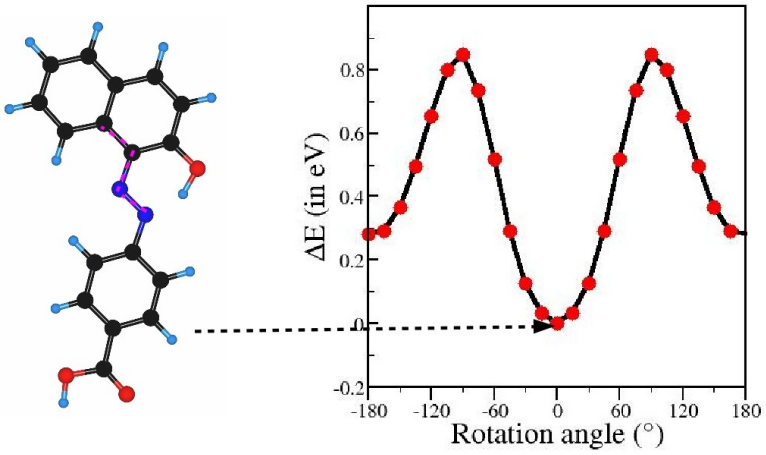

FIGURE B.2: Potential energy profile as a function of the $\angle N_1N_2C_3C_4$ dihedral angle as marked with magenta lines in the figure.

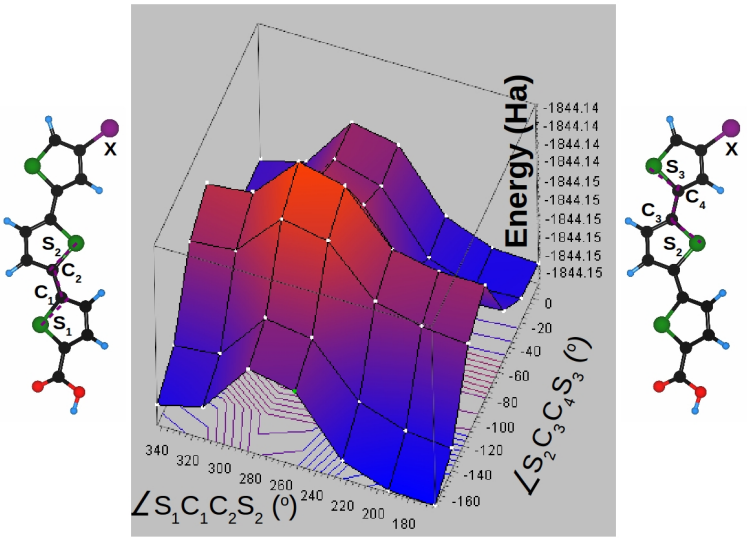

FIGURE B.3: Potential energy surface as a function of the $\angle S_1C_1C_2S_2$ and $\angle S_2C_3C_4S_3$ dihedral angles as marked with magenta lines in the figure.

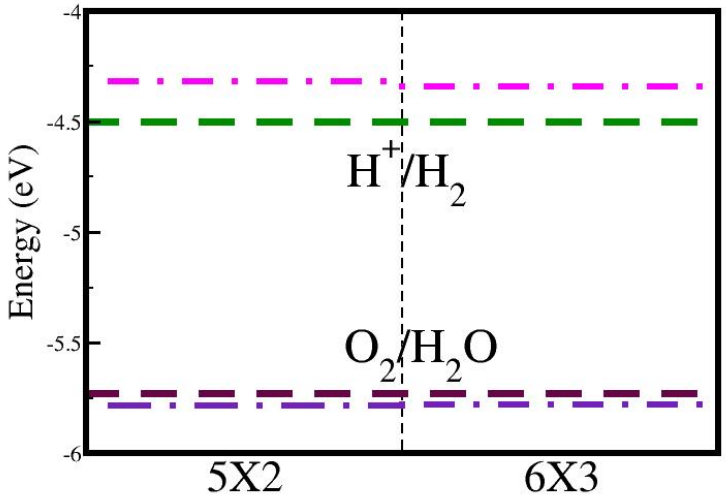

FIGURE B.4: Alignment of the redox potentials with respect to the valence band maximum (VBM) and the conduction band minimum (CBM) for (5×2) and (6×3) supercell of the composite system.

B.2 Test for convergence of supercell size

We have checked that using a (6×3) supercell, where the minimum distance between the periodic images of the molecule is about 15.5 Å, the results remain unchanged (See Figure B.4).

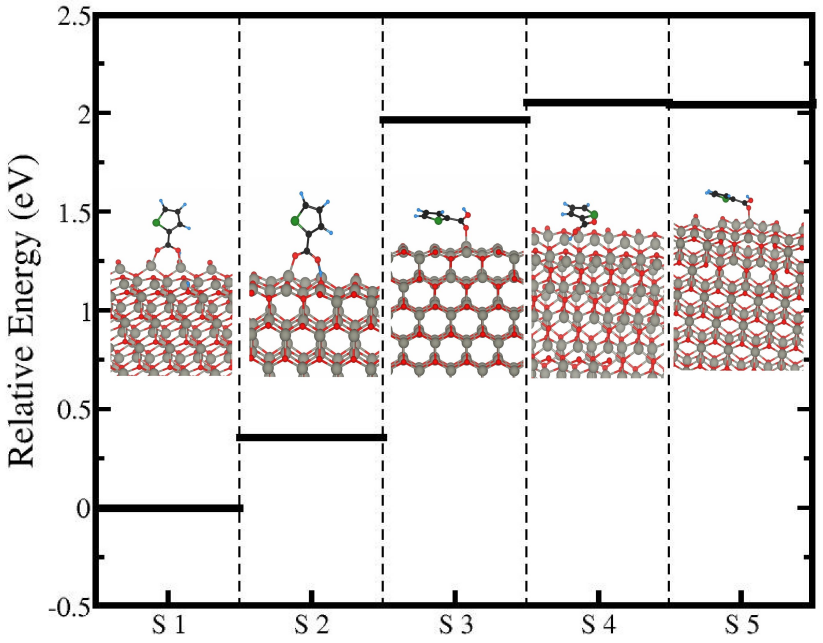

FIGURE B.5: Possible local minima dye orientations on ZnO $(10\bar{1}0)$ surface. The grey, red, black, cyan and dark green spheres represent Zn, O, C, H, and S atoms respectively.

B.3 Oligothiophenes

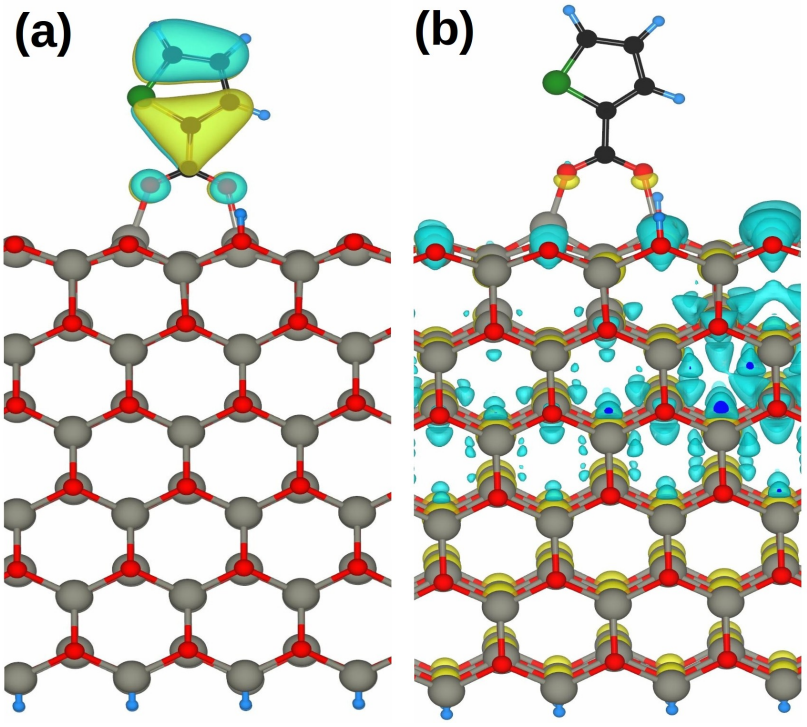

FIGURE B.6: a) HOMO and b) LUMO of thiophene-2-carboxylic acid (T_1) on ZnO ($10\bar{1}0$) slab.

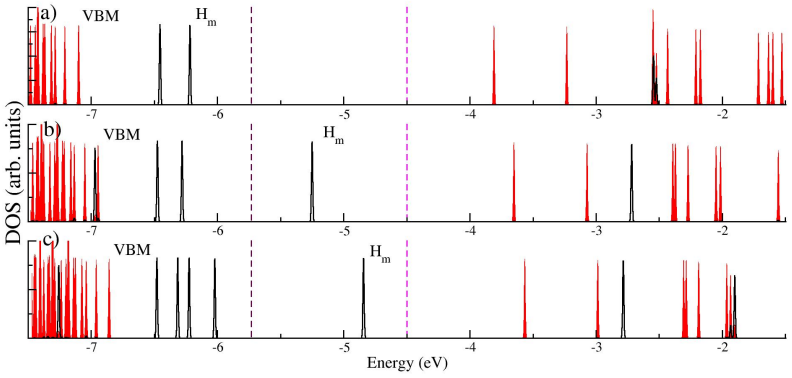

FIGURE B.7: DOS of the composite a) monomer (T_1), b) dimer (T_2), and c) trimer (T_3) unit on ZnO($10\bar{1}0$) surface. Projected contributions of ZnO substrate (red shaded area), and molecule (black line) are aligned with vacuum energy. H_m is the HOMO of the molecular level and VBM of ZnO is marked in the figure. The dashed brown and magenta lines mark the OP and RP.

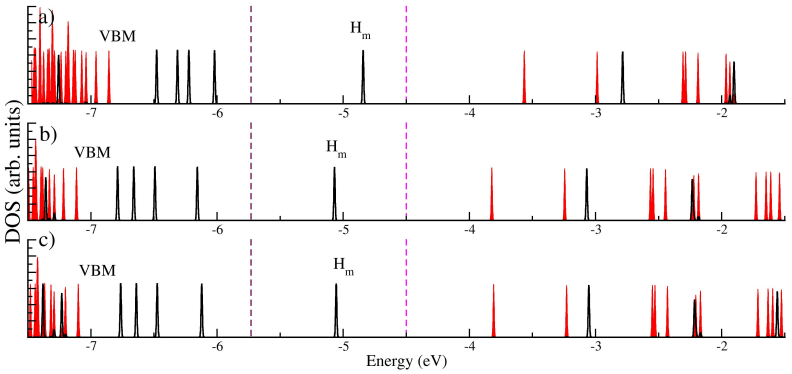

FIGURE B.8: DOS of the composite a) T_3, b) T_3-Cl, and c) T_3-Br unit on ZnO($10\bar{1}0$) surface. Projected contributions of ZnO substrate (red shaded area), and molecule (black line) are aligned with vacuum energy. H_m is the HOMO of the molecular level and VBM of ZnO is marked in the figure. The dashed brown and magenta lines mark the OP and RP.

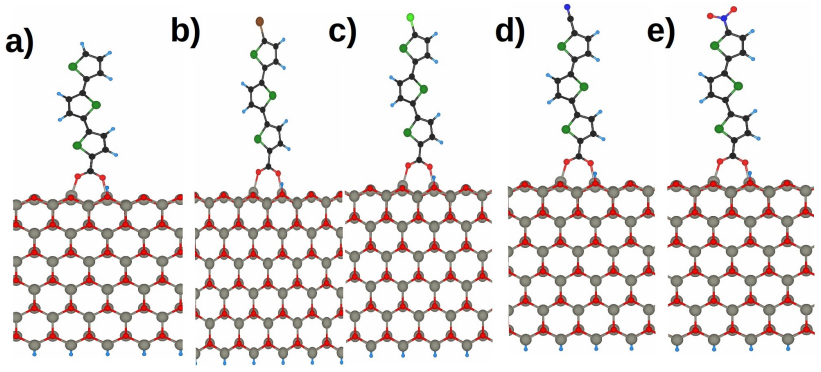

FIGURE B.9: Schematic diagram of relaxed oligo-thiophene-2-carboxylic acid (T_3) molecules with substitution group a) H, b) Br, c) Cl, d) CN, and e) NO_2. The grey, red, black, cyan, blue, brown, green, and dark green spheres represent Zn, O, C, H, N, Br, Cl, and S atoms respectively.

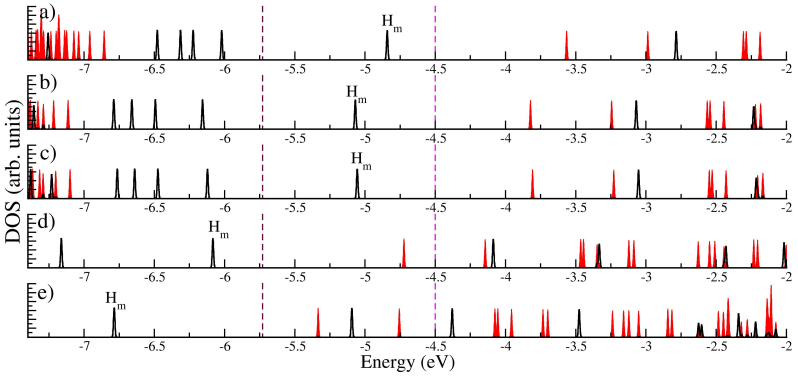

FIGURE B.10: Projected density of states (PDOS) of the ZnO ($10\bar{1}0$) in red and molecule a) T_3 , b) T_3-Cl, c) T_3-Br, d) T_3-CN, and e) T_3-NO_2 unit (in black line). Projected contributions of ZnO substrate (red shaded area), and molecule (black line) are aligned with vacuum energy. H_m is the HOMO of the molecular level and VBM of ZnO is marked in the figure. The dashed brown and magenta lines mark the OP and RP.

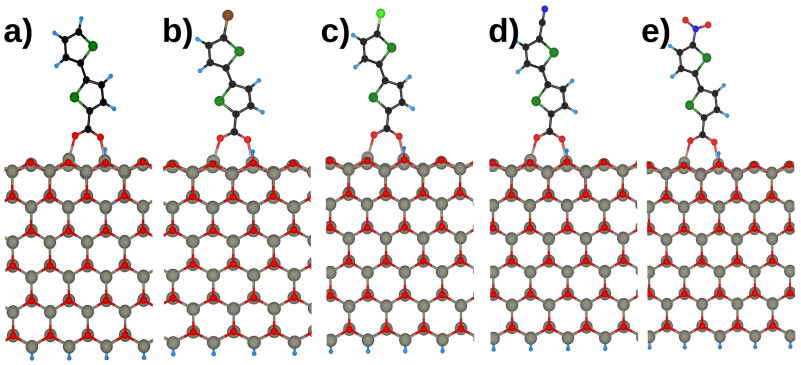

FIGURE B.11: Schematic diagram of relaxed oligo-thiophene (T_2) molecules with substitution group a) H, b) Br, c) Cl, d) CN, and e) NO_2.The grey, red, black, cyan, blue, brown, green, and dark green spheres represent Zn, O, C, H, N, Br, Cl, and S atoms respectively.

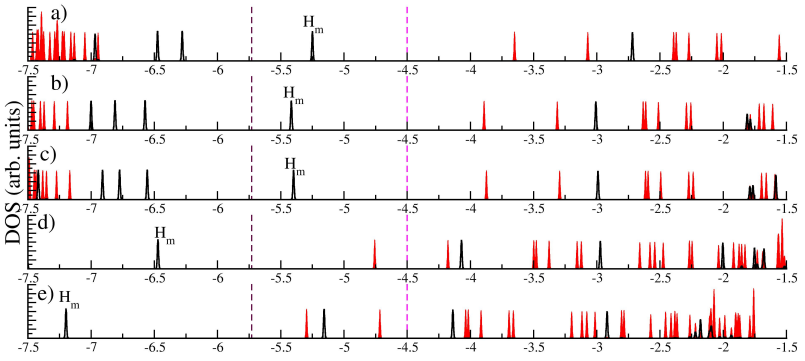

FIGURE B.12: PDOS of the ZnO $(10\bar{1}0)$ in red and molecule a) T_2 , b) T_2-Cl, c) T_2-Br, d) T_2-CN, and e) T_2-NO_2 unit (in black line). Projected contributions of ZnO substrate (red shaded area), and molecule (black line) are aligned with vacuum energy. H_m is the HOMO of the molecular level and VBM of ZnO is marked in the figure. The dashed brown and magenta lines mark the OP and RP.

Bibliography

[1] Tangui Le Bahers, Carlo Adamo, and Ilaria Ciofini. A qualitative index of spatial extent in charge-transfer excitations. *Journal of Chemical Theory and Computation*, 7(8):2498–2506, 2011. doi: 10.1021/ct200308m. URL https://doi.org/10.1021/ct200308m. PMID: 26606624.

[2] Luca Bertoluzzi, Pilar Lopez-Varo, Juan Antonio Jiménez Tejada, and Juan Bisquert. Charge transfer processes at the semiconductor/electrolyte interface for solar fuel production: insight from impedance spectroscopy. *J. Mater. Chem. A*, 4:2873–2879, 2016. doi: 10.1039/C5TA03210E. URL http://dx.doi.org/10.1039/C5TA03210E.

[3] Thomas E. Markland and Michele Ceriotti. Nuclear quantum effects enter the mainstream. *Nature Reviews Chemistry*, 2:0109 EP, Feb 2018. URL http://dx.doi.org/10.1038/s41570-017-0109. Review Article.

[4] Matthias Batzill. Fundamental aspects of surface engineering of transition metal oxide photocatalysts. *Energy Environ. Sci.*, 4:3275–3286, 2011. doi: 10.1039/C1EE01577J. URL http://dx.doi.org/10.1039/C1EE01577J.

[5] Krishna Gavvala, Abhigyan Sengupta, Raj Kumar Koninti, and Partha Hazra. Prototropical and photophysical properties of ellipticine inside the nanocavities of molecular containers. *Journal of Physical Chemistry B*, 117(45):14099–14107, 2013. doi: 10.1021/jp408280p. URL http://dx.doi.org/10.1021/jp408280p.

[6] Xiaohu Zhang, Tianyou Peng, and Shuaishuai Song. Recent advances in dye-sensitized semiconductor systems for photocatalytic hydrogen production. *J. Mater. Chem. A*, 4:2365–2402, 2016. doi: 10.1039/C5TA08939E. URL http://dx.doi.org/10.1039/C5TA08939E.

[7] Christian Reichardt. Solvatochromic dyes as solvent polarity indicators. *Chemical Reviews*, 94(8):2319–2358, 1994. doi: 10.1021/cr00032a005. URL https://doi.org/10.1021/cr00032a005.

[8] Judith P. Klinman and Amnon Kohen. Hydrogen tunneling links protein dynamics to enzyme catalysis. *Annu Rev Biochem*, 82:471–496, 2013. ISSN 1545-4509. doi: 10.1146/annurev-biochem-051710-133623. URL https://www.ncbi.nlm.nih.gov/pubmed/23746260. 23746260[pmid].

[9] Michael J. Knapp and Judith P. Klinman. Environmentally coupled hydrogen tunneling. *European Journal of Biochemistry*, 269(13):3113–3121, 2002. doi: 10.1046/j.1432-1033.2002.03022.x. URL https://febs.onlinelibrary.wiley.com/doi/abs/10.1046/j.1432-1033.2002.03022.x.

[10] Lu Wang, Stephen D. Fried, Steven G. Boxer, and Thomas E. Markland. Quantum delocalization of protons in the hydrogen-bond network of an enzyme active site. *Proceedings of the National Academy of Sciences*, 111(52):18454–18459, 2014. doi: 10.1073/pnas.1417923111.

[11] L. Wang, C.M. Isborn, and T.E. Markland. Chapter fifteen simulating nuclear and electronic quantum effects in enzymes. In Gregory A. Voth, editor, *Computational Approaches for Studying Enzyme Mechanism Part A*, volume 577 of *Methods in Enzymology*, pages 389 – 418. Academic Press, 2016. doi: https://doi.org/10.1016/bs.mie.2016.05.047. URL http://www.sciencedirect.com/science/article/pii/S0076687916300830.

[12] Miguel A. Morales, Jeffrey M. McMahon, Carlo Pierleoni, and David M. Ceperley. Nuclear quantum effects and nonlocal exchange-correlation functionals applied to liquid hydrogen at high pressure. *Phys. Rev. Lett.*, 110:065702, Feb 2013. doi: 10.1103/PhysRevLett.110.065702. URL https://link.aps.org/doi/10.1103/PhysRevLett.110.065702.

[13] Mariana Rossi, Piero Gasparotto, and Michele Ceriotti. Anharmonic and quantum fluctuations in molecular crystals: A first-principles study of the stability of paracetamol. *Phys. Rev. Lett.*, 117:115702, Sep 2016. doi: 10.1103/PhysRevLett.117.115702. URL https://link.aps.org/doi/10.1103/PhysRevLett.117.115702.

[14] Peter S. Zuev, Robert S. Sheridan, Titus V. Albu, Donald G. Truhlar, David A. Hrovat, and Weston Thatcher Borden. Carbon tunneling from a single quantum state. *Science*, 299(5608):867–870, 2003. ISSN 0036-8075. doi: 10.1126/science.1079294. URL http://science.sciencemag.org/content/299/5608/867.

[15] Michele Ceriotti, Giovanni Bussi, and Michele Parrinello. Nuclear quantum effects in solids using a colored-noise thermostat. *Phys. Rev. Lett.*, 103:030603, Jul 2009. doi: 10.1103/PhysRevLett.103.030603.

[16] Michele Ceriotti and David E. Manolopoulos. Efficient first-principles calculation of the quantum kinetic energy and momentum distribution of nuclei. *Phys. Rev. Lett.*, 109:100604, 2012. doi: 10.1103/PhysRevLett.109.100604.

[17] Michele Ceriotti, Joshua More, and David E. Manolopoulos. i-pi: A python interface for ab initio path integral molecular dynamics simulations. *Computer Physics Communications*, 185(3):1019 – 1026, 2014. ISSN 0010-4655. doi: http://dx.doi.org/10.1016/j.cpc.2013.10.027.

[18] Michele Ceriotti, Jérôme Cuny, Michele Parrinello, and David E. Manolopoulos. Nuclear quantum effects and hydrogen bond fluctuations in water. *Proceedings of the National Academy of Sciences*, 110(39):15591–15596, 2013. doi: 10.1073/pnas.1308560110.

[19] Michele Ceriotti, Wei Fang, Peter G. Kusalik, Ross H. McKenzie, Angelos Michaelides, Miguel A. Morales, and Thomas E. Markland. Nuclear quantum effects in water and aqueous systems: Experiment, theory, and current challenges. *Chemical Reviews*, 116(13):7529–7550, 2016. doi: 10.1021/acs.chemrev.5b00674.

[20] Oscar Khaselev and John A. Turner. A monolithic photovoltaic-photoelectrochemical device for hydrogen production via water splitting. *Science*, 280(5362):425–427, 1998. ISSN 0036-8075. doi: 10.1126/science.280.5362.425. URL http://science.sciencemag.org/content/280/5362/425.

[21] Takashi Hisatomi, Jun Kubota, and Kazunari Domen. Recent advances in semiconductors for photocatalytic and photoelectrochemical water splitting. *Chem. Soc. Rev.*, 43:7520–7535, 2014. doi: 10.1039/C3CS60378D. URL http://dx.doi.org/10.1039/C3CS60378D.

[22] Jin Mao, Kan Li, and Tianyou Peng. Recent advances in the photocatalytic co2 reduction over semiconductors. *Catal. Sci. Technol.*, 3:2481–2498, 2013. doi: 10.1039/C3CY00345K. URL http://dx.doi.org/10.1039/C3CY00345K.

[23] Damien Voiry, Hisato Yamaguchi, Junwen Li, Rafael Silva, Diego C. B. Alves, Takeshi Fujita, Mingwei Chen, Tewodros Asefa, Vivek B. Shenoy, Goki Eda, and Manish Chhowalla. Enhanced catalytic activity in strained chemically exfoliated ws2 nanosheets for hydrogen evolution. *Nature Materials*, 12:850 EP –, Jul 2013. URL https://doi.org/10.1038/nmat3700. Article.

[24] Jin-Xian Feng, Jin-Qi Wu, Ye-Xiang Tong, and Gao-Ren Li. Efficient hydrogen evolution on cu nanodots-decorated ni3s2 nanotubes by optimizing atomic hydrogen adsorption and desorption. *Journal of the American Chemical Society*, 140 (2):610–617, 2018. doi: 10.1021/jacs.7b08521. URL https://doi.org/10.1021/jacs.7b08521. PMID: 29058435.

[25] An-Liang Wang, Jing Lin, Han Xu, Ye-Xiang Tong, and Gao-Ren Li. Ni2p–cop hybrid nanosheet arrays supported on carbon cloth as an efficient flexible cathode for hydrogen evolution. *J. Mater. Chem. A*, 4:16992–16999, 2016. doi: 10.1039/C6TA07704H. URL http://dx.doi.org/10.1039/C6TA07704H.

[26] Zhe Zhang, Baoping Lu, Jinhui Hao, Wenshu Yang, and Jilin Tang. Fep nanoparticles grown on graphene sheets as highly active non-precious-metal electrocatalysts for hydrogen evolution reaction. *Chem. Commun.*, 50:11554–11557, 2014. doi: 10.1039/C4CC05285D. URL http://dx.doi.org/10.1039/C4CC05285D.

[27] Cheng Wan, Yagya N. Regmi, and Brian M. Leonard. Multiple phases of molybdenum carbide as electrocatalysts for the hydrogen evolution reaction. *Angewandte Chemie*, 126(25):6525–6528, 2014. doi: 10.1002/ange.201402998. URL https://onlinelibrary.wiley.com/doi/abs/10.1002/ange.201402998.

[28] Xiaodong Yan, Lihong Tian, Min He, and Xiaobo Chen. Three-dimensional crystalline/amorphous co/co3o4 core/shell nanosheets as efficient electrocatalysts for the hydrogen evolution reaction. *Nano Letters*, 15(9):6015–6021, Sep 2015. ISSN 1530-6984. doi: 10.1021/acs.nanolett.5b02205. URL https://doi.org/10.1021/acs.nanolett.5b02205.

[29] M. M. Ottakam Thotiyl, T. Ravikumar, and S. Sampath. Platinum particles supported on titanium nitride: an efficient electrode material for the oxidation of methanol in alkaline media. *J. Mater. Chem.*, 20:10643–10651, 2010. doi: 10.1039/C0JM01600D. URL http://dx.doi.org/10.1039/C0JM01600D.

[30] Brian O'Regan and Michael Grätzel. A low-cost, high-efficiency solar cell based on dye-sensitized colloidal tio2 films. *Nature*, 353:737 EP –, Oct 1991. URL http://dx.doi.org/10.1038/353737a0.

[31] U. Bach, D. Lupo, P. Comte, J. E. Moser, F. Weissörtel, J. Salbeck, H. Spreitzer, and M. Grätzel. Solid-state dye-sensitized mesoporous tio2 solar cells with high photon-to-electron conversion efficiencies. *Nature*, 395:583 EP –, Oct 1998. URL http://dx.doi.org/10.1038/26936.

[32] Michael Grätzel. Photoelectrochemical cells. *Nature*, 414:338 EP –, Nov 2001. URL http://dx.doi.org/10.1038/35104607.

[33] M. Grätzel. Photoelectrochemical solar energy conversion by dye sensitization. *AIP Conference Proceedings*, 404(1):119–127, 1997. doi: 10.1063/1.53471. URL https://aip.scitation.org/doi/abs/10.1063/1.53471.

[34] Dirac Paul Adrien Maurice and Fowler Ralph Howard. Quantum mechanics of many-electron systems. *Proceedings of the Royal Society of London. Series A, Containing Papers of a Mathematical and Physical Character*, 123(792):714–733, Apr 1929. doi: 10.1098/rspa.1929.0094. URL https://doi.org/10.1098/rspa.1929.0094.

[35] M. Born and R. Oppenheimer. Zur quantentheorie der molekeln. *Annalen der Physik*, 389(20):457–484, 1927. doi: 10.1002/andp.19273892002. URL https://onlinelibrary.wiley.com/doi/abs/10.1002/andp.19273892002.

[36] P. Hohenberg and W. Kohn. Inhomogeneous electron gas. *Phys. Rev.*, 136:B864–B871, Nov 1964. doi: 10.1103/PhysRev.136.B864. URL https://link.aps.org/doi/10.1103/PhysRev.136.B864.

[37] Dr Matt Probert. Electronic structure: Basic theory and practical methods, by richard m. martin. *Contemporary Physics*, 52(1):77–77, 2011. doi: 10.1080/00107514.2010.509989. URL https://doi.org/10.1080/00107514.2010.509989.

[38] John P. Perdew, Kieron Burke, and Matthias Ernzerhof. Generalized gradient approximation made simple. *Phys. Rev. Lett.*, 77:3865–3868, Oct 1996. doi: 10.1103/PhysRevLett.77.3865. URL https://link.aps.org/doi/10.1103/PhysRevLett.77.3865.

[39] Axel D. Becke. Densityfunctional thermochemistry the role of exact exchange. *Journal of Chemical Physics*, 98(7):5648–5652, 1993. doi: http://dx.doi.org/10.1063/1.464913.

[40] Chengteh Lee, Weitao Yang, and Robert G. Parr. Development of the colle-salvetti correlation-energy formula into a functional of the electron density. *Phys. Rev. B*, 37:785–789, Jan 1988. doi: 10.1103/PhysRevB.37.785.

[41] John P. Perdew, Matthias Ernzerhof, and Kieron Burke. Rationale for mixing exact exchange with density functional approximations. *Journal of Chemical Physics*, 105(22), 1996.

[42] Takeshi Yanai, David P Tew, and Nicholas C Handy. A new hybrid exchange–correlation functional using the coulomb-attenuating method (cam-b3lyp). *Chemical Physics Letters*, 393(1–3):51 – 57, 2004.

[43] Jochen Heyd, Gustavo E. Scuseria, and Matthias Ernzerhof. Hybrid functionals based on a screened coulomb potential. *The Journal of Chemical Physics*, 118(18): 8207–8215, 2003. doi: 10.1063/1.1564060. URL https://doi.org/10.1063/1.1564060.

[44] Denis Jacquemin, Eric A. Perpète, Giovanni Scalmani, Michael J. Frisch, Rika Kobayashi, and Carlo Adamo. Assessment of the efficiency of long-range corrected functionals for some properties of large compounds. *The Journal of Chemical Physics*, 126(14):144105, 2007.

[45] P. Pulay. Ab initio calculation of force constants and equilibrium geometries in polyatomic molecules. *Molecular Physics*, 17(2):197–204, 1969. doi: 10.1080/00268976900100941. URL https://doi.org/10.1080/00268976900100941.

[46] R. P. Feynman. Forces in molecules. *Phys. Rev.*, 56:340–343, Aug 1939. doi: 10.1103/PhysRev.56.340. URL https://link.aps.org/doi/10.1103/PhysRev.56.340.

[47] David Vanderbilt. Soft self-consistent pseudopotentials in a generalized eigenvalue formalism. *Phys. Rev. B*, 41:7892–7895, Apr 1990. doi: 10.1103/PhysRevB.41.7892. URL https://link.aps.org/doi/10.1103/PhysRevB.41.7892.

[48] Saman Alavi. Statistical mechanics: Theory and molecular simulation. *Angewandte Chemie International Edition*, 50(51):12138–12139, 2011. doi: 10.1002/anie.201105752. URL https://onlinelibrary.wiley.com/doi/abs/10.1002/anie.201105752.

[49] Michele Ceriotti, Michele Parrinello, Thomas E. Markland, and David E. Manolopoulos. Efficient stochastic thermostatting of path integral molecular dynamics. *The Journal of Chemical Physics*, 133(12):124104, 2010. doi: 10.1063/1.3489925. URL https://doi.org/10.1063/1.3489925.

[50] Michele Ceriotti, Giovanni Bussi, and Michele Parrinello. Colored-noise thermostats à la carte. *Journal of Chemical Theory and Computation*, 6(4):1170–1180, 2010. doi: 10.1021/ct900563s.

[51] Andreas Dreuw and Martin Head-Gordon. Failure of time-dependent density functional theory for long-range charge-transfer excited states the zincbacteriochlorin-bacteriochlorin and bacteriochlorophyll-spheroidene complexes. *Journal of the American Chemical Society*, 126(12):4007–4016, 2004. doi: 10.1021/ja039556n. URL https://doi.org/10.1021/ja039556n. PMID: 15038755.

[52] Maja Parac, Markus Doerr, Christel M. Marian, and Walter Thiel. Qm/mm calculation of solvent effects on absorption spectra of guanine. *Journal of Computational Chemistry*, 31(1):90–106. doi: 10.1002/jcc.21233. URL https://onlinelibrary.wiley.com/doi/abs/10.1002/jcc.21233.

[53] Filippo De Angelis, Simona Fantacci, and Ralph Gebauer. Simulating dye-sensitized tio2 heterointerfaces in explicit solvent: Absorption spectra, energy levels, and dye desorption. *The Journal of Physical Chemistry Letters*, 2(7):813–817, 2011. doi: 10.1021/jz200191u. URL https://doi.org/10.1021/jz200191u.

[54] Dario Rocca, Ralph Gebauer, Filippo De Angelis, Mohammad K. Nazeeruddin, and Stefano Baroni. Time-dependent density functional theory study of squaraine dye-sensitized solar cells. *Chemical Physics Letters*, 475(1):49 – 53, 2009. ISSN

0009-2614. doi: https://doi.org/10.1016/j.cplett.2009.05.019. URL http://www.sciencedirect.com/science/article/pii/S0009261409005624.

[55] Paul Hessler, Jang Park, and Kieron Burke. Several theorems in time-dependent density functional theory. *Phys. Rev. Lett.*, 82:378–381, Jan 1999. doi: 10.1103/PhysRevLett.82.378. URL https://link.aps.org/doi/10.1103/PhysRevLett.82.378.

[56] Tie-cheng Li and Pei-qing Tong. Hohenberg-kohn theorem for time-dependent ensembles. *Phys. Rev. A*, 31:1950–1951, Mar 1985. doi: 10.1103/PhysRevA.31.1950. URL https://link.aps.org/doi/10.1103/PhysRevA.31.1950.

[57] Erich Runge and E. K. U. Gross. Density-functional theory for time-dependent systems. *Phys. Rev. Lett.*, 52:997–1000, Mar 1984. doi: 10.1103/PhysRevLett.52.997. URL https://link.aps.org/doi/10.1103/PhysRevLett.52.997.

[58] G Mathé, E Chenu, C Bourut, and S Orbach-Arbouys. The in vivo effect of ellipticine analogues on the blood concentration of friend virus: a murine model for studying anti-hiv drugs. *Biomedicine pharmacotherapy and Biomedecine pharmacotherapie*, 47(10):457–460, 1993. ISSN 0753-3322.

[59] Li Ding, Jan Balzarini, Dominique Schols, Bernard Meunier, and Erik De Clercq. Anti-human immunodeficiency virus effects of cationic metalloporphyrin-ellipticine complexes. *Biochemical Pharmacology*, 44(8):1675 – 1679, 1992. ISSN 0006-2952. doi: http://dx.doi.org/10.1016/0006-2952(92)90486-3.

[60] Marie Stiborova and Eva Frei. Ellipticines as dna-targeted chemotherapeutics. *Current Medicinal Chemistry*, 21(5):575–591, 2014.

[61] Nichola C. Garbett and David E. Graves. Extending natures leads: The anticancer agent ellipticine. *Current Medicinal Chemistry-Anti-Cancer Agents*, 4(2):149–172, 2004. ISSN 1568-0118.

[62] Leslie M. Werbel, Mario Angelo, David W. Fry, and Donald F. Worth. Basically substituted ellipticine analogs as potential antitumor agents. *Journal of Medicinal Chemistry*, 29(7):1321–1322, 1986. doi: 10.1021/jm00157a040.

[63] G Mathé, K Triana, P Pontiggia, D Blanquet, M Hallard, and C Morette. Data of pre-clinical and early clinical trials of acriflavine and hydroxy-methyl-ellipticine

reviewed, enriched by the experience of their use for 18 months to 6 years in combinations with other hiv1 virostatics. *Biomedicine and Pharmacotherapy*, 52(9): 391 – 396, 1998. ISSN 0753-3322. doi: http://dx.doi.org/10.1016/S0753-3322(99)80007-9.

[64] Raj Kumar Koninti, Abhigyan Sengupta, Krishna Gavvala, Nirmalya Ballav, and Partha Hazra. Loading of an anti-cancer drug onto graphene oxide and subsequent release to dna/rna: a direct optical detection. *Nanoscale*, 6:2937–2944, 2014. doi: 10.1039/C3NR06081K. URL http://dx.doi.org/10.1039/C3NR06081K.

[65] Krishna Gavvala, Raj Kumar Koninti, Abhigyan Sengupta, and Partha Hazra. Excited state proton transfer dynamics of an eminent anticancer drug, ellipticine, in octyl glucoside micelle. *Phys. Chem. Chem. Phys.*, 16:14953–14960, 2014. doi: 10.1039/C4CP01783H.

[66] Ferenc Zsila. The anticancer agent ellipticine binds to glycosaminoglycans at mildly acidic ph characteristic of the extracellular matrix of tumor tissues. *RSC Adv.*, 6:810–814, 2016. doi: 10.1039/C5RA23437A.

[67] Albert Clarysse, Antonio Brugarolas, Pierre Siegenthaler, Reto Abele, Franco Cavalli, Robert de Jager, Georgette Renard, Marcel Rozencweig, and Heine H. Hansen. Phase ii study of 9-hydroxy-2¡em¿n¡/em¿-methylellipticinium acetate. *European Journal of Cancer*, 20(2):243–247, 1984. ISSN 0959-8049. doi: 10.1016/0277-5379(84)90190-1.

[68] P. Dodion, M. Rozencweig, C. Nicaise, M. Piccart, E. Cumps, N. Crespeigne, D. Kisner, and Y. Kenis. Phase i clinical study of 9-hydroxy-2¡em¿n¡/em¿-methyl-ellipticinium acetate (nsc-264137) administered on a 5-day i.v. schedule. *European Journal of Cancer*, 18(6):519–522, 1982. ISSN 0959-8049. doi: 10.1016/0277-5379(82)90220-6.

[69] T.W Moody, G Czerwinski, N.I Tarasova, and C.J Michejda. Vip-ellipticine derivatives inhibit the growth of breast cancer cells. *Life Sciences*, 71(9):1005–1014, 2002. ISSN 0024-3205. doi: http://dx.doi.org/10.1016/S0024-3205(02)01741-1.

[70] Shan Yu Fung, Hong Yang, Priya T. Bhola, Parisa Sadatmousavi, Edward Muzar, Mingyao Liu, and P. Chen. Self-assembling peptide as a potential carrier for

hydrophobic anticancer drug ellipticine: Complexation, release and in vitro delivery. *Advanced Functional Materials*, 19(1):74–83, 2009. ISSN 1616-3028. doi: 10.1002/adfm.200800860. URL http://dx.doi.org/10.1002/adfm.200800860.

[71] Grzegorz Czerwinski, Nadya I. Tarasova, and Christopher J. Michejda. Cytotoxic agents directed to peptide hormone receptors: Defining the requirements for a successful drug. *Proceedings of the National Academy of Sciences*, 95(20):11520–11525, 1998. doi: 10.1073/pnas.95.20.11520.

[72] M. Sbai, S.Ait Lyazidi, D.A. Lerner, B. del Castillo, and M.A. Martin. Papers presented at the sixth international symposium on luminescence spectrometry in biomedical analysis. detection techniques and applications in chromatography and capillary electrophoresis modified β-cylclodextrins as enhancers of fluorescence emission of carbazole alkaloid derivatives. *Analytica Chimica Acta*, 303(1):47 – 55, 1995. ISSN 0003-2670. doi: http://dx.doi.org/10.1016/0003-2670(94)00475-2.

[73] S. Y. Fung, J. Duhamel, and P. Chen. Solvent effect on the photophysical properties of the anticancer agent ellipticine. *Journal of Physical Chemistry A*, 110(40): 11446–11454, 2006. doi: 10.1021/jp062778y.

[74] M. Sbai, S. Ait Lyazidi, D.A. Lerner, B. del Castillo, and M.A. Martin. Use of micellar media for the fluorimetric determination of ellipticine in aqueous solutions. *Journal of Pharmaceutical and Biomedical Analysis*, 14(8):959 – 965, 1996. ISSN 0731-7085. doi: http://dx.doi.org/10.1016/S0731-7085(96)01759-1.

[75] Zsombor Miskolczy, László Biczók, and István Jablonkai. Effect of hydroxylic compounds on the photophysical properties of ellipticine and its 6-methyl derivative: The origin of dual fluorescence. *Chemical Physics Letters*, 427(1–3):76 – 81, 2006. doi: http://dx.doi.org/10.1016/j.cplett.2006.06.045.

[76] Sanghamitra Banerjee, Ashok Pabbathi, M. Chandra Sekhar, and Anunay Samanta. Dual fluorescence of ellipticine: Excited state proton transfer from solvent versus solvent mediated intramolecular proton transfer. *Journal of Physical Chemistry A*, 115(33):9217–9225, 2011. doi: 10.1021/jp206232b.

[77] F. Sureau, F. Moreau, J. M. Millot, M. Manfait, B. Allard, J. Aubard, and M. A. Schwaller. Microspectrofluorometry of the protonation state of ellipticine, an antitumor alkaloid, in single cells. *Biophysical Journal*, 65(5):1767–1774, 1993. ISSN 0006-3495. doi: 10.1016/S0006-3495(93)81273-6.

[78] Wei Fang, Ji Chen, Mariana Rossi, Yexin Feng, Xin-Zheng Li, and Angelos Michaelides. Inverse temperature dependence of nuclear quantum effects in dna base pairs. *The Journal of Physical Chemistry Letters*, 7(11):2125–2131, 2016. doi: 10.1021/acs.jpclett.6b00777.

[79] Mariana Rossi, Wei Fang, and Angelos Michaelides. Stability of complex biomolecular structures: van der waals, hydrogen bond cooperativity, and nuclear quantum effects. *The Journal of Physical Chemistry Letters*, 6(21):4233–4238, 2015. doi: 10.1021/acs.jpclett.5b01899.

[80] Barbara Michela Giuliano, Igor Reva, Leszek Lapinski, and Rui Fausto. Infrared spectra and ultraviolet-tunable laser induced photochemistry of matrix-isolated phenol and phenol-d5. *Journal of Chemical Physics*, 136(2):024505, 2012.

[81] Federico Giberti, Ali A. Hassanali, Michele Ceriotti, and Michele Parrinello. The role of quantum effects on structural and electronic fluctuations in neat and charged water. *Journal of Physical Chemistry B*, 118(46):13226–13235, 2014. doi: 10.1021/jp507752e.

[82] Mario Barbatti, Adelia J. A. Aquino, and Hans Lischka. The uv absorption of nucleobases: semi-classical ab initio spectra simulations. *Phys. Chem. Chem. Phys.*, 12:4959–4967, 2010. doi: 10.1039/B924956G.

[83] Fabio Della Sala, Roger Rousseau, Andreas Gorling, and Dominik Marx. Quantum and thermal fluctuation effects on the photoabsorption spectra of clusters. *Phys. Rev. Lett.*, 92:183401, 2004. doi: 10.1103/PhysRevLett.92.183401.

[84] Yu Kay Law and Ali A. Hassanali. Role of quantum vibrations on the structural, electronic, and optical properties of 9-methylguanine. *Journal of Physical Chemistry A*, 119(44):10816–10827, 2015. doi: 10.1021/acs.jpca.5b07022.

[85] Dorothea Pinotsi, Luca Grisanti, Pierre Mahou, Ralph Gebauer, Clemens F. Kaminski, Ali Hassanali, and Gabriele S. Kaminski Schierle. Proton transfer and

structure-specific fluorescence in hydrogen bond-rich protein structures. *Journal of the American Chemical Society*, 138(9):3046–3057, 2016. doi: 10.1021/jacs.5b11012.

[86] Luke M. Oltrogge and Steven G. Boxer. Short hydrogen bonds and proton delocalization in green fluorescent protein (gfp). *ACS Central Science*, 1(3):148–156, 2015. doi: 10.1021/acscentsci.5b00160.

[87] Xin-Zheng Li, Brent Walker, and Angelos Michaelides. Quantum nature of the hydrogen bond. *Proceedings of the National Academy of Sciences*, 108(16):6369–6373, 2011. doi: 10.1073/pnas.1016653108.

[88] Ross H. McKenzie, Christiaan Bekker, Bijyalaxmi Athokpam, and Sai G. Ramesh. Effect of quantum nuclear motion on hydrogen bonding. *The Journal of Chemical Physics*, 140(17):174508, 2014. doi: 10.1063/1.4873352. URL https://doi.org/10.1063/1.4873352.

[89] William L. Jorgensen. Quantum and statistical mechanical studies of liquids. 10. transferable intermolecular potential functions for water, alcohols, and ethers. application to liquid water. *Journal of the American Chemical Society*, 103(2):335–340, 1981. doi: 10.1021/ja00392a016.

[90] Junmei Wang, Romain M. Wolf, James W. Caldwell, Peter A. Kollman, and David A. Case. Development and testing of a general amber force field. *Journal of Computational Chemistry*, 25(9):1157–1174, 2004. doi: 10.1002/jcc.20035.

[91] Brent H. Besler, Kenneth M. Merz, and Peter A. Kollman. Atomic charges derived from semiempirical methods. *Journal of Computational Chemistry*, 11(4):431–439, 1990. doi: 10.1002/jcc.540110404.

[92] M. J. Frisch, G. W. Trucks, H. B. Schlegel, G. E. Scuseria, M. A. Robb, J. R. Cheeseman, G. Scalmani, V. Barone, B. Mennucci, G. A. Petersson, H. Nakatsuji, M. Caricato, X. Li, H. P. Hratchian, A. F. Izmaylov, J. Bloino, G. Zheng, J. L. Sonnenberg, M. Hada, M. Ehara, K. Toyota, R. Fukuda, J. Hasegawa, M. Ishida, T. Nakajima, Y. Honda, O. Kitao, H. Nakai, T. Vreven, J. A. Montgomery, Jr., J. E. Peralta, F. Ogliaro, M. Bearpark, J. J. Heyd, E. Brothers, K. N. Kudin, V. N. Staroverov, R. Kobayashi, J. Normand, K. Raghavachari, A. Rendell, J. C. Burant, S. S. Iyengar, J. Tomasi, M. Cossi, N. Rega, J. M. Millam, M. Klene,

J. E. Knox, J. B. Cross, V. Bakken, C. Adamo, J. Jaramillo, R. Gomperts, R. E. Stratmann, O. Yazyev, A. J. Austin, R. Cammi, C. Pomelli, J. W. Ochterski, R. L. Martin, K. Morokuma, V. G. Zakrzewski, G. A. Voth, P. Salvador, J. J. Dannenberg, S. Dapprich, A. D. Daniels, Ö. Farkas, J. B. Foresman, J. V. Ortiz, J. Cioslowski, and D. J. Fox. Gaussian09 revision d.01.

[93] David A. Case, Thomas E. Cheatham, Tom Darden, Holger Gohlke, Ray Luo, Kenneth M. Merz, Alexey Onufriev, Carlos Simmerling, Bing Wang, and Robert J. Woods. The amber biomolecular simulation programs. *Journal of Computational Chemistry*, 26(16):1668–1688, 2005. doi: 10.1002/jcc.20290.

[94] Wendy D. Cornell, Piotr Cieplak, Christopher I. Bayly, and Peter A. Kollmann. Application of resp charges to calculate conformational energies, hydrogen bond energies, and free energies of solvation. *Journal of the American Chemical Society*, 115(21):9620–9631, 1993. doi: 10.1021/ja00074a030.

[95] Eric J. Sorin and Vijay S. Pande. Exploring the helix-coil transition via all-atom equilibrium ensemble simulations. *Biophysical Journal*, 88(4):2472 – 2493, 2005. doi: http://dx.doi.org/10.1529/biophysj.104.051938.

[96] H. J. C. Berendsen, J. P. M. Postma, W. F. van Gunsteren, A. DiNola, and J. R. Haak. Molecular dynamics with coupling to an external bath. *Journal of Chemical Physics*, 81(8):3684–3690, 1984. doi: http://dx.doi.org/10.1063/1.448118.

[97] Berk Hess, Henk Bekker, Herman J. C. Berendsen, and Johannes G. E. M. Fraaije. Lincs: A linear constraint solver for molecular simulations. *Journal of Computational Chemistry*, 18(12):1463–1472. doi: 10.1002/(SICI)1096-987X(199709)18:12⟨1463::AID-JCC4⟩3.0.CO;2-H. URL https://onlinelibrary.wiley.com/doi/abs/10.1002/%28SICI%291096-987X%28199709%2918%3A12%3C1463%3A%3AAID-JCC4%3E3.0.CO%3B2-H.

[98] Joost VandeVondele, Matthias Krack, Fawzi Mohamed, Michele Parrinello, Thomas Chassaing, and Jürg Hutter. Quickstep: Fast and accurate density functional calculations using a mixed gaussian and plane waves approach. *Computer Physics Communications*, 167(2):103 – 128, 2005. doi: http://dx.doi.org/10.1016/j.cpc.2004.12.014.

[99] G. Kresse and J. Furthmuller. Efficient iterative schemes for *ab initio* total-energy calculations using a plane-wave basis set. *Phys. Rev. B*, 54:11169–11186, Oct 1996. doi: 10.1103/PhysRevB.54.11169.

[100] Daniel W. Silverstein and Lasse Jensen. Assessment of the accuracy of long-range corrected functionals for describing the electronic and optical properties of silver clusters. *Journal of Chemical Physics*, 132(19):194302, 2010.

[101] Giovanni Bussi, Davide Donadio, and Michele Parrinello. Canonical sampling through velocity rescaling. *Journal of Chemical Physics*, 126(1):–, 2007. doi: http://dx.doi.org/10.1063/1.2408420.

[102] Christine M. Isborn, Brendan D. Mar, Basile F. E. Curchod, Ivano Tavernelli, and Todd J. Martínez. The charge transfer problem in density functional theory calculations of aqueously solvated molecules. *The Journal of Physical Chemistry B*, 117(40):12189–12201, 2013. doi: 10.1021/jp4058274.

[103] Claudia Filippi, Maurizio Zaccheddu, and Francesco Buda. Absorption spectrum of the green fluorescent protein chromophore: A difficult case for ab initio methods? *Journal of Chemical Theory and Computation*, 5(8):2074–2087, 2009. doi: 10.1021/ct900227j.

[104] Thomas M. Henderson, Artur F. Izmaylov, Giovanni Scalmani, and Gustavo E. Scuseria. Can short-range hybrids describe long-range-dependent properties? *Journal of Chemical Physics*, 131(4):–, 2009.

[105] Giovanni Scalmani and Michael J. Frisch. Continuous surface charge polarizable continuum models of solvation. i. general formalism. *Journal of Chemical Physics*, 132(11), 2010.

[106] Michael J. Tubergen, Anne M. Andrews, and Robert L. Kuczkowski. Microwave spectrum and structure of a hydrogen-bonded pyrrole-water complex. *Journal of Physical Chemistry*, 97(29):7451–7457, 1993. doi: 10.1021/j100131a011.

[107] Ann M. Schmiedekamp, Igor A. Topol, and Christopher J. Michejda. Proton affinities of molecules containing nitrogen and oxygen: Comparing density functional results to experiment. *Theoretica chimica acta*, 92(2):83–96, 1995. ISSN 1432-2234. doi: 10.1007/BF01134215.

[108] Erlend R. M. Davidson, Jiří Klimeš, Dario Alfè, and Angelos Michaelides. Cooperative interplay of van der waals forces and quantum nuclear effects on adsorption: H at graphene and at coronene. *ACS Nano*, 8(10):9905–9913, 2014. doi: 10.1021/nn505578x.

[109] Mats Ormö, Andrew B. Cubitt, Karen Kallio, Larry A. Gross, Roger Y. Tsien, and S. James Remington. Crystal structure of the aequorea victoria green fluorescent protein. *Science*, 273(5280):1392–1395, 1996. ISSN 0036-8075. doi: 10.1126/science.273.5280.1392. URL http://science.sciencemag.org/content/273/5280/1392.

[110] Shigeo Yamaguchi, Hironari Kamikubo, Kazuo Kurihara, Ryota Kuroki, Nobuo Niimura, Nobutaka Shimizu, Yoichi Yamazaki, and Mikio Kataoka. Low-barrier hydrogen bond in photoactive yellow protein. *Proceedings of the National Academy of Sciences*, 106(2):440–444, 2009. ISSN 0027-8424. doi: 10.1073/pnas.0811882106. URL http://www.pnas.org/content/106/2/440.

[111] Nathalia S. V. Barbosa, Yong Zhang, Eduardo R. A. Lima, Frederico W. Tavares, and Edward J. Maginn. Development of an amber-compatible transferable force field for poly(ethylene glycol) ethers (glymes). *Journal of Molecular Modeling*, 23(6):194, May 2017. ISSN 0948-5023. doi: 10.1007/s00894-017-3355-3. URL https://doi.org/10.1007/s00894-017-3355-3.

[112] Kalju Kahn and Thomas C. Bruice. Parameterization of opls-aa force field for the conformational analysis of macrocyclic polyketides. *Journal of Computational Chemistry*, 23(10):977–996, 2002. doi: 10.1002/jcc.10051. URL https://onlinelibrary.wiley.com/doi/abs/10.1002/jcc.10051.

[113] Yang Zhong and Sandeep Patel. Nonadditive empirical force fields for short-chain linear alcohols: Methanol to butanol. hydration free energetics and kirkwood-buff analysis using charge equilibration models. *The Journal of Physical Chemistry B*, 114(34):11076–11092, Sep 2010. ISSN 1520-6106. doi: 10.1021/jp101597r. URL https://doi.org/10.1021/jp101597r.

[114] Thomas Steiner Gautam R. Desiraju. *The Weak Hydrogen Bond: In Structural Chemistry and Biology (International Union of Crystallography Monographs on Crystallography)*. International Union of Crystallography Monographs

on Crystallography volume 9. Oxford University Press, USA, 2001. ISBN 0198509707,9780198509707. URL http://gen.lib.rus.ec/book/index.php?md5=744c25f2056a65018245232ef7671f33.

[115] Subrahmanyam Sappati, Ali Hassanali, Ralph Gebauer, and Prasenjit Ghosh. Nuclear quantum effects in a hiv/cancer inhibitor: The case of ellipticine. *The Journal of Chemical Physics*, 145(20):205102, 2016. doi: 10.1063/1.4968046. URL http://dx.doi.org/10.1063/1.4968046.

[116] Krishnan Rajeshwar, Robert McConnell, and Stuart Licht. Solar hydrogen generation. *Toward a Renewable Energy Future*, 2008.

[117] Akira Fujishima, Xintong Zhang, and Donald. A. Tryk. Heterogeneous photocatalysis: From water photolysis to applications in environmental cleanup. *International Journal of Hydrogen Energy*, 32(14):2664–2672, 2007. ISSN 0360-3199. doi: https://doi.org/10.1016/j.ijhydene.2006.09.009. URL http://www.sciencedirect.com/science/article/pii/S0360319906004356. International Conference on Materials for Hydrogen Energy: Solar Hydrogen (ICMHE 2004).

[118] Kazuhiko Maeda, Kentaro Teramura, Daling Lu, Tsuyoshi Takata, Nobuo Saito, Yasunobu Inoue, and Kazunari Domen. Photocatalyst releasing hydrogen from water. *Nature*, 440(7082):295, 2006.

[119] Andrew Mills and Stephen Le Hunte. An overview of semiconductor photocatalysis. *Journal of Photochemistry and Photobiology A: Chemistry*, 108(1):1–35, 1997. ISSN 1010-6030. doi: https://doi.org/10.1016/S1010-6030(97)00118-4. URL http://www.sciencedirect.com/science/article/pii/S1010603097001184.

[120] Akihiko Kudo. Development of photocatalyst materials for water splitting. *International Journal of Hydrogen Energy*, 31(2):197 – 202, 2006. ISSN 0360-3199. doi: https://doi.org/10.1016/j.ijhydene.2005.04.050. URL http://www.sciencedirect.com/science/article/pii/S0360319905001576. HTM 2004.

[121] Bill Durham and Thomas J Meyer. Photoelectrochemical cells based on electron-transfer quenching of excited states. *Journal of the American Chemical Society*, 100(19):6286–6287, 1978.

[122] Keith M Haynes, Kaci C Kratch, Sean D Stovall, Christopher O Obondi, Casey R Thurber, and W Justin Youngblood. Tuning interfacial electron transfer in nanostructured cuprous oxide photoelectrochemical cells with charge-selective molecular coatings. *ACS applied materials & interfaces*, 7(30):16133–16137, 2015.

[123] Felipe Guzman, Steven SC Chuang, and Cheng Yang. Role of methanol sacrificing reagent in the photocatalytic evolution of hydrogen. *Industrial & Engineering Chemistry Research*, 52(1):61–65, 2012.

[124] Donia Beydoun, Rose Amal, Gary Low, and S McEvoy. Role of nanoparticles in photocatalysis. *Journal of Nanoparticle Research*, 1(4):439–458, 1999.

[125] Ü. Özgür, Ya. I. Alivov, C. Liu, A. Teke, M. A. Reshchikov, S. Doğan, V. Avrutin, S.-J. Cho, and H. Morkoç. A comprehensive review of zno materials and devices. *Journal of Applied Physics*, 98(4):041301, 2005. doi: 10.1063/1.1992666. URL https://doi.org/10.1063/1.1992666.

[126] Aleksandra B Djurišić and Yu Hang Leung. Optical properties of zno nanostructures. *small*, 2(8-9):944–961, 2006.

[127] Kazuhiro Takanabe, Tsutomu Uzawa, Xinchen Wang, Kazuhiko Maeda, Masao Katayama, Jun Kubota, Akihiko Kudo, and Kazunari Domen. Enhancement of photocatalytic activity of zinc-germanium oxynitride solid solution for overall water splitting under visible irradiation. *Dalton Transactions*, (45):10055–10062, 2009.

[128] Kulamani Parida and Lagnamayee Mohapatra. Recent progress in the development of carbonate-intercalated zn/cr ldh as a novel photocatalyst for hydrogen evolution aimed at the utilization of solar l ight. *Dalton Transactions*, 41(4):1173–1178, 2012.

[129] Enrico Borgarello, John Kiwi, Ezio Pelizzetti, Mario Visca, and Michael Grätzel. Photochemical cleavage of water by photocatalysis. *Nature*, 289:158 EP –, Jan 1981. URL http://dx.doi.org/10.1038/289158a0.

[130] Nick S Norberg and Daniel R Gamelin. Influence of surface modification on the luminescence of colloidal zno nanocrystals. *The Journal of Physical Chemistry B*, 109(44):20810–20816, 2005.

[131] Lin Guo, Shihe Yang, Chunlei Yang, Ping Yu, Jiannong Wang, Weikun Ge, and George KL Wong. Synthesis and characterization of poly (vinylpyrrolidone)-modified zinc oxide nanoparticles. *Chemistry of Materials*, 12(8):2268–2274, 2000.

[132] Zheng Hua, Qinfeng Xu, Xiangnan Huang, Chunfeng Zhang, Xiaoyong Wang, and Min Xiao. Energy transfer from a single semiconductor nanocrystal to dye molecules. *ACS nano*, 8(7):7060–7066, 2014.

[133] Prashant V Kamat and Brian Patrick. Photophysics and photochemistry of quantized zinc oxide colloids. *The journal of physical chemistry*, 96(16):6829–6834, 1992.

[134] Leena George, Athira K Kunhikannan, Rajith Illathvalappil, Divya Ottoor, Sreekumar Kurungot, and R Nandini Devi. Understanding the electron transfer process in zno–naphthol azobenzoic acid composites from photophysical characterisation. *Physical Chemistry Chemical Physics*, 18(32):22179–22187, 2016.

[135] Ryu Abe, Kenichi Shinmei, Kohjiro Hara, and Bunsho Ohtani. Robust dye-sensitized overall water splitting system with two-step photoexcitation of coumarin dyes and metal oxide semiconductors. *Chem. Commun.*, pages 3577–3579, 2009. doi: 10.1039/B905935K. URL http://dx.doi.org/10.1039/B905935K.

[136] Anderson Janotti and Chris G Van de Walle. Fundamentals of zinc oxide as a semiconductor. *Reports on Progress in Physics*, 72(12):126501, 2009. URL http://stacks.iop.org/0034-4885/72/i=12/a=126501.

[137] Akihiko Kudo and Yugo Miseki. Heterogeneous photocatalyst materials for water splitting. *Chem. Soc. Rev.*, 38:253–278, 2009. doi: 10.1039/B800489G. URL http://dx.doi.org/10.1039/B800489G.

[138] Jae Sung Lee. Photocatalytic water splitting under visible light with particulate semiconductor catalysts. *Catalysis Surveys from Asia*, 9(4):217–227, 2005.

[139] Jing Liqiang, Qu Yichun, Wang Baiqi, Li Shudan, Jiang Baojiang, Yang Libin, Fu Wei, Fu Honggang, and Sun Jiazhong. Review of photoluminescence performance of nano-sized semiconductor materials and its relationships with photocatalytic activity. *Solar Energy Materials and Solar Cells*, 90(12):1773–1787, 2006.

[140] Masaya Matsuoka, Masaaki Kitano, Masato Takeuchi, Koichiro Tsujimaru, Masakazu Anpo, and John M Thomas. Photocatalysis for new energy production: recent advances in photocatalytic water splitting reactions for hydrogen production. *Catalysis Today*, 122(1-2):51–61, 2007.

[141] Nail M Shavaleev, Harry Adams, Jonathan Best, Ruth Edge, Suppiah Navaratnam, and Julia A Weinstein. Deep-red luminescence and efficient singlet oxygen generation by cyclometalated platinum (ii) complexes with 8-hydroxyquinolines and quinoline-8-thiol. *Inorganic chemistry*, 45(23):9410–9415, 2006.

[142] Amritanjali Tiwari, Indranil Mondal, and Ujjwal Pal. Visible light induced hydrogen production over thiophenothiazine-based dye sensitized tio2 photocatalyst in neutral water. *RSC Adv.*, 5:31415–31421, 2015. doi: 10.1039/C5RA03039K. URL http://dx.doi.org/10.1039/C5RA03039K.

[143] Paolo Giannozzi, Stefano Baroni, Nicola Bonini, Matteo Calandra, Roberto Car, Carlo Cavazzoni, Davide Ceresoli, Guido L Chiarotti, Matteo Cococcioni, Ismaila Dabo, Andrea Dal Corso, Stefano de Gironcoli, Stefano Fabris, Guido Fratesi, Ralph Gebauer, Uwe Gerstmann, Christos Gougoussis, Anton Kokalj, Michele Lazzeri, Layla Martin-Samos, Nicola Marzari, Francesco Mauri, Riccardo Mazzarello, Stefano Paolini, Alfredo Pasquarello, Lorenzo Paulatto, Carlo Sbraccia, Sandro Scandolo, Gabriele Sclauzero, Ari P Seitsonen, Alexander Smogunov, Paolo Umari, and Renata M Wentzcovitch. Quantum espresso: a modular and open-source software project for quantum simulations of materials. *Journal of Physics: Condensed Matter*, 21(39):395502, 2009. URL http://stacks.iop.org/0953-8984/21/i=39/a=395502.

[144] Dirk Vogel, Peter Krüger, and Johannes Pollmann. Self-interaction and relaxation-corrected pseudopotentials for ii-vi semiconductors. *Phys. Rev. B*, 54:5495–5511, Aug 1996. doi: 10.1103/PhysRevB.54.5495. URL https://link.aps.org/doi/10.1103/PhysRevB.54.5495.

[145] Arrigo Calzolari, Alice Ruini, and Alessandra Catellani. Anchor group versus conjugation: Toward the gap-state engineering of functionalized zno(1010) surface for optoelectronic applications. *Journal of the American Chemical Society*, 133 (15):5893–5899, 2011. doi: 10.1021/ja1101008. URL http://dx.doi.org/10.1021/ja1101008. PMID: 21443210.

[146] Anderson Janotti, David Segev, and Chris G. Van de Walle. Effects of cation d states on the structural and electronic properties of iii-nitride and ii-oxide wide-band-gap semiconductors. *Phys. Rev. B*, 74:045202, Jul 2006. doi: 10.1103/PhysRevB.74.045202. URL https://link.aps.org/doi/10.1103/PhysRevB.74.045202.

[147] Eun-Ae Choi, Woo-Jin Lee, and K. J. Chang. Enhanced electron-mediated ferromagnetism in co-doped zno nanowires. *Journal of Applied Physics*, 108(2):023904, 2010. doi: 10.1063/1.3463412. URL http://dx.doi.org/10.1063/1.3463412.

[148] Litty Irimpan, V. P. N. Nampoori, P. Radhakrishnan, A. Deepthy, and Bindu Krishnan. Size dependent fluorescence spectroscopy of nanocolloids of zno. *Journal of Applied Physics*, 102(6):063524, 2007. doi: 10.1063/1.2778637. URL http://dx.doi.org/10.1063/1.2778637.

[149] Leena George, Subrahmanyam Sappati, Prasenjit Ghosh, and R. Nandini Devi. Surface site modulations by conjugated organic molecules to enhance visible light activity of zno nanostructures in photocatalytic water splitting. *The Journal of Physical Chemistry C*, 119(6):3060–3067, 2015. doi: 10.1021/jp511996z. URL https://doi.org/10.1021/jp511996z.

[150] Jittikarn Songkhao, Rajdeep Banerjee, Saikat Debnath, Shobhana Narasimhan, Napaporn Wannaprom, Parichatr Vanalabhpatana, Nicola Seriani, Ralph Gebauer, and Patchanita Thamyongkit. Structure-property relationship of pi-extended boron-dipyrromethene derivatives towards optoelectronic applications. *Dyes and Pigments*, 142:558 – 571, 2017. ISSN 0143-7208. doi: https://doi.org/10.1016/j.dyepig.2017.03.050. URL http://www.sciencedirect.com/science/article/pii/S0143720817301559.

[151] Leena George, Subrahmanyam Sappati, Prasenjit Ghosh, and R. Nandini Devi. Sensitizing with short conjugated molecules: Multimodal anchoring on zno nanoparticles for enhanced electron transfer characteristics, stability and h2 evolution. *Catalysis Today*, 309:89 – 97, 2018. ISSN 0920-5861. doi: https://doi.org/10.1016/j.cattod.2017.09.052. URL http://www.sciencedirect.com/science/article/pii/S0920586117306673. Catalysis for Sustainable Development, Peace and Prosperity.

Publication works are included in this thesis

Published

- Subrahmanyam Sappati, Hassanali, Ali, Gebauer, Ralph and Prasenjit Ghosh, "Nuclear Quantum Effects in an HIV/Cancer Inhibitor: The Case of Ellipticine.", 145, *J. Chem. Phys.*, **2016** 205102-205113 (Chapter 3).

  This publication was selected as a 2016 Editor′s Choice article. This collection contains 70 articles selected by the editors as the most innovative and influential articles of 2016. This work was highlighted in the ICTP news website.

- Leena George, Subrahmanyam Sappati, Prasenjit Ghosh, Nandini Devi, "Sensitizing with short conjugated molecules: Multimodal anchoring on ZnO nanoparticles for enhanced electron transfer characteristics, stability and H_2 evolution.", *Catalysis Today*, **2017**, 89-97, (Chapter 5).

- Leena George, Subrahmanyam Sappati, Prasenjit Ghosh, Nandini Devi, "Surface site modulations by conjugated organic molecules to enhance visible light activity of ZnO nanostructures in photocatalytic water splitting", *J. Phys. Chem. C*, **2015**, 3060-3067, (Chapter 5).

Communicated

- Leena George, Subrahmanyam Sappati, Prasenjit Ghosh, Nandini Devi, "Bimodal anchoring of short conjugated molecules on ZnO for photocatalytic hydrogen evolution through efficient electron injection: A combined computational and spectroscopy study.", *under revision, PCCP.* (Chapter 5)

Manuscript under preparation

- Subrahmanyam Sappati, Hassanali, Ali, Gebauer, Ralph and Prasenjit Ghosh, "**Role of Nuclear Quantum Effects on solute-solvent and solvent-solvent Hydrogen bonding: The case of Ellipticine in protic solvents** ", (*manuscript under preparation*), (Chapter 4).

- Subrahmanyam Sappati, Leena George, Nandini Devi, and Prasenjit Ghosh "Anchor Group versus Conjugation: Design of oligothiophenes based dyes for enhanced visible light absorption and photocatalytic water splitting in ZnO", (*manuscript under preparation*), (Chapter 5).

Other Publications

Published

- B. Dhara, Subrahmanyam Sappati, S. Singh, S. Kurungot, P. Ghosh , and N. Ballav, "Coordination polymers of Fe(III) and Al(III) ions with TCA ligand: distinctive fluorescence, CO_2 uptake, redox-activity and oxygen evolution reaction" , *Dalton Trans.*, **2016**, 6901-6908.

- Raj Kumar Koninti, Subrahmanyam Sappati, Sagar Satpathi, Krishna Gavvala, and Partha Hazra "Spectroscopy and Dynamics of Cryptolepine in the Nanocavity of Cucurbit[7]uril and DNA", *Chem. Phys. Chem*, **2015**, 506-515, DOI - 10.1002/cphc.201501011.

- A Sudheer Kumar, Vikas D Ghule, Sappati Subrahmanyam, Akhila K Sahoo, "Synthesis of Thermally Stable Energetic 1,2,3-Triazole Derivatives", *Chem. Eur. J*, **2013**, 509-518.